



Abschlussarbeit im Masterstudiengang Physik der
Kondensierten Materie

Entwicklung eines diagonalen isometrischen Tensor Netzwerk Algorithmus

Development of a Diagonal Isometric Tensor Network Algorithm

Benjamin Sappler

30. Juli 2024

Erstgutachter (Themensteller): Prof. Dr. Frank Pollmann
Zweitgutachter: Prof. Dr. Michael Knap

I hereby declare that this thesis is entirely the result of my own work except where otherwise indicated. I have only used the resources given in the list of references.

München, 30. Juli 2024

Benjamin Sappler

Abstract

The numerical simulation of strongly interacting quantum many-body systems is a very challenging problem because of the exponential growth of the Hilbert space with system size. In the last decades, Tensor Networks have emerged as the standard method for tackling this problem in one dimensional systems in the form of Matrix Product States (MPS). Tensor Networks have also been generalized for the highly relevant problem of two and more spatial dimensions. However, these so-called Projected Entangled Pair States (PEPS) are typically plagued by high computational complexity and drastic approximations. Recently, a new class of Tensor Networks, called isometric Tensor Product States (isoTPS), has been introduced for the simulation of two-dimensional quantum systems. This new class of Tensor Networks generalizes the canonical form of Matrix Product States to higher dimensions. In this work, we develop an alternative way of defining this canonical form by rotating the lattice by 45° and introducing auxiliary tensors. This alternative ansatz is then tested by performing ground state search and real-time evolution of the Transverse Field Ising (TFI) model on large square lattices of up to 800 spins.

Contents

1	Introduction	1
2	Tensors and Tensor Networks	5
2.1	Conventions and Notation	5
2.2	Tensor Decompositions	8
2.3	Isometric Tensor Networks	10
2.4	Matrix Product States (MPS)	12
2.5	Isometric Tensor Product States (isoTPS) in 2D	19
3	IsoTPS with Alternative Canonical Form	25
3.1	Network Structure	25
3.2	Yang-Baxter Move	28
3.3	Time Evolving Block Decimation (TEBD)	44
4	The Toric Code: An Exactly Representable Model	51
4.1	The Toric Code Model	51
4.2	Representing the Toric Code Ground State with YB-isoTPS	53
5	The Transverse Field Ising Model: Ground State Search and Time Evolution	57
5.1	The Transverse Field Ising Model	57
5.2	Ground State Search	58
5.3	Time Evolution after a Global Quench	68
6	Conclusion and Outlook	71
A	Optimization Problems for Isometric Tensor Networks	73
B	Riemannian Optimization of Isometries	77
C	Computing the Gradient and Hessian of the Disentangling Cost Functions	83
	Bibliography	89

Chapter 1

Introduction

Quantum many-body systems exhibit a variety of novel and exotic emergent behaviours arising from the interaction of many local degrees of freedom. Well-known examples of such phenomena are the fractional quantum Hall effect [1–3] and other spin liquids with fractionalized excitations [4], topological phases of matter [5], and high-temperature superconductivity [6, 7]. The main challenge in the study of quantum many-body systems is posed by the fact that the dimension of the many-body Hilbert space grows exponentially with the system size. For example, exact diagonalization of spin-1/2 models is limited to systems of a few tens of spins. There has been a lot of effort to overcome this problem by introducing numerical algorithms that approximately simulate quantum many-body systems, with the two most prominent approaches being Quantum Monte Carlo (QMC) [8, 9] and tensor network algorithms. While QMC algorithms have had a lot of success, the infamous sign problem [9, 10] prevents the method from simulating many interesting models, for example frustrated spin systems. Tensor network methods have had great success in the simulation of one-dimensional systems. Especially the Density Matrix Renormalization Group (DMRG) algorithm [11], which was later understood as a variational method over the class of Matrix Product States (MPS) [12–14], has developed to be the de-facto standard for the computation of ground state properties of gapped Hamiltonians. Such ground states exhibit a characteristic area law entanglement structure [15] and the success of DMRG is due to the remarkable ability of MPS to capture this entanglement structure efficiently [16, 17]. Another important problem is the real and imaginary time evolution of quantum states, which can for example be performed by using the Time Evolving Block Decimation (TEBD) [18] algorithm or the Time Dependent Variational Principle (TDVP) [19]. The natural generalization of MPS to two and higher dimensions is given in the form of Projected Entangled Pair States (PEPS) [14, 20], which are able to efficiently represent area law states [14]. However, algorithms for ground state search and time evolution of PEPS have a computational cost scaling with high powers of the bond dimension D . For example, the cost of a full time evolution update scales as $\mathcal{O}(D^{10})$ and the cost of variational energy minimization scales as $\mathcal{O}(D^{12})$ [21, 22]. Additionally, the energy-minimization algorithm that is obtained by generalizing DMRG to PEPS

requires solving a generalized eigenvalue problem, which is numerically ill-conditioned [22].

Recently, the new class of isometric Tensor Product States (isoTPS) have been introduced [23–25], generalizing the canonical form of MPS to two and higher dimensions by enforcing isometry constraints. This allows for the efficient computation of local expectation values and can reduce the computational cost of algorithms compared to PEPS. For example, the cost of real and imaginary time evolution is reduced from $\mathcal{O}(D^{10})$ to $\mathcal{O}(D^7)$ [23]. While the generalization of DMRG to isoTPS still has a computational complexity of $\mathcal{O}(D^{12})$, the generalized eigenvalue problem is reduced to a standard eigenvalue problem because of the canonical form, improving the stability of the algorithm [26]. The downside to this approach is that not all quantum states that can be represented by PEPS can also be represented by isoTPS. It is thus an interesting question to ask which kinds of states and, more generally, which kinds of quantum phases can still be efficiently written as an isoTPS. The expressional power of the ansatz has been studied in [27], where it was found that isoTPS with finite bond dimension can exactly represent ground state wave functions of string-net liquid models. This shows that long-range entanglement does not form an obstruction for isoTPS representations and suggests that the ground states of gapped Hamiltonians with gappable edges can be efficiently represented as an isoTPS. There have also been works discussing the computational complexity of isoTPS contractions [28] and relating isoTPS to quantum circuits [29, 30]. In [31], topological phase transitions were studied with isoTPS, showing that they can represent certain critical states with power-law correlations. IsoTPS were also extended to fermionic systems [32], to two dimensional strips of infinite length [33], and to three dimensional cubic lattices [34]. They have also been used to compute properties of two dimensional thermal states [35].

While algorithms on isoTPS have shown first promising results, there are still open questions. For example, the best way of defining the canonical form is not yet agreed upon. Different canonical forms could in principle lead to reduced errors, more stable algorithms, and reduced computational cost. In this work we propose a new way of defining the canonical form of isoTPS. The ansatz differs from the original isoTPS by rotating the lattice by 45° and introducing auxiliary tensors that do not have a physical degree of freedom. While we mainly discuss the implementation on the square lattice, this ansatz is easily generalizable to other lattice types.

The thesis is structured as follows. First, an introduction to tensor networks, MPS and isoTPS is provided in Chapter 2. Next, the new ansatz of defining the canonical form is introduced on the square lattice in Chapter 3 and a TEBD algorithm for real and imaginary time evolution is formulated. In Chapter 4 it is shown that isoTPS with the alternative canonical form are able to represent the ground state of the Toric Code model, a quantum spin model with \mathbb{Z}_2 topological order. The method is then further benchmarked on the Transverse Field Ising (TFI) model

in Chapter 5, showcasing its ability to find ground states and perform real time evolution. Additionally, the ansatz is generalized to the honeycomb lattice. Last, a conclusion and outlook are given in Chapter 6. Our implementation is openly available at [36].

Chapter 2

Tensors and Tensor Networks

In the following, a brief introduction to tensors, tensor networks, and tensor network algorithms is given. We start by defining the conventions and notation used in this thesis in Section 2.1. In Section 2.2 we introduce important tensor decompositions that are used extensively in tensor network algorithms. In Section 2.3 we define isometric tensor networks and discuss their properties. Lastly, we give examples for physical states being represented in terms of isometric tensor networks, namely the popular Matrix Product States (MPS) in Section 2.4 and the recently developed isometric Tensor Product States in 2D (isoTPS) in Section 2.5.

2.1 Conventions and Notation

For the purpose of this thesis we define a *tensor* T of rank n as an n -dimensional array of complex numbers

$$T \in \mathbb{C}^{\chi_1 \times \chi_2 \times \dots \times \chi_n}, \quad \chi_i \in \{1, 2, \dots\} \quad (2.1)$$

with entries

$$T_{i_1, i_2, \dots, i_n} \in \mathbb{C}, \quad i_j \in \{1, 2, \dots, \chi_j\}.$$

For example, a rank-0 tensor is a scalar, a rank-1 tensor is a vector, and a tensor of rank-2 is a matrix. It is convenient to use a diagrammatic notation, drawing tensors as shapes and tensor indices as lines (*legs*) emerging from these shapes. As an example we draw a few simple tensors in tensor diagram notation in Figure 2.1.

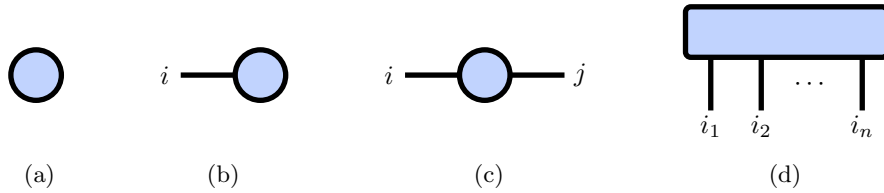


Figure 2.1: Tensors of different ranks are shown in diagrammatic notation. (a) A scalar, (b) a vector, (c) a matrix, (d) a general tensor of rank n as defined in Equation (2.1).

An *index contraction* between two or more tensors is the linear operation that is performed by summing over a given set of indices. For example, the scalar product of two vectors $A \in \mathbb{C}^\chi$ and $B \in \mathbb{C}^\chi$,

$$c = \sum_{\alpha=1}^{\chi} A_{\alpha} B_{\alpha}, \quad c \in \mathbb{C}, \quad (2.2)$$

and the matrix product of two matrices $A \in \mathbb{C}^{\chi_1 \times \chi_2}$, $B \in \mathbb{C}^{\chi_2 \times \chi_3}$,

$$C_{ij} = \sum_{\alpha=1}^{\chi_2} A_{i\alpha} B_{\alpha j}, \quad C \in \mathbb{C}^{\chi_1 \times \chi_3} \quad (2.3)$$

constitute index contractions. A more involved example is the index contraction of two rank-3 tensors $A \in \mathbb{C}^{\chi_1 \times \chi_2 \times \chi_3}$, $B \in \mathbb{C}^{\chi_2 \times \chi_4 \times \chi_5}$ and one rank-4 tensor $C \in \mathbb{C}^{\chi_3 \times \chi_5 \times \chi_6 \times \chi_7}$, where we contract along the indices with dimension χ_2 , χ_3 and χ_5 . The result is a rank-4 tensor $D \in \mathbb{C}^{\chi_1 \times \chi_4 \times \chi_6 \times \chi_7}$:

$$D_{ijkl} = \sum_{\alpha=1}^{\chi_2} \sum_{\beta=1}^{\chi_3} \sum_{\gamma=1}^{\chi_5} A_{i\alpha\beta} B_{\alpha j\gamma} C_{\beta\gamma kl}. \quad (2.4)$$

In tensor diagrams, index contractions are drawn by connecting the legs corresponding to contracted indices. Lines connecting two tensors are sometimes called *bonds*, while indices not used in contractions are called *open indices*. The *bond dimension* χ_i denotes the number of different values an index i can take. It is often more convenient to discuss tensor network algorithms in terms of diagrams than in terms of equations.

A *tensor network* is defined as a set of tensors that is contracted in a specified way. We draw the tensor diagrams of the above equations in Figure 2.2.

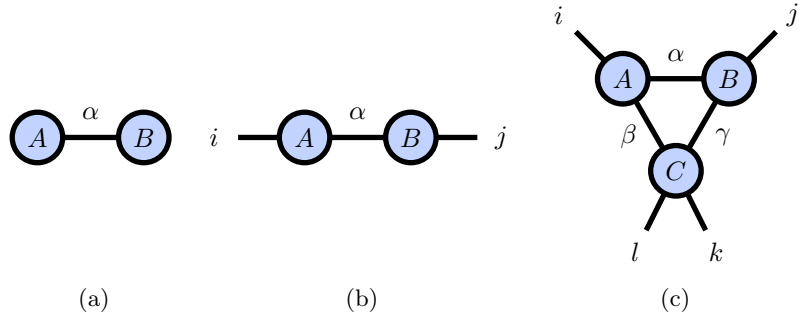


Figure 2.2: Tensor networks in diagrammatic notation. (a) Scalar product (2.2). (b) Matrix product (2.3). (c) More involved network consisting of three tensors (2.4).

Because tensor contractions are linear, the order in which tensors are contracted does not change the result. However, the computational complexity does in general

depend on the order of contractions and can thus be minimized by choosing the optimal contraction order. The computational complexity of a tensor contraction of two tensors is simply the product of all bond dimensions, where bond dimensions of contracted indices only appear in the product once. For example, the computational complexity of contracting tensors B and C from the contraction (2.4) scales as $\mathcal{O}(\chi_1\chi_2\chi_4\chi_5\chi_6\chi_7)$.

Given two normed vector spaces V_1 and V_2 with $\dim(V_1) = m$, $\dim(V_2) = n$, $m \leq n$, an *isometry* (sometimes also called *semi-unitary*) is a linear, norm-preserving map $W : V_1 \rightarrow V_2$ from the smaller to the larger vector space. Each isometry can be represented by a $n \times m$ matrix W fulfilling the *isometry condition*

$$W^\dagger W = \mathbb{1}, \quad WW^\dagger = \mathbb{P}, \quad (2.5)$$

where $\mathbb{P} = \mathbb{P}^2$ is a projection. If $m = n$, it holds $\mathbb{P} = \mathbb{1}$ and W is a *unitary map*. An isometry tensor is a tensor that through grouping of indices and reshaping (i.e. matrixization) becomes an isometry. In tensor network diagrams, we draw isometries by decorating lines with arrows. Following the convention of [23, 26], we denote the indices belonging to the larger vector space by incoming arrows and the indices belonging to the smaller vector space by outgoing arrows. Unitary tensors are decorated with bidirectional arrows on all indices, where the grouping must be inferred from the context. Ordinary tensors are drawn without arrows. Tensor diagrams for isometric and unitary tensors are shown in Figure 2.3.

We lastly introduce an inner product for rank- n tensors $A, B \in \mathbb{C}^{\chi_1 \times \dots \times \chi_n}$, the *Frobenius inner product*

$$\langle A, B \rangle_{\text{F}} := \sum_{\mu_1=1}^{\chi_1} \dots \sum_{\mu_n=1}^{\chi_n} A_{\mu_1, \dots, \mu_n}^* B_{\mu_1, \dots, \mu_n} = \text{Tr} \left(A^\dagger B \right),$$

where A^* denotes the complex conjugate of A and the last equality holds only if $n = 2$. The Frobenius inner product induces a norm, the *Frobenius norm*

$$\|A\|_{\text{F}} = \sqrt{\langle A, A \rangle_{\text{F}}},$$

which can be used to define a measure of distance $\|A - B\|_{\text{F}}$ between two tensors A and B .

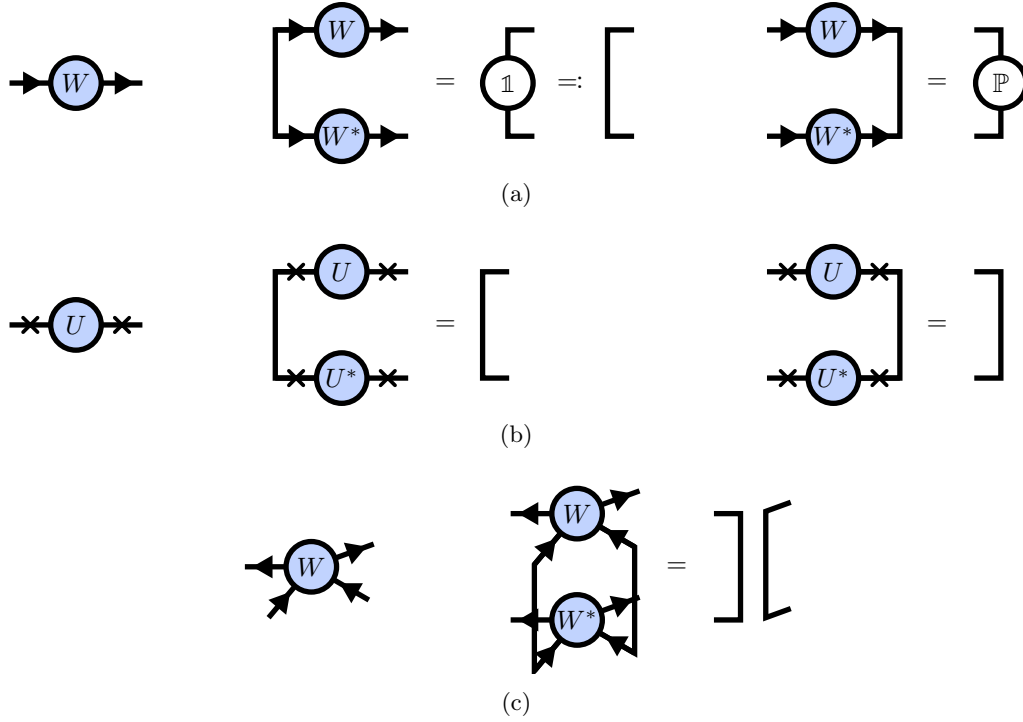


Figure 2.3: (a) An isometric matrix W is depicted as a tensor diagram. The isometry condition (2.5) reduces contractions of W with its adjoint to the identity matrix or to a projector \mathbb{P} . (b) A unitary matrix U is drawn by using double arrows. For unitary matrices, the projector \mathbb{P} is equal to the identity. (c) Isometric tensors of higher rank must fulfill the isometry condition by grouping of indices.

2.2 Tensor Decompositions

There are two decompositions that are used extensively in this thesis: The QR-decomposition and the Singular Value Decomposition. Both decompositions are matrix decompositions but can be applied to tensors as well by first grouping indices and reshaping to a matrix, applying the decomposition, and reshaping the result back to the original indices.

The *reduced QR-decomposition* of a matrix $A \in \mathbb{C}^{n \times m}$ is the decomposition

$$A = QR, \quad (2.6)$$

where $Q \in \mathbb{C}^{n \times k}$ is an isometry, $R \in \mathbb{C}^{k \times m}$ is an upper triangular matrix and $k := \min(n, m)$. The computational complexity of the QR decomposition scales as

$$\mathcal{O}(nmk). \quad (2.7)$$



Figure 2.4: Tensor decompositions are shown in tensor network diagram notation. (a) QR-decomposition (2.6). (b) Singular Value Decomposition (2.8)

The QR decomposition is drawn as a tensor diagram in Figure 2.4a.

The *Singular Value Decomposition* (SVD) of a matrix $A \in \mathbb{C}^{n \times m}$ is the decomposition

$$A = USV^\dagger, \quad (2.8)$$

where $U \in \mathbb{C}^{n \times k}$ and $V \in \mathbb{C}^{m \times k}$ are isometries, $S \in \mathbb{R}^{k \times k}$ is a diagonal real matrix of non-negative *singular values*, and $k := \min(n, m)$. The computational complexity of the SVD is the same as for the QR decomposition (2.7). However, while the scaling is the same, the prefactors are lower for the QR decomposition in most implementations, meaning that the QR decomposition is faster in practice. Moreover, in contrast to the SVD, the QR decomposition allows for highly efficient implementations on Graphics Processing Units (GPUs), which enables decompositions of large matrices to be carried out significantly faster and more power efficiently. Thus, whenever the singular values are not needed, the QR decomposition is preferred over the SVD. Figure 2.4b shows a tensor network diagram of the SVD (2.8).

An important property of the SVD is that it can be used to approximate a matrix A by a matrix \tilde{A} of lower rank $\chi < \min(m, n)$. This *truncated SVD* can be performed by keeping only the largest $\chi < k$ singular values and omitting the corresponding columns of U and V :

$$A \approx \tilde{A} = \tilde{U} \tilde{S} \tilde{V}, \quad (2.9)$$

with isometries $\tilde{U} \in \mathbb{C}^{n \times \chi}$, $\tilde{V} \in \mathbb{C}^{m \times \chi}$ and real diagonal matrix $\tilde{S} \in \mathbb{R}^{\chi \times \chi}$ with non-negative entries. It can be shown [37] that the truncated SVD minimizes the distance $\|A - \tilde{A}\|_F$ between A and \tilde{A} under the constraint $\text{rank}(\tilde{A}) = \chi$. The remaining *truncation error* is

$$\varepsilon_{\text{trunc}} = \|A - \tilde{A}\|_F = \sqrt{\sum_{i=\chi+1}^{\min(m,n)} S_i^2},$$

where we have sorted the singular values in descending order. The truncated SVD is frequently used in tensor network algorithms to truncate tensors to a maximum bond dimension χ_{max} .

2.3 Isometric Tensor Networks

An isometric tensor network is a tensor network whose diagrams bonds can be consistently assigned with arrows. In particular we will look at finite tensor networks where the arrows do not form any loops. In such networks, all arrows point to a single tensor, the *orthogonality center*. These networks have the very useful property that the error of local approximations around the orthogonality center can be computed locally, without contracting the full network. Let \mathcal{N} be the tensor that is the result of contracting the full network, and let \mathcal{M} be the tensor resulting from the contraction of a subregion of the network around the orthogonality center, where all arrows in the tensor network diagram point towards \mathcal{M} (see Figure 2.5a for an example in tensor diagram notation). Let us now approximate the sub-network \mathcal{M} by a different sub-network \mathcal{M}' , which changes the contraction of the full network to \mathcal{N}' (see 2.5b). We can compute the error ε of this approximation as

$$\begin{aligned}
 \varepsilon^2 &= \|\mathcal{N} - \mathcal{N}'\|_{\text{F}}^2 \\
 &= \langle \mathcal{N} - \mathcal{N}', \mathcal{N} - \mathcal{N}' \rangle_{\text{F}} \\
 &= \|\mathcal{N}\|_{\text{F}}^2 + \|\mathcal{N}'\|_{\text{F}}^2 - 2 \operatorname{Re} \langle \mathcal{N}, \mathcal{N}' \rangle_{\text{F}} \\
 &= \|\mathcal{M}\|_{\text{F}}^2 + \|\mathcal{M}'\|_{\text{F}}^2 - 2 \operatorname{Re} \langle \mathcal{M}, \mathcal{M}' \rangle_{\text{F}} \\
 &= \|\mathcal{M} - \mathcal{M}'\|_{\text{F}}^2,
 \end{aligned}$$

where in the fourth step we used the fact that all tensors outside of the sub-network satisfy the isometry condition. As an example, the contraction of $\langle \mathcal{N}, \mathcal{N}' \rangle_{\text{F}} = \langle \mathcal{M}, \mathcal{M}' \rangle_{\text{F}}$ is shown in Figure 2.5c. As one can see, the computation of the error reduces to a contraction of only the local sub-networks. This greatly simplifies the computation of optimal approximations of tensors especially for large networks because the full network does not need to be contracted. When the tensor network represents a quantum state, this also makes it very easy to compute local expectation values, as will become clear in the next section. This is because the computation of the overlap of the wave function can be simplified to a contraction of a local environment around the orthogonality center. Additionally, approximations made by the truncated SVD (2.9) are, when performed at the orthogonality center, globally optimal for isometric tensor networks, instead of only locally optimal for non-isometric tensor networks.

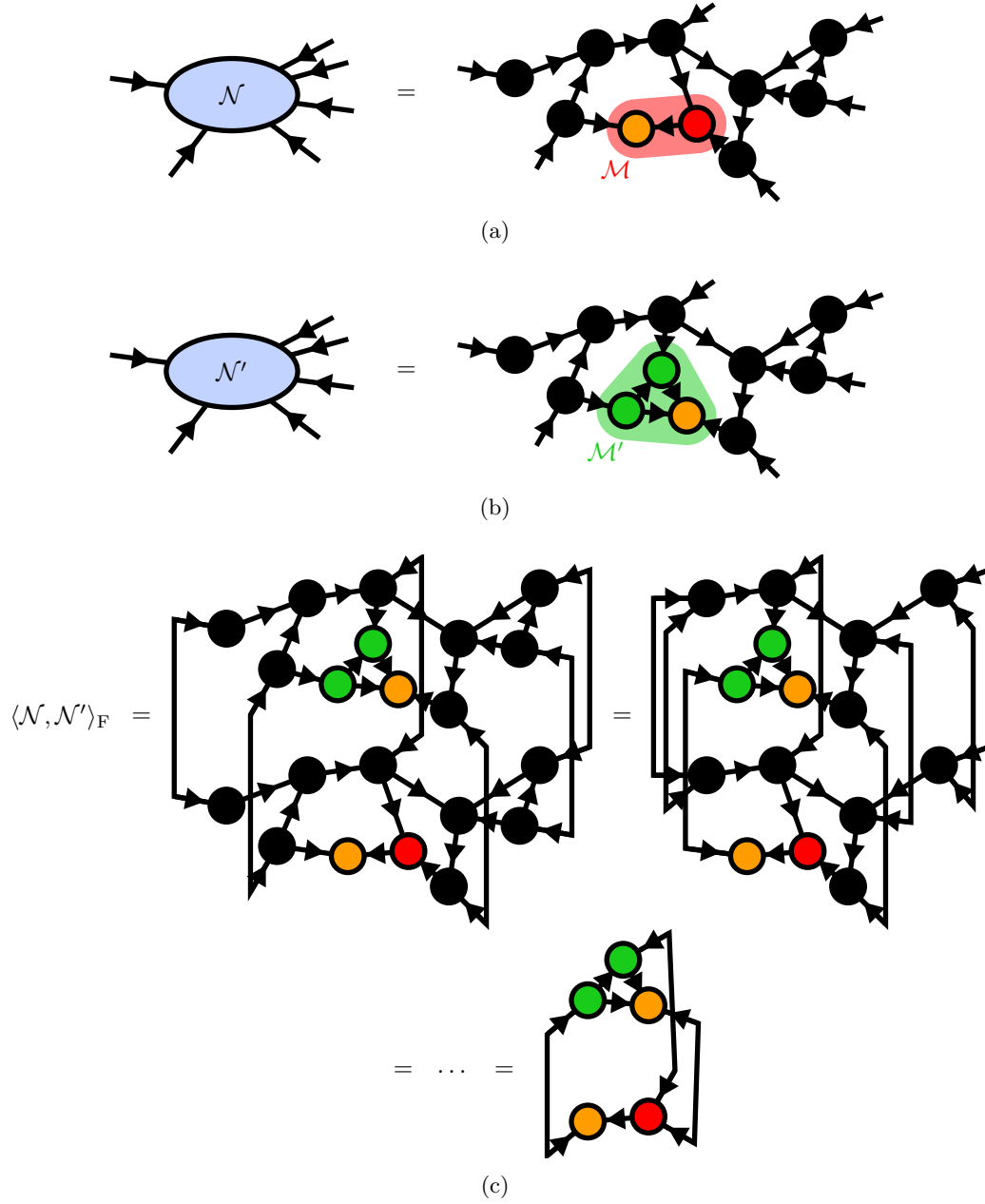


Figure 2.5: (a) An isometric tensor network \mathcal{N} with the orthogonality center depicted in orange. The sub-network \mathcal{M} is made up of all tensors in the red region. (b) The isometric tensor network \mathcal{N}' with an updated sub-network \mathcal{M}' . (c) The computation of the inner product $\langle \mathcal{N}, \mathcal{N}' \rangle_F$ reduces to a contraction of the sub-networks $\langle \mathcal{M}, \mathcal{M}' \rangle_F$ because of the isometry condition. In the shown tensor network, the tensors of \mathcal{N} are complex conjugated.

2.4 Matrix Product States (MPS)

The Density Matrix Renormalization Group (DMRG) algorithm, a variational method over the class of Matrix Product States (MPS), has developed to be the de-facto standard for the numerical simulation of one-dimensional quantum systems. The success of this method is due to the remarkable ability of MPS to capture the area law entanglement characteristics of ground states of gapped Hamiltonians. Additionally, due to the elegant diagrammatic notation of tensor networks, new algorithms can be developed and discussed efficiently and intuitively. Applications of MPS include finding ground and thermal states, real and imaginary time evolution, and the computation of dynamical properties of lattice Hamiltonians. In the following, we give a brief introduction to MPS, for a more in-depth discussion see [13, 14, 38].

The state of a quantum many-body system can be written as

$$|\Psi\rangle = \sum_{i_1=1}^{d_1} \sum_{i_2=1}^{d_2} \cdots \sum_{i_N=1}^{d_N} \Psi_{i_1, i_2, \dots, i_N} |i_1\rangle \otimes |i_2\rangle \otimes \cdots \otimes |i_N\rangle,$$

where N is the number of subsystems (e.g. lattice sites or particles), and $\{|i_1\rangle \otimes |i_2\rangle \otimes \cdots \otimes |i_N\rangle\}$, $i_j = 0, \dots, d_j$ is a set of basis vectors of the full many-body Hilbert space

$$\mathcal{H} = \bigotimes_{j=1}^N \mathcal{H}_j,$$

with $\dim(\mathcal{H}_j) = d_j$ the dimension of the local Hilbert space of subsystem j . To simplify the notation, we will assume that the dimension of all local subsystems is the same, $d_j = d$. The d^N complex numbers $\Psi_{i_1, i_2, \dots, i_N}$ fully describe the quantum many-body state, and one can think of $\Psi \in \mathbb{C}^{d \times \cdots \times d}$ as a tensor of rank N . However, due to the number of parameters scaling exponentially with system size, only very small system sizes are accessible computationally. One can proceed by writing Ψ as a tensor network of tensors of lower rank. A *Matrix Product State* (MPS) is constructed by introducing N rank-3 tensors $T^{[n]} \in \mathbb{C}^{d \times \chi_{n-1} \times \chi_n}$ and contracting them in a chain as

$$\Psi_{i_1, i_2, \dots, i_N} := \sum_{\alpha_1=1}^{\chi_1} \sum_{\alpha_2=1}^{\chi_2} \cdots \sum_{\alpha_{N-1}=1}^{\chi_{N-1}} T_{1, \alpha_1}^{[1], i_1} T_{\alpha_1, \alpha_2}^{[2], i_2} \cdots T_{\alpha_{N-1}, 1}^{[N], i_N}, \quad (2.10)$$

where we have written the indices i_n as superscripts, such that the sums are performed only over subscripts. Note that in this notation the bond dimensions at the two ends of the chain are $\chi_0 = \chi_N = 1$, and we can interpret the tensors $T^{[1]}$ and $T^{[N]}$ as tensors of rank-2. Since the indices $i_n = 0, 1, \dots, d$ represent the local physical degrees of freedom, they are sometimes referred to as *physical indices*. The other indices are called *virtual indices*. A tensor diagram of the MPS (2.10) is given in Figure 2.6.

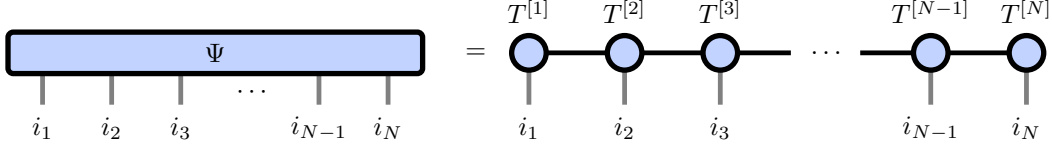


Figure 2.6: Diagrammatic representation of the Matrix Product State (2.10).

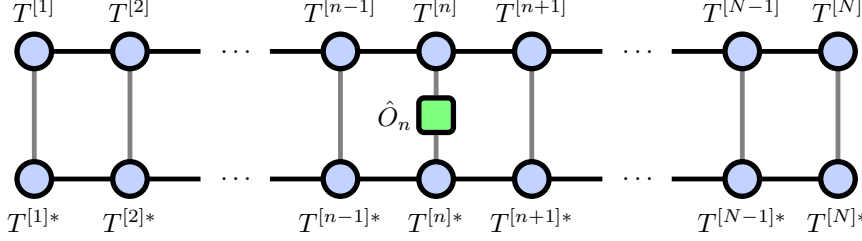


Figure 2.7: The computation of the expectation value of a local operator can be computed by contracting the MPS with its conjugate transpose, with the operator "sandwiched" in between.

An important property of MPS is the existence of a *canonical form* as an isometric tensor network, where a single tensor $T^{[n]} =: \Lambda^{[n]}$ is selected as the orthogonality center. One can bring an arbitrary MPS into this canonical form through successive QR-decompositions or SVDs, starting at the outer ends of the chain and isometrizing one tensor at a time, until the orthogonality center is reached [13]. In Figure 2.8a an MPS in canonical form with the orthogonality center at subsystem n is visualized in diagrammatic notation. We call tensors to the left of the orthogonality center $A^{[i]}$ and tensors to the right of the orthogonality center $B^{[i]}$. The canonical form greatly simplifies many operations on MPS and allows for the formulation of efficient algorithms, where many contractions reduce to identity due to the isometry condition (2.5), see Figure 2.8b and Figure 2.8c. For example, the expectation value $\langle \Psi | \hat{O} | \Psi \rangle$ of a one-site operator $\hat{O} \in \mathbb{C}^{d \times d}$ acting on site n can for a general MPS be computed as

$$\begin{aligned}
 \langle \Psi | \hat{O} | \Psi \rangle &= \sum_{i_1, \dots, i_N, j_n=1}^d \Psi_{i_1, i_2, \dots, i_N} \Psi_{i_1, \dots, i_{n-1}, j_n, i_{n+1}, \dots, i_N}^* \langle j_n | \hat{O} | i_n \rangle \\
 &= \sum_{i_1, \dots, i_N, j_n=1}^d \left(T^{[1], i_1} \dots T^{[N], i_N} \right) \\
 &\quad \cdot \left(T^{[1], i_1*} \dots T^{[n], j_n*} \dots T^{[N], i_N*} \right) \cdot \hat{O}_{i_n, j_n},
 \end{aligned} \tag{2.11}$$

where the $T^{[n], i_n}$ are interpreted as matrices for $1 < n < N$ and as row/column

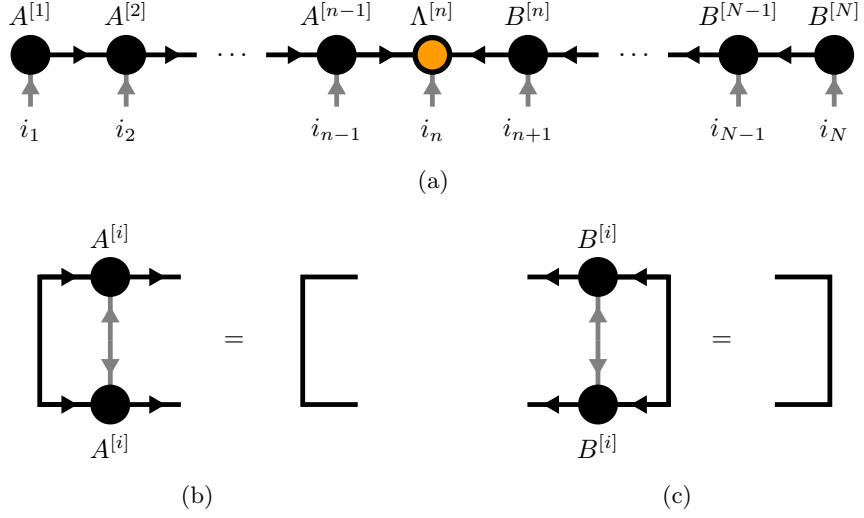


Figure 2.8: (a) Diagrammatic representation of an MPS in canonical form. (b) The left isometry condition. (c) The right isometry condition.

vectors for $n = 1, N$ such that the product

$$\left(T^{[1], i_1} \dots T^{[N], i_N} \right)$$

gives a scalar. The contraction (2.11) is visualized as a tensor diagram in Figure 2.7. Here the advantage of the diagrammatic notation becomes apparent: It is much easier to understand how tensors are contracted when expressing the contraction in terms of tensor network diagrams. The computational cost of computing the expectation value scales linear with the system size $\mathcal{O}(N\chi^3d)$, where χ is the maximum virtual bond dimension $\chi = \max\{\chi_1, \dots, \chi_N\}$. If the MPS is however given in canonical form with the orthogonality center at site n , the computation reduces to a contraction of only three tensors as can be seen in Figure 2.9, and the computational cost $\mathcal{O}(\chi^3d)$ becomes independent of system size.

Approximating Quantum States with MPS

Until now, the MPS representation of $|\Psi\rangle$ is still exact. One can approximate an MPS by restricting the virtual bond dimension to a maximal bond dimension $\chi_n \leq \chi_{\max}$. In this case, the number of parameters that need to be stored to describe the state is reduced from $\mathcal{O}(d^N)$ to $\mathcal{O}(N\chi_{\max}^2d)$. To arrive at this approximation, two neighboring tensors can be contracted and split via a truncated SVD, keeping only the χ_{\max} largest singular values. If the orthogonality center of the MPS is at one of the two tensors, this approximation is globally optimal as explained in Section

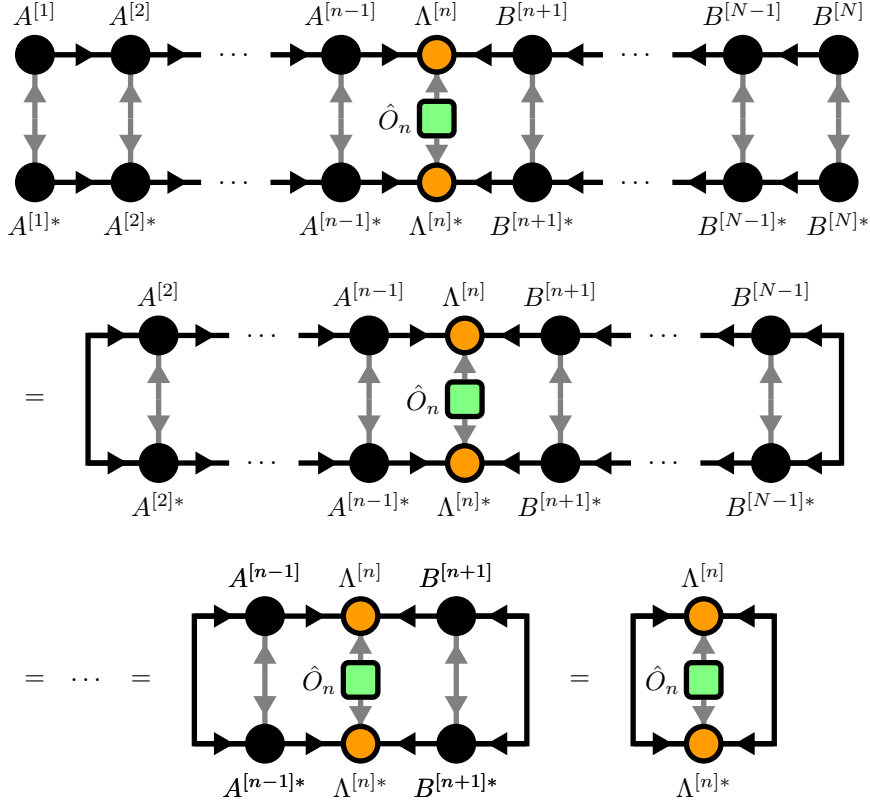


Figure 2.9: If the MPS is in canonical form, the computation of the expectation value of a local operator can be simplified to a contraction of only three tensors using the isometry condition.

2.3. Additionally, this SVD at the orthogonality center is related to the Schmidt decomposition of a bipartite system

$$|\Psi\rangle = \sum_{\alpha=1}^{\chi_n} \lambda_{\alpha} |\Psi_{\alpha}^{[L]}\rangle \otimes |\Psi_{\alpha}^{[R]}\rangle,$$

where the chain is split into a left and right subsystem, grouping all indices to the left and right of the orthogonality center into orthogonal basis vectors $|\Psi_{\alpha}^{[L]}\rangle$ and $|\Psi_{\alpha}^{[R]}\rangle$ respectively. In this case, the Schmidt values $\lambda_{\alpha} \geq 0$ coincide with the singular values [13] and one can compute the Von-Neumann entanglement entropy

$$S = - \sum_{\alpha=1}^{\chi_n} \lambda_{\alpha}^2 \log(\lambda_{\alpha}^2),$$

quantifying the amount of entanglement between the left and right subsystem. If the state is normalized, it additionally holds

$$\sum_{\alpha=1}^{\chi_n} \lambda_{\alpha}^2 = 1.$$

Thus, how well an MPS of a given bond dimension χ_{\max} is able to represent a given quantum state is highly dependent on the Schmidt spectrum $\{\lambda_{\alpha}\}$ at the different bipartitions of the chain. If the Schmidt values decrease exponentially, only an exponentially small part of the entanglement structure is truncated and the MPS is a good approximation for the original state. It can be shown [15, 16] that for ground states of local, gapped, one dimensional Hamiltonians there holds an *area law*: The entanglement entropy at arbitrary bipartitions of the chain is bounded by a constant

$$S \leq S_{\max},$$

where S_{\max} is independent of the system size. This is in contrast to the fact that the entanglement of states drawn randomly from the many-body Hilbert space on average exhibits *volume law* scaling

$$\mathbb{E}[S] > \min(N_L, N_R) \log(d),$$

where N_L and N_R are the number of subsystems in the left and right bipartition. Hence, ground states of gapped Hamiltonians are very non-generic. Note that the constant S_{\max} scales with the correlation length of the system, which diverges when approaching critical points.

It is immediately clear that truncated MPS by construction exhibit area law entanglement scaling if the local subsystems that are represented by each tensor correspond to physical systems on a 1D chain. The maximal entanglement entropy for a bipartition can be reached when all Schmidt values are equal, i.e. $\lambda_{\alpha} = 1/\sqrt{\chi_n}$ for $\alpha = 1, \dots, \chi_n$, and thus

$$S \leq \log(\chi_{\max})$$

for arbitrary bipartitions of the chain. One can conclude that MPS are good approximations for ground states of gapped 1D Hamiltonians away from criticality.

For completeness we note that the truncation of all bonds of an MPS is a highly non-linear optimization problem and the naive algorithm of truncating each bond with an SVD does in general not lead to a minimal error. A variational compression procedure can be used to obtain a lower error at the same maximum bond dimension χ_{\max} [13].

Time Evolution

Many algorithms have been formulated in the language of MPS. Most notably, the Density Matrix Renormalization Group (DMRG) algorithm can be used for finding ground states of local lattice Hamiltonians [13]. Time evolution of MPS can for example be performed with the Time Evolving Block Decimation (TEBD) algorithm [18, 39] or the Time Dependant Variational Principle (TDVP) [19, 40]. In the following, we will briefly discuss TEBD, as this algorithm can be generalized easily to isometric tensor product states of higher dimensions, which we will discuss in Section 3.3.

Assume that we are given a quantum state $|\Psi\rangle$ in the form of an MPS and a Hamiltonian \hat{H} that can be written as a sum of nearest-neighbor operators $\hat{h}^{[j,j+1]}$,

$$\hat{H} = \sum_{j=1}^{N-1} \hat{h}^{[j,j+1]}.$$

According to the Schrödinger equation, the state $|\Psi\rangle$ can be evolved in time as

$$|\Psi(t)\rangle = \hat{U}(t) |\Psi\rangle = e^{-it\hat{H}} |\Psi\rangle,$$

where we have set $\hbar = 1$. The time evolution operator $\hat{U}(t)$ is in general very hard to compute and handle exactly. Thus, $\hat{U}(t)$ is approximated using a *Suzuki-Trotter decomposition*. We start by decomposing the time evolution into a series of K small time steps $\Delta t = t/K$ as

$$\hat{U}(t) = e^{-it\hat{H}} = \left(e^{-i\Delta t\hat{H}} \right)^K = \left(\hat{U}(\Delta t) \right)^K.$$

Next, we split the Hamiltonian into terms acting on even and odd bonds

$$\hat{H} = \sum_{j \text{ even}} \hat{h}^{[j,j+1]} + \sum_{j \text{ odd}} \hat{h}^{[j,j+1]} =: \hat{H}_{\text{even}} + \hat{H}_{\text{odd}}.$$

We can then use the *Zassenhaus formula*

$$e^{\varepsilon(\hat{A}+\hat{B})} = e^{\varepsilon\hat{A}} e^{\varepsilon\hat{B}} e^{-\frac{\varepsilon^2}{2}[\hat{A},\hat{B}]} e^{\frac{\varepsilon^3}{6}(2[\hat{B},[\hat{A},\hat{B}]] + [\hat{A},[\hat{A},\hat{B}]])} \dots$$

which can be derived from the Baker-Campbell-Hausdorff formula, to approximate

$$\begin{aligned} \hat{U}(\Delta t) &= e^{-i\Delta t(\hat{H}_{\text{even}} + \hat{H}_{\text{odd}})} = e^{-i\Delta t\hat{H}_{\text{even}}} e^{-i\Delta t\hat{H}_{\text{odd}}} + \mathcal{O}(\Delta t^2) \\ &= \hat{U}^{\text{TEBD1}}(\Delta t) + \mathcal{O}(\Delta t^2). \end{aligned} \tag{2.12}$$

This is called a Suzuki-Trotter decomposition of first order. Since operators acting

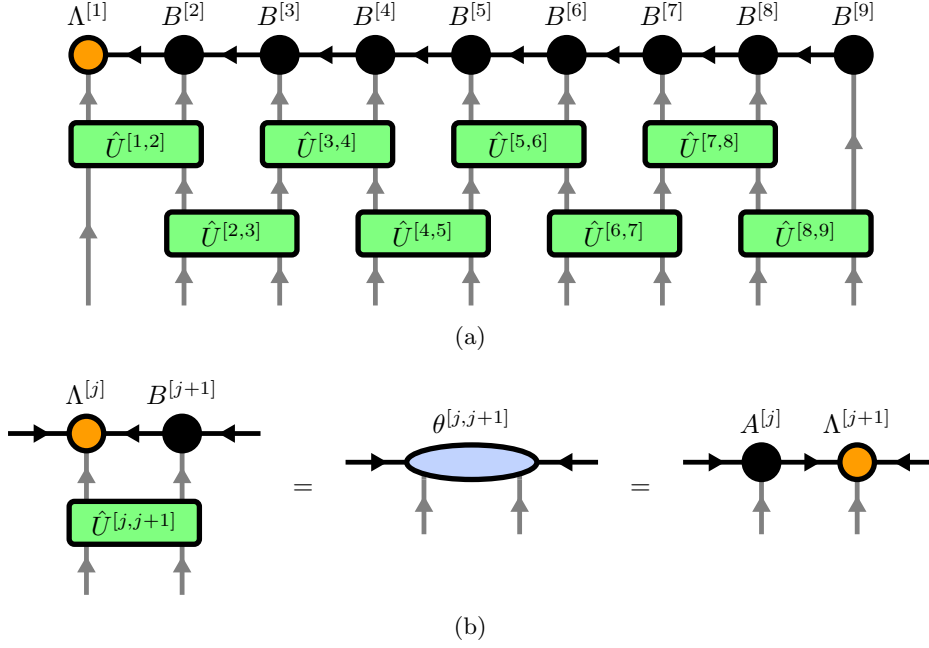


Figure 2.10: (a) An MPS can be approximately evolved by a time Δt by applying the first order TEBD operator (2.12), which is made up of bond operators acting first on all even and then on all odd bonds. (b) To apply a single bond operator $\hat{U}^{[j,j+1]}$, the two corresponding tensors $\Lambda^{[j]}$ and $B^{[j+1]}$ are contracted with the operator into a tensor $\theta^{[j,j+1]}$, which is then split using truncated SVD to obtain the updated tensors $A^{[j]}$ and $\Lambda^{[j+1]}$.

on even bonds commute with each other, the exponential $e^{-i\Delta t \hat{H}_{\text{even}}}$ factorizes,

$$e^{-i\Delta t \hat{H}_{\text{even}}} = e^{-i\Delta t \sum_{j \text{ even}} \hat{h}^{[j,j+1]}} = \prod_{j \text{ even}} e^{-i\Delta t \hat{h}^{[j,j+1]}},$$

and the same holds for the exponential $e^{-i\Delta t \hat{H}_{\text{odd}}}$. Each bond operator $\hat{U}^{[j,j+1]} := e^{-i\Delta t \hat{h}^{[j,j+1]}}$ acting on the combined Hilbert space of sites j and $j+1$ can be reshaped into a tensor of rank 4. The application of the operator $\hat{U}^{\text{TEBD1}}(\Delta t)$ to a state in MPS form can then be written as the tensor network in Figure 2.10a. To perform a single TEBD iteration corresponding to a time evolution of Δt , we want to approximate this tensor network by a new MPS. This can be done by moving the orthogonality center from left to right, applying the bond operators $\hat{U}^{[j,j+1]}$ while keeping the MPS structure. The process of applying a single bond operator is shown in Figure 2.10b. First, the orthogonality center is moved to site j . The two site tensors $\Lambda^{[j]}$ and $B^{[j+1]}$ are then contracted with the bond operator $\hat{U}^{[j,j+1]}$ into a single tensor θ , which is subsequently split and truncated using an SVD. By sweeping twice across the MPS, first applying the bond operators on all even bonds and then the bond

operators on all odd bonds, we perform a full TEBD iteration. There exist two sources of errors, the truncation error of the truncated SVD and the error of the Suzuki-Trotter decomposition. The truncation error can be controlled by choosing a larger bond dimension χ , allowing the representation of more entanglement and thus the evolution to larger times. However, generally the amount of entanglement grows exponentially in time [13], necessitating an exponentially growing bond dimension and practically limiting the algorithm to small times. A smaller Suzuki-Trotter error can be achieved by choosing smaller time steps Δt or by performing a higher-order Suzuki-Trotter decomposition. For example, a second order decomposition can be computed by symmetrizing two first-order decompositions of time step $\Delta t/2$ as

$$\begin{aligned}\hat{U}(\Delta t) &= e^{-i\Delta t(\hat{H}_{\text{even}}+\hat{H}_{\text{odd}})} = e^{-i\frac{\Delta t}{2}\hat{H}_{\text{even}}}e^{-i\Delta t\hat{H}_{\text{odd}}}e^{-i\frac{\Delta t}{2}\hat{H}_{\text{even}}} + \mathcal{O}(\Delta t^3) \\ &= \hat{U}^{\text{TEBD2}}(\Delta t) + \mathcal{O}(\Delta t^3).\end{aligned}$$

and can be applied to an MPS similarly as the first order decomposition. For higher order Suzuki-Trotter decompositions see [41].

2.5 Isometric Tensor Product States (isoTPS) in 2D

The natural generalization of MPS to higher dimensional lattices is given by *Projected Entangled Pair States* (PEPS) [22, 42]. A PEPS is constructed similar to an MPS by representing the local subsystem on each lattice site j with the index i_j of a tensor $T^{[j],i_j}$ and connecting nearest-neighbor tensors with virtual bonds. The maximum bond dimension of virtual bonds is called D and controls both the representational power of the PEPS and the computational cost of algorithms. The full quantum state can be written as

$$|\Psi\rangle = \sum_{i_1, i_2, \dots, i_N} \mathcal{C}\left(T^{[1],i_1}, T^{[2],i_2}, \dots, T^{[N],i_N}\right) |i_1, i_2, \dots, i_N\rangle,$$

where $\mathcal{C}(\dots)$ denotes the contraction of the full network along all virtual bonds. As an example, we draw a PEPS on a square lattice in Figure 2.11a.

PEPS are able to efficiently represent area law states in two and higher dimensions [14]. Remarkably, PEPS can even represent certain states with correlations decaying polynomially with separation distance [43], whereas MPS can only handle exponentially decaying correlations. Polynomially decaying correlations are characteristic for critical points.

Unfortunately, it is not generally possible to bring a PEPS into an exact canonical form due to the presence of closed loops. Because of this, already the computation of local expectation values scales exponentially with system size and can only be computed approximately in practice, e.g., using the boundary MPS method [14] or

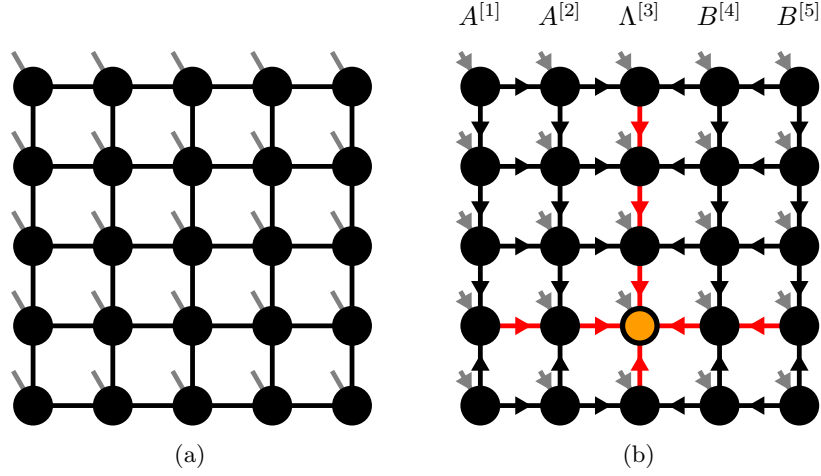


Figure 2.11: Tensor Networks representing two dimensional quantum states on a square lattice. (a) A Projected Entangled Pair State (PEPS). (b) An isometric Tensor Product State (isoTPS). The orthogonality hypersurface is drawn in red and the orthogonality center in orange.

corner transfer matrices [44]. Moreover, algorithms for ground state search and time evolution have computational costs scaling with high powers of the bond dimension. For example, the cost of a full update TEBD iteration is dominated by the contraction of an effective environment, scaling as $\mathcal{O}(D^{10})$ [21].

Recently, the new class of *isometric Tensor Product States* (isoTPS) has been introduced [23–25], generalizing the canonical form of MPS to higher dimensions by enforcing isometry constraints. In the following, we will give a brief introduction to the isoTPS defined in [23]. A two-dimensional isoTPS on the square lattice is constructed by enforcing the isometry conditions shown in Figure 2.11b. The isometries are chosen in such a way that all arrows point towards a special row and column, called the *orthogonality hypersurface* of the isoTPS. The term *hypersurface* is chosen in anticipation of a generalization to higher dimensions. The maximum bond dimension of bonds along the orthogonality hypersurface is increased to $\chi = f \cdot D$, where $f \geq 1$ is a positive integer. In practice, this can produce better results at similar computational costs than increasing the maximum bond dimension for all bonds of the lattice [26].

Because of the isometry condition, one can think of the contractions of each of the four regions outside the orthogonality hypersurface as orthogonal boundary maps [26]. The single tensor with only incoming arrows is called the *orthogonality center*. Local expectation values of operators acting in the vicinity of the orthogonality center can be computed efficiently because most contractions reduce to identity, similar to the computation of local expectation values in MPS. The orthogonality

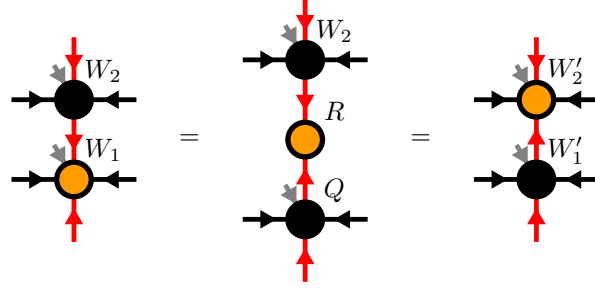


Figure 2.12: Moving the orthogonality center along the orthogonality hypersurface can be done easily via a single QR-decomposition. First, the orthogonality center is split as $W_1 = QR = W'_1 R$. The tensors W_2 and R are then contracted to form the new orthogonality center W'_2 .

center can be moved along the orthogonality hypersurface simply and exactly using a QR-decomposition as shown in Figure 2.12.

Moving the orthogonality surface is a harder problem, which can in general only be done approximately. In analogy to MPS and as shown in Figure 2.11b, we call columns left of the orthogonality hypersurface $A^{[n]}$ and columns right of the orthogonality hypersurface $B^{[n]}$, with $n = 1, 2, \dots, L$ and L the linear system size. Moving the orthogonality hypersurface $\Lambda^{[n]}$ one column to the right can be expressed as solving the problem

$$\Lambda^{[n]} B^{[n+1]} \approx A^{[n]} \Lambda^{[n+1]}, \quad (2.13)$$

where the notation $\Lambda^{[n]} B^{[n+1]}$ denotes the contraction of columns $\Lambda^{[n]}$ and $B^{[n+1]}$

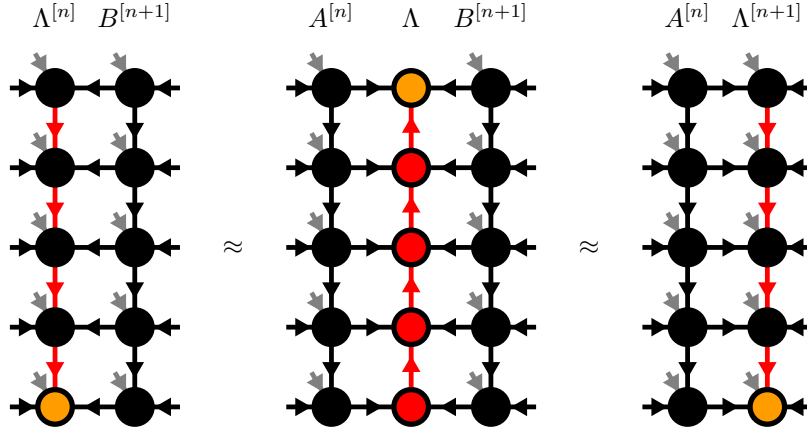


Figure 2.13: The orthogonality hypersurface can be moved to the right by first solving Equation (2.14) variationally and then absorbing Λ into $B^{[n+1]}$ via the standard MPO-MPS multiplication and MPS compression algorithms.

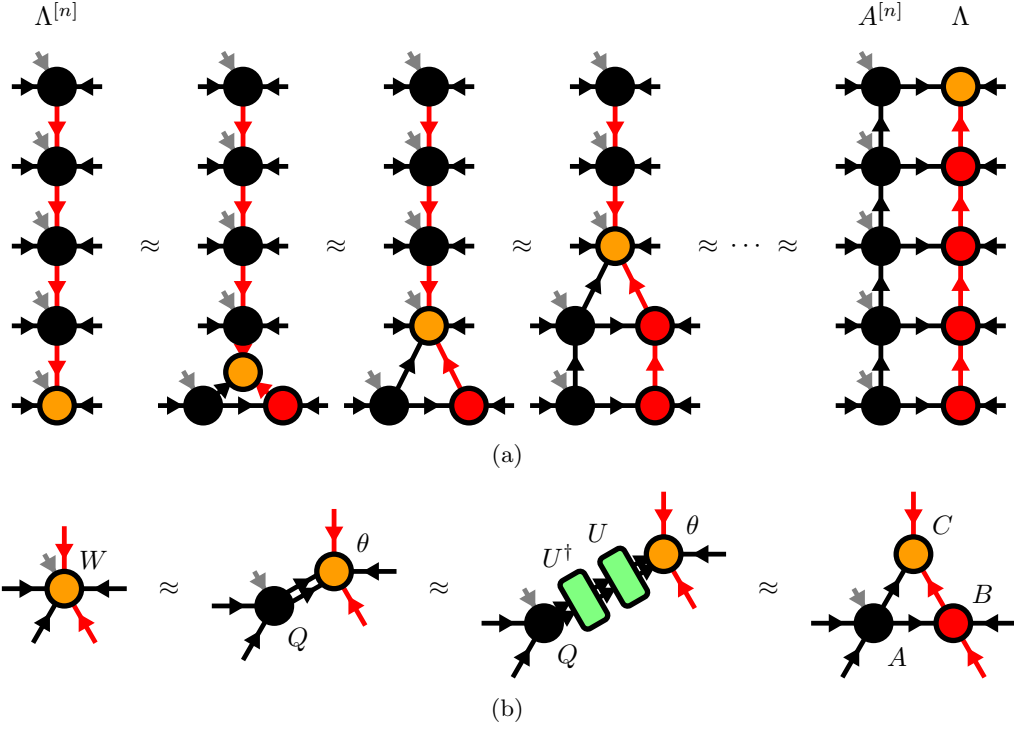


Figure 2.14: (a) The Moses Move (MM) splits the column $\Lambda^{[n]}$ into $A^{[n]}$ and Λ via a single unzipping sweep of tripartite decompositions. (b) Tripartite decomposition of the tensor W as explained in the text.

along their connecting bonds. Instead of (2.13), one can solve the simpler auxiliary problem

$$\Lambda^{[n]} = A^{[n]} \Lambda, \quad (2.14)$$

where Λ is a column of tensors with no physical indices, as shown in Figure 2.13. This column can then be absorbed into $B^{[n+1]}$ via the standard algorithm of applying a Matrix Product Operator (MPO) to an MPS and subsequently compressing the MPS to the maximal bond dimension [13] to form the new orthogonality hypersurface $\Lambda^{[n+1]}$. One can variationally solve problem (2.14) by minimizing the distance $\|\Lambda^{[n]} - A^{[n]} \Lambda\|$, sweeping over all tensors of the columns $A^{[n]}$ and Λ and performing local optimizations while respecting the isometry condition. This is known as an Evenbly-Vidal style variational optimization and is discussed in more detail in Appendix A. It is however found in [23] that a single unzipping sweep, called the *Moses Move* (MM), provides a solution very close to the variational one whilst being far quicker. The MM can also be used as a good initialization for the variational algorithm. We sketch the MM in Figure 2.14a. Starting from the bottom of the orthogonality hypersurface column,

the tensors are split one after the other using tripartite decompositions. A single tripartite decomposition of a tensor W is shown in Figure 2.14b. First, W is split into two tensors Q and θ via a truncated SVD $W = U(SV) = Q\theta$, where Q is an isometry. The bond connecting Q and θ is then reshaped into two bonds of bond dimension $< D$. Next, it is important to note that the full contraction is invariant under the insertion of a unitary U and its conjugate transpose, $Q\theta = (QU^\dagger)(U\theta)$, with $A = QU^\dagger$ still satisfying the isometry condition. This degree of freedom can be used to *disentangle* the tensor θ along the vertical direction. Accordingly, we choose U such that the truncation error or some entanglement measure is minimized for splits of θ along this direction. Choosing a good disentangling unitary is crucial for a successful tripartite decomposition and will be discussed further in Section 3.2. Assume for now that a good disentangling unitary has been found. After contracting QU^\dagger and $U\theta$, a truncated SVD is used to split $U\theta$ into tensors B and C as shown in Figure 2.14b, completing the tripartite decomposition. The computational cost of the MM scales with the maximum bond dimension D as $\mathcal{O}(D^7)$ [23, 26].

Because the orthogonality center can be moved easily along the orthogonality hypersurface, one can think of the orthogonality hypersurface along a column or row as a 1D MPS with an enlarged physical bond dimension grouping together the physical and the two auxiliary legs protruding from the orthogonality hypersurface tensors. Standard MPS algorithms can then be generalized to isoTPS by performing one iteration of the algorithm on the orthogonality hypersurface MPS, before moving the hypersurface via the MM and repeating the procedure. As an example, we will discuss TEBD², the generalization of TEBD to an isoTPS on a 2D square lattice. The Hamiltonian \hat{H} is split into terms acting on columns and rows,

$$\hat{H} = \sum_{x=1}^{L_x} \hat{H}_x + \sum_{y=1}^{L_y} \hat{H}_y,$$

and the time evolution operator is replaced by the first order approximation

$$\hat{U}^{\text{TEBD1}}(\Delta t) = \prod_{y=1}^{L_y} e^{-i\Delta t \hat{H}_y} \prod_{x=1}^{L_x} e^{-i\Delta t \hat{H}_x}.$$

If the orthogonality hypersurface $\Lambda^{[x]}$ is at column x , the operator $e^{-i\Delta t \hat{H}_x}$ can easily be applied by calling the standard 1D TEBD algorithm at a cost of $\mathcal{O}(D^6)$ [23]. To evolve the full isoTPS, we start with the orthogonality center in the bottom left corner and apply first the time evolution operators along all columns, moving from left to right using the MM. We then rotate the lattice by 90° , turning rows into columns and columns into rows. Moving back from right to left we now apply the time evolution operators along the rows, completing the time step.

The computational cost of the full TEBD² algorithm scales as $\mathcal{O}(D^7)$. The algorithm can be easily improved to second order by symmetrizing the time evolution [26].

Chapter 3

IsoTPS with Alternative Canonical Form

In the following, we introduce an alternative way of defining the canonical form for isometric tensor product states, which has some important differences to the isoTPS discussed in Section 2.5. We start by introducing this canonical form in Section 3.1. To move the orthogonality hypersurface, a new algorithm must be implemented, which we call the *Yang-Baxter* (YB) move and discuss in Section 3.2. Finally, in Section 3.3 we generalize the TEBD algorithm to this new canonical form.

3.1 Network Structure

The structure of an isoTPS in the alternative canonical form on a square lattice is shown in Figure 3.1. It can be constructed in three steps. First, a square PEPS is rotated by 45° . Next, the orthogonality hypersurface is constructed as a column of auxiliary tensors. The auxiliary tensors are connected in a line similar to an MPS and placed between two columns of PEPS tensors. Note that, in contrast to the original isoTPS, the tensors of the orthogonality hypersurface do not carry any physical degrees of freedom and only have virtual indices. Lastly, the isometry condition is enforced such that all arrows point towards the orthogonality hypersurface. Tensors left of the orthogonality hypersurface are thus brought into a left-isometric form and tensors right of the orthogonality hypersurface are brought into a right-isometric form, as shown in Figure 3.1. The auxiliary tensors making up the orthogonality hypersurface are isometrized such that all arrows point towards a single auxiliary tensor, the orthogonality center. We further impose that the quantum state represented by the isoTPS is normalized to one. Because of the isometry condition, this reduces to the constraint that the orthogonality center must be a tensor of norm one.

In the following, we will denote the auxiliary tensors by W_j , and the tensors carrying physical degrees of freedom by T_j . The bonds connecting two T -tensors or a T -tensor and a W -tensor are truncated to a maximal bond dimension of D , while the maximal bond dimension between two W -tensors is denoted as χ . Similar to the original isoTPS it is found that setting $\chi = f \cdot D$ with an integer $f \geq 1$ produces

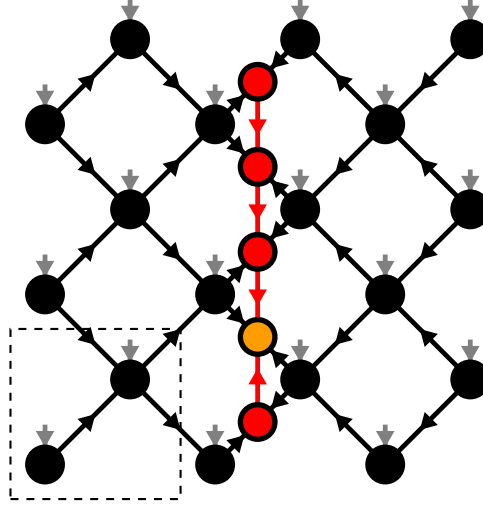


Figure 3.1: An isometric tensor product state in the alternative canonical form on a 3×3 diagonal square lattice is constructed from site tensors T_j (drawn in black) and an orthogonality hypersurface of auxiliary tensors W_j (drawn in red). The orthogonality hypersurface is rotated by 45° with respect to the lattice. The dashed lines denote a single unit cell. The single tensor in the orthogonality hypersurface with only incoming arrows is called the orthogonality center (drawn in orange). The maximal bond dimension of virtual bonds (drawn in black) is D , the maximal bond dimension of auxiliary bonds (drawn in red) is $\chi = f \cdot D$, and the bond dimension of physical indices (drawn in gray) is d .

good results in practice. We denote the dimension of the physical indices by d in analogy to MPS and isoTPS.

Similar to the original isoTPS, the orthogonality center can easily and exactly be moved along the orthogonality hypersurface using QR-decompositions, compare Figure 2.12. Moving the orthogonality hypersurface to the left or to the right is a harder problem and will be discussed in Section 3.2.

Similar to MPS and the original isoTPS, isoTPS in this alternative canonical form allow for the fast computation of expectation values of local operators. The expectation value $\langle \Psi | \hat{O}_i | \Psi \rangle$ of a one-site operator \hat{O}_i acting on site i can be computed as follows: First, the orthogonality center is moved next to site i . We then define the *one-site wave function* as the sub-network containing the site tensor T_i and the two connected W -tensors. Note that the one-site wave function is connected to its environment only by bonds with incoming arrows. Next, the wave function is contracted with its complex conjugate, sandwiching the operator \hat{O}_i between the two. Due to the isometry condition this reduces to a contraction of only the one-site wave function, its complex conjugate, and the operator \hat{O}_i , as shown in Figure 3.2.

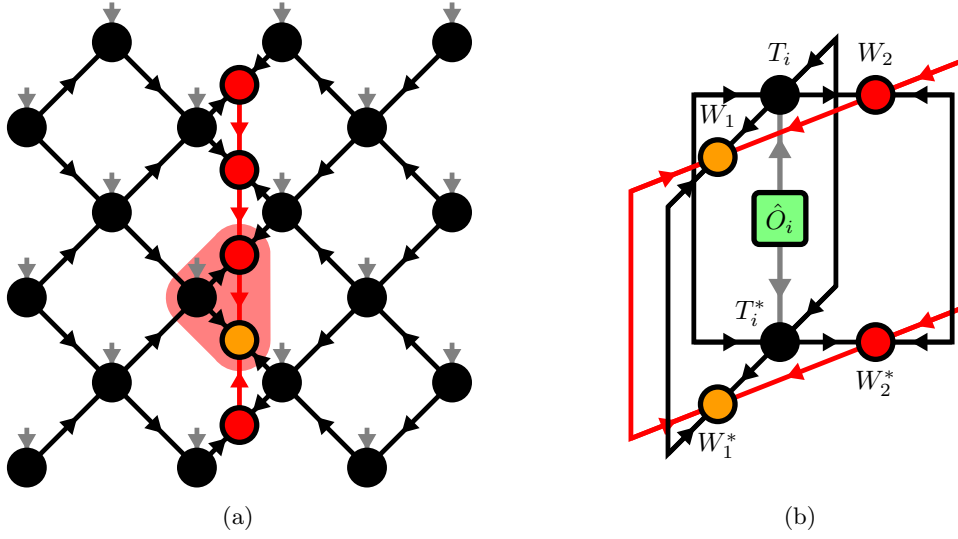


Figure 3.2: (a) The one-site wave function around a site i is the sub-network containing the site tensor T_i and the two connected auxiliary tensors. (b) The computation of a one-site expectation value reduces to the shown contraction over the one-site wave function, its complex conjugate, and the one-site operator \hat{O}_i .

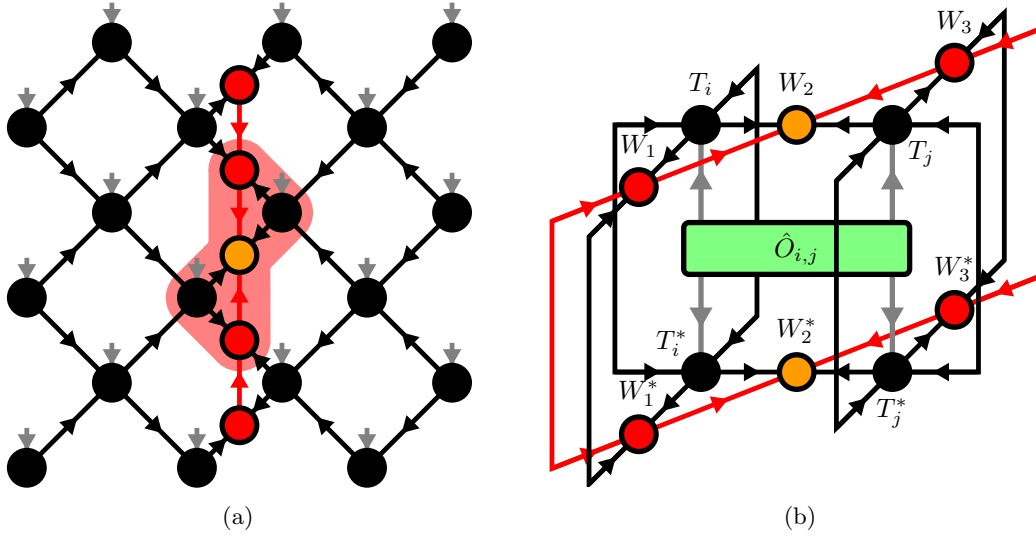


Figure 3.3: (a) The two-site wave function around neighboring sites i and j is the sub-network containing the site tensors T_i and T_j and the three connected auxiliary tensors. (b) The computation of a two-site expectation value reduces to the shown contraction over the two-site wave function, its complex conjugate, and the two-site operator $\hat{O}_{i,j}$.

The contraction has a computational cost scaling as $\mathcal{O}(\chi^3 D^3 + D^6 d^2) = \mathcal{O}(D^6)$ and gives as result the desired expectation value.

The expectation value $\langle \Psi | \hat{O}_{i,j} | \Psi \rangle$ of a two-site bond operator $\hat{O}_{i,j}$ acting on two neighboring sites i and j can be computed similarly. First, the orthogonality center is moved such that it sits in the middle of the bond connecting sites i and j . The *two-site wave function* is then defined as the sub-network containing the two T -tensors T_i and T_j and three W -tensors as shown in Figure 3.3, such that again all legs connecting the sub-network to its environment are only decorated with arrows pointing towards the two-site wave function. The computation of the expectation value then reduces to the contraction of only the two-site wave function, its complex conjugate and the bond operator $\hat{O}_{i,j}$. The computational cost of this contraction scales as $\mathcal{O}(\chi^3 D^3 d^2) = \mathcal{O}(D^6)$.

3.2 Yang-Baxter Move

Most algorithms implemented on isoTPS require an efficient procedure for moving the orthogonality surface, where the error introduced by this procedure should be as small as possible. For the original isoTPS discussed in Section 2.5, the current best procedure is given by the Moses Move, followed by an optional variational optimization.

In analogy to the MM we look for a procedure to iteratively shift the orthogonality surface through one column of T -tensors as shown in Figure 3.4. A single iteration of this process is shown in Figure 3.5. The two tensors W_1 and W_2 , which are part of the orthogonality hypersurface, are "pulled through" the site tensor T , resulting in updated tensors T' , W'_1 and W'_2 . To keep the isometric structure of the network, T' and W'_1 must be isometries and W'_2 must be a tensor of norm one (the new orthogonality center). Due to the visual similarity to the Yang-Baxter equation we call this procedure the *Yang-Baxter* (YB) move. Accordingly, we will in the following refer to isoTPS with the diagonal canonical form as YB-isoTPS, while the original isoTPS are referred to as MM-isoTPS.

We denote the state represented by the YB-isoTPS before the YB move by $|\Psi\rangle = |\Psi(W_1, W_2, T)\rangle$ and the state after the YB move by $|\Psi'\rangle = |\Psi'(W'_1, W'_2, T')\rangle$. One can think of the YB move as an optimization problem

$$(T'_{\text{opt}}, W'_{1,\text{opt}}, W'_{2,\text{opt}}) = \underset{T', W'_1, W'_2}{\operatorname{argmin}} \|\Psi\rangle - |\Psi'\rangle\| \quad (3.1)$$

under the constraints

$$T'^{\dagger} T' = \mathbb{1}, \quad W_1'^{\dagger} W'_1 = \mathbb{1}, \quad \|W'_2\|_{\text{F}} = 1. \quad (3.2)$$

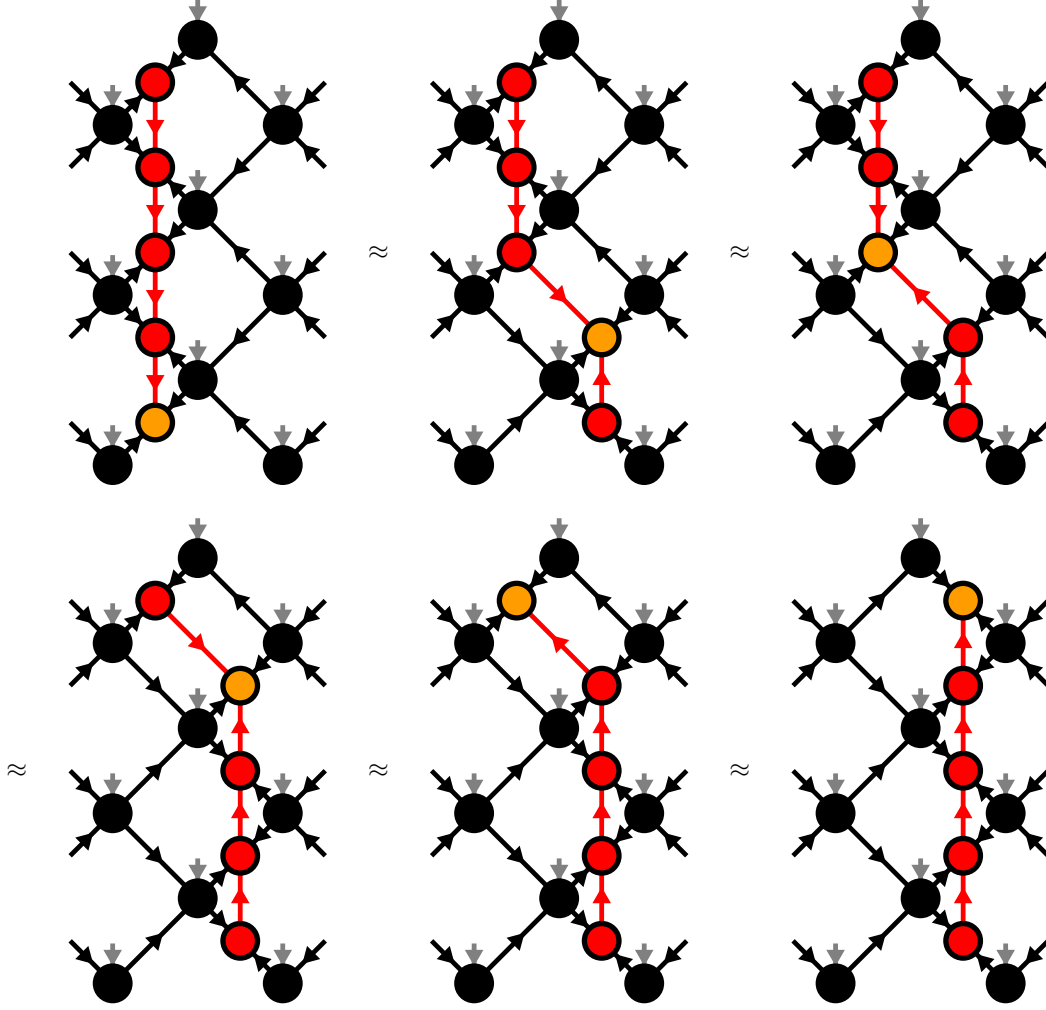


Figure 3.4: Two YB-moves are used to shift the orthogonality hypersurface one column to the right. In the last step, the orthogonality center can be moved across the T -tensor by simply contracting the two tensors and performing a truncated SVD.

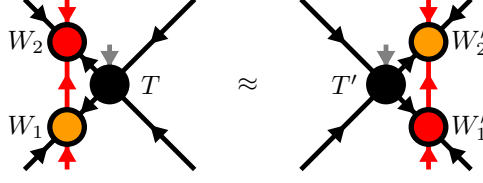


Figure 3.5: The Yang-Baxter (YB) move is the procedure of "pulling" two auxiliary tensors W_1 and W_2 through a site tensor T .

The error of the YB move can be rewritten as

$$\begin{aligned} \|\Psi - \Psi'\| &= \sqrt{\langle \Psi | \Psi \rangle + \langle \Psi' | \Psi' \rangle - 2 \operatorname{Re} \langle \Psi' | \Psi \rangle} \\ &= \sqrt{2 - 2 \operatorname{Re} \langle \Psi' | \Psi \rangle}, \end{aligned}$$

where in the second step we used the fact that the wave function is normalized to one, $\langle \Psi | \Psi \rangle = \langle \Psi' | \Psi' \rangle = 1$. It follows that the optimization problem of minimizing the error becomes the problem of maximizing the overlap

$$(T'_{\text{opt}}, W'_{1,\text{opt}}, W'_{2,\text{opt}}) = \operatorname{argmax}_{T, W'_1, W'_2} \operatorname{Re} \langle \Psi' | \Psi \rangle \quad (3.3)$$

under the constraints (3.2). Because the only tensors that are changed by the YB move are W_1 , W_2 and T and the three tensors make up a subregion of the full network with only incoming arrows, we can use the isometry condition to reduce the computation of the overlap $\langle \Psi' | \Psi \rangle$ to a contraction of only six tensors as shown in Figure 3.6.

In the following, we present two explicit algorithms for performing the YB move. The first algorithm (see Section 3.2.1) is an Evenly-Vidal-style variational optimization method with iterative local updates. The second algorithm (see Section 3.2.2) is a tripartite decomposition with disentangling similar to the tripartite decomposition used in the MM. In Section 3.2.3 we will compare the two algorithms.

3.2.1 Variational Optimization with Local Updates

To solve the constrained optimization problem (3.3) we proceed by maximizing the overlap while only varying the parameters of one of the three tensors T' , W'_1 or W'_2 , treating all other tensors as constant. For example, let us keep W'_1 and W'_2 fixed and optimize T' . We first contract all tensors except T' into an environment E as shown in Figure 3.7a. We can then write the optimization problem as

$$T'_{\text{opt}} = \operatorname{argmax}_{T'^{\dagger} T = \mathbb{1}} \operatorname{Re} \langle \Psi' | \Psi \rangle = \operatorname{argmax}_{T'^{\dagger} T' = \mathbb{1}} \operatorname{Re} \langle T', E \rangle_{\text{F}} = \operatorname{argmax}_{T'^{\dagger} T' = \mathbb{1}} \operatorname{Re} \operatorname{Tr} (T'^{\dagger} E).$$

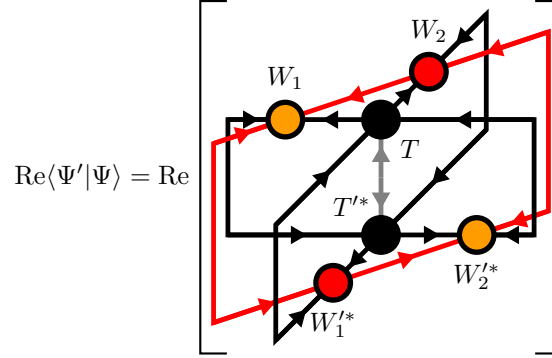


Figure 3.6: The cost function of the optimization problem (3.3) can be computed as a contraction of only six tensors.

This problem is known as the *orthogonal Procrustes problem* and permits the closed form solution $T'_{\text{opt}} = UV^\dagger$, where U and V are computed using the SVD $E = USV^\dagger$. For the derivation of this solution see Appendix A. The tensors W'_1 and W'_2 can be optimized similarly. The full algorithm is then performed by sweeping over the three tensors, optimizing them iteratively until convergence. Tensor diagrams for the algorithm are shown in Figure 3.7. We discuss one iteration of the algorithm in more detail:

1. Contract all tensors except T' into an environment E and perform an SVD $E = USV$. The tensor T' is then updated as $T' \leftarrow UV^\dagger$. See Figure 3.7a.
2. Contract all tensors except W'_1 into an environment E and perform an SVD $E = USV$. The tensor W'_1 is then updated as $W'_1 \leftarrow UV^\dagger$. See Figure 3.7b.
3. Contract all tensors except W'_2 into an environment E . The tensor W'_1 is then updated as $W'_1 \leftarrow E / \|E\|$. See Figure 3.7c.

These three steps are repeated until a termination criterion is met, for example until the decrease in error after one iteration is smaller than a given threshold or if a given maximum number of iterations $N_{\text{iter,YB}}$ is exceeded. A similar algorithm was also used by Evenbly and Vidal in the context of the multi-scale entanglement renormalization ansatz (MERA) [45, 46]. Note that in step 3 of the algorithm, a norm constraint is enforced instead of an isometry constraint, in which case the closed form solution takes a different shape. We also derive this solution in Appendix A.

The computational cost of the algorithm is dominated by the tensor contractions, scaling as $\mathcal{O}(3N_{\text{iter}}(\chi^2 D^6 d + \chi^3 D^4)) = \mathcal{O}(N_{\text{iter}} D^8)$ for one YB move.

In practice we observe that the discussed algorithm converges only very slowly. To qualitatively showcase this, we perform the YB move on a typical environment of

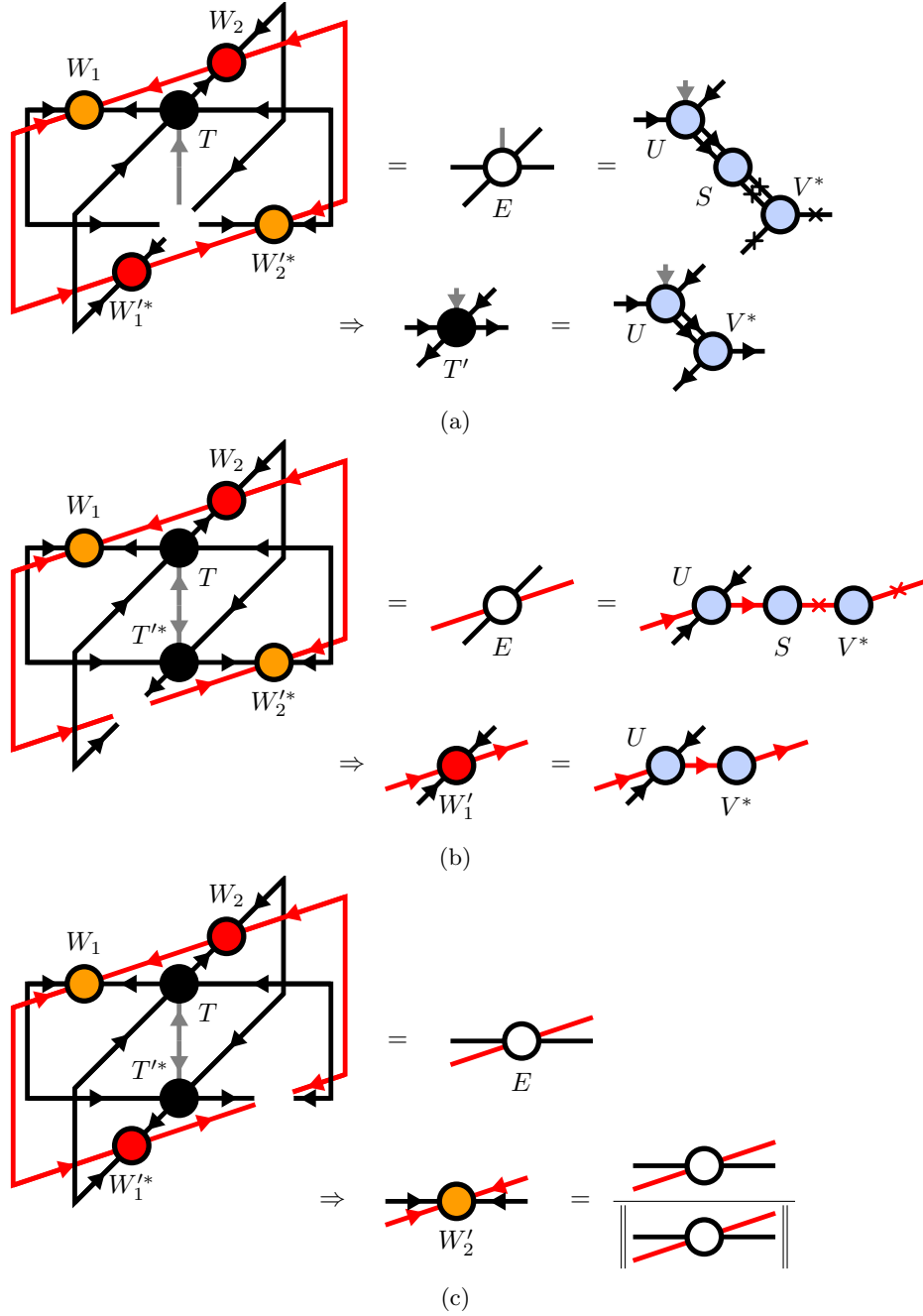


Figure 3.7: In this figure we show the three local updates that are used to iteratively solve optimization problem (3.3). (a) The tensor T' is updated by contracting all tensors except T' into the environment E and isometrizing E using an SVD. (b) The tensor W_1' can be updated similarly by contracting all tensors except W_1' into the environment E , which is subsequently isometrized using an SVD. (c) To optimize the tensor W_2' , all tensors except W_2' are contracted into the environment E . The updated tensor is then given as $W_2' = E / \|E\|$.

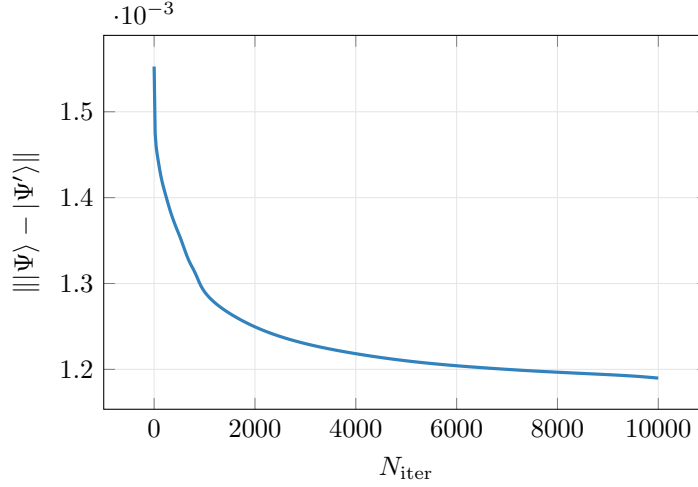


Figure 3.8: In this figure we plot the YB error against the number of iterations N_{iter} of the iterative YB move. The YB move is performed on an environment of tensors that were obtained during imaginary TEBD on the TFI model, see Chapter 5. The algorithm converges only very slowly.

tensors $\{W_1, W_2, T\}$ that was encountered during imaginary time evolution of the Transverse Field Ising model, see Chapter 5 for more details. The bond dimensions chosen for the YB-isoTPS are $D = 4$, $\chi = 24$. We plot the error $|||\Psi\rangle - |\Psi'\rangle||$ against the number of iterations in Figure 3.8. After $N_{\text{iter}} = 10000$ iterations, the algorithm is still not converged.

3.2.2 Tripartite Decomposition Using an SVD and Disentangling

Alternatively, the constrained optimization problem (3.1) can be solved via two successive SVDs with an optional disentangling procedure with the goal of reducing the truncation error or some entanglement measure. This is a similar algorithm to the one used for the MM in isoTPS [23, 26], compare Section 2.5. The algorithm is sketched in Figure 3.9 and is made up of three main steps.

1. We start by contracting the tensors T , W_1 and W_2 into a single tensor Ψ at a cost of $\mathcal{O}(\chi^3 D^4 + \chi^2 D^6 d) = \mathcal{O}(D^8 d)$. This tensor is then split from left to right via a truncated SVD

$$\Psi = ASV^\dagger = A(SV^\dagger) =: A\theta$$

as shown in Figure 3.9a. Here, the bond connecting A and θ has a bond dimension of $\min(dD^2, \chi^2 D^2)$. The bond dimension is truncated to D^2 . The cost of the SVD is $\mathcal{O}(\chi^2 D^6 d^2) = \mathcal{O}(D^8 d^2)$.

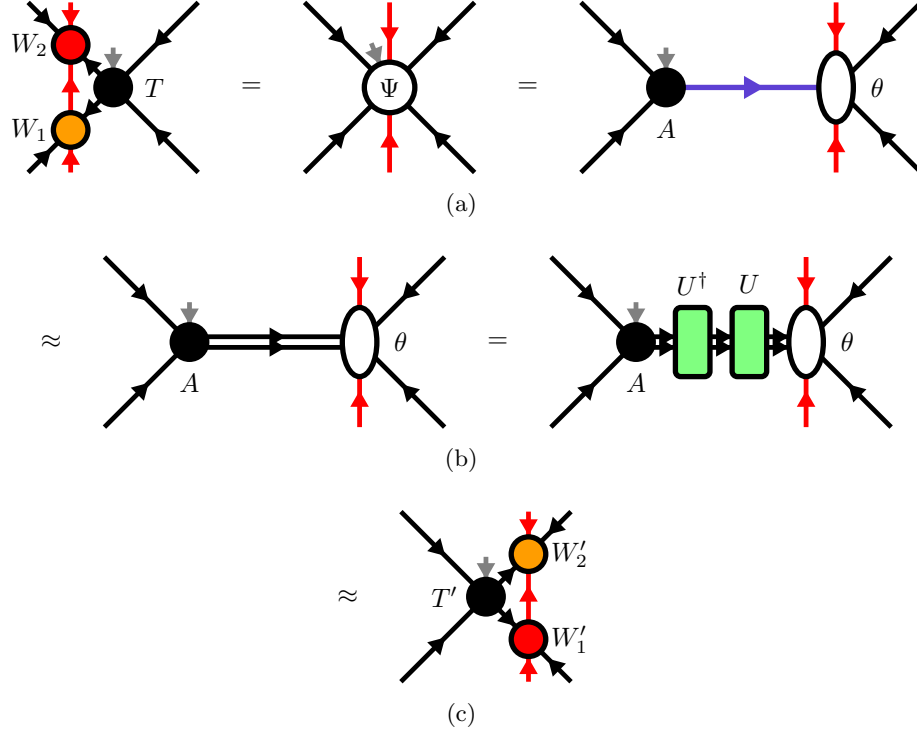


Figure 3.9: The YB move consists of three steps (a), (b) and (c) as explained in the text.

- Next, we split the index of the bond connecting A and θ into two indices of dimension D each, see Figure 3.9b. To proceed, we note that there exists a degree of freedom on the bonds connecting A and θ : A unitary U and its adjoint can be inserted as shown in the second step of Figure 3.9b without changing the result of the contraction

$$AU^\dagger U\theta = (AU^\dagger)(U\theta) =: T'\tilde{\theta}.$$

The unitary U can be chosen to minimize the truncation error of the next step by *disentangling* the tensor θ . We will discuss procedures of finding such a *disentangling unitary* U on the next page.

- In the last step, the tensor $\tilde{\theta}$ is split vertically into W'_1 and W'_2 using a truncated SVD as shown in Figure 3.9c. The computational cost of this SVD scales as $\mathcal{O}(\chi^3 D^6) = \mathcal{O}(D^9)$. Here, the bond dimension is truncated to χ . We end up with the three tensors T' , W'_1 and W'_2 , completing the YB move.

Before we discuss the disentangling procedure, two comments about step 2 of the above algorithm are in order. First, there exists a degree of freedom for splitting the

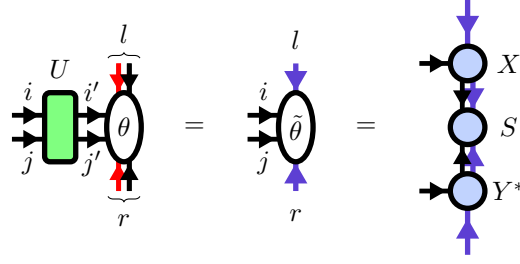


Figure 3.10: The disentangling unitary U is contracted with the wave function tensor θ to form $\tilde{\theta}$, which is subsequently split via an SVD $\tilde{\theta} = XSY^\dagger$. The purple legs have bond dimension χD .

bond index, because applying the same permutations to the columns of A and rows of θ does not change the result of contracting the network. However, this degree of freedom is fixed by the disentangling process, making the exact permutation of the bond splitting irrelevant. Second, note that near the edges of the lattice it can happen that the matrixized tensor Ψ has $\tilde{\chi} < D^2$ rows. In this case, the bond dimension after the SVD will also be $\tilde{\chi}$ and we cannot simply split the bond into two bonds of dimension $\chi_1 = \chi_2 = D$. Instead, we choose a splitting $\chi_1 \leq D$, $\chi_2 \leq D$ such that $\chi_1 \cdot \chi_2$ is maximized, while it must still hold $\chi_1 \cdot \chi_2 \leq \tilde{\chi}$. We additionally prefer equal splittings $\chi_1 \approx \chi_2 \approx \sqrt{\tilde{\chi}}$ if possible. One can find such a splitting easily by computing all possible combinations of χ_1 and χ_2 and keeping only the best one, which has a computational cost of $\mathcal{O}(\sqrt{\tilde{\chi}}) = \mathcal{O}(D)$. See also our implementation at [36].

The Disentangling Process

We will now discuss the problem of finding a good disentangling unitary U for step 2 of the above algorithm, which is crucial for the performance of the YB move. The problem can be formulated as follows: Given the tensor θ that is obtained after splitting the index in step 2, find a unitary U minimizing a cost function $f(U, \theta)$. In the following, let $\tilde{\theta}_{(l,i),(j,r)}$ be the $\chi D^2 \times \chi D^2$ matrix that is obtained by reshaping the contraction $\tilde{\theta}_{l,i,j,r} = \sum_{i',j'} U_{i,j,i',j'} \theta_{l,i',j',r}$ into a matrix as shown in Figure 3.10. Let further $\tilde{\theta} = XSY^\dagger$ denote the SVD of $\tilde{\theta}$. We discuss two cost functions, as also done in [26]. The first cost function is simply given by the truncation error

$$f_{\text{trunc}}(U, \theta) = \sqrt{\sum_{\mu=\chi+1}^{\chi D^2} S_\mu^2} \quad (3.4)$$

arising in step 3 of the YB move. Alternatively, one can think of $|\tilde{\theta}\rangle := \sum_{(l,i),(j,r)} \tilde{\theta}_{(l,i),(j,r)} |(l,i), (j,r)\rangle$ as a bipartite state in an orthogonal basis and consider

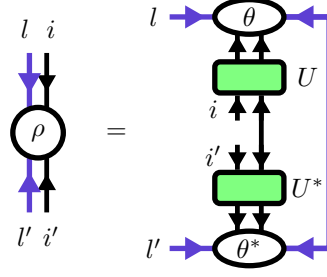


Figure 3.11: Definition of the reduced density matrix ρ . The purple legs have bond dimension χD .

as a cost function the Rényi-entropy

$$f_{\text{Rényi}}(U, \theta, \alpha) = \frac{1}{1 - \alpha} \log \text{Tr}(\rho^\alpha) = \frac{1}{1 - \alpha} \log \left(\sum_{\mu=1}^{\chi D^2} S_\mu^{2\alpha} \right), \quad (3.5)$$

where $\alpha \in [0, \infty)$ and $\rho = \text{Tr}_{(j,r)}(|\tilde{\theta}\rangle\langle\tilde{\theta}|)$ is the reduced density matrix obtained by tracing out one of the subsystems, see Figure 3.11. In the last step of (3.5), we used the fact that the eigenvalues of ρ are the squares of the singular values of $\tilde{\theta}$. The Rényi-entropy can be used as a measure of entanglement. It approaches the Von-Neumann entanglement entropy for $\alpha \rightarrow 1$. It can be shown that the truncation error is bounded by the Rényi-entropy if $\alpha < 1$ [17], which is a motivation for using $f_{\text{Rényi}}$ as a cost function. For $\alpha > 1$ such a bond cannot generally be given. However, optimizations of Rényi-entropies with $\alpha > 1$ are often simpler to perform and still achieve good results in practice [23, 26, 47]. Setting $\alpha = 2$ yields the Rényi-entropy

$$f_{\text{Rényi}}(U, \theta, \alpha = 2) = -\log \text{Tr} \rho^2, \quad (3.6)$$

which can easily be computed by contracting the tensor network shown in Figure 3.12a without needing to perform an SVD [47]. The cost function $f_{\text{Rényi}}(U, \theta, \alpha = 2)$ can be minimized using the Evenly-Vidal algorithm as proposed in [47]. First, we rewrite the minimization problem as a maximization problem

$$U_{\text{opt}} = \underset{U^\dagger U = \mathbb{1}}{\text{argmin}} f_{\text{Rényi}}(U, \theta, \alpha = 2) = \underset{U^\dagger U = \mathbb{1}}{\text{argmax}} \text{Tr} \rho^2.$$

We proceed by taking one tensor U out of the network $\text{Tr} \rho^2$ and contracting all other tensors into the environment E as shown in Figure 3.12b. We now treat E as if it were independent of U and update $U \leftarrow AB^\dagger$, where A and B are obtained by taking the SVD $E = A\Lambda B^\dagger$. This is repeated until convergence. For details on the Evenly-Vidal algorithm see Appendix A.2. In practice it is observed that

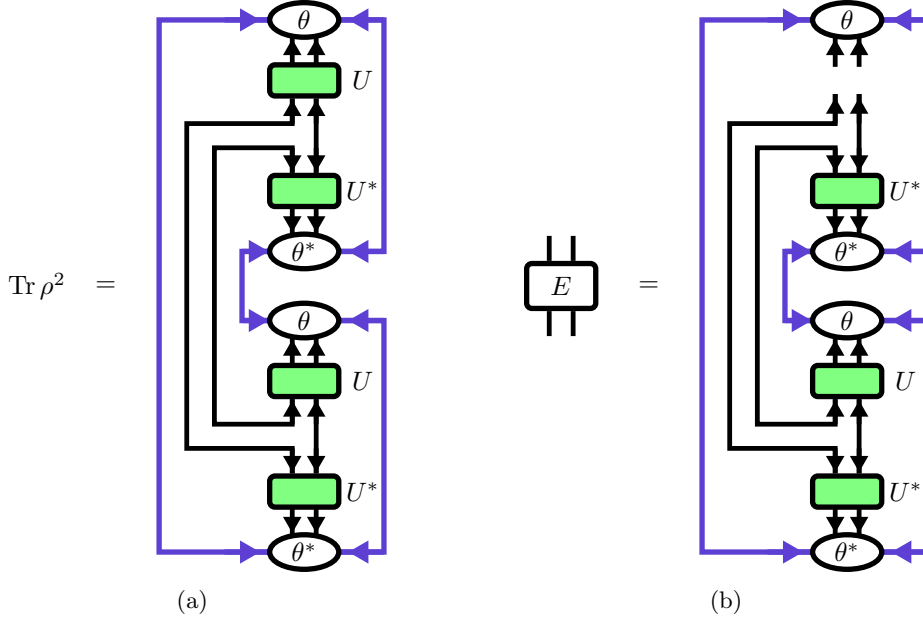


Figure 3.12: (a) Tensor network for the computation of the cost function (3.6). (b) Taking out one unitary U , the tensor network is contracted into the environment E .

this algorithm for minimizing $f_{\text{Rényi}}(U, \theta, \alpha = 2)$ converges very quickly [26]. The computational cost of this algorithm is dominated by the contraction of the effective environment E , which scales as $\mathcal{O}(\chi^3 D^6) = \mathcal{O}(D^9)$. The full cost of the algorithm is thus $\mathcal{O}(N_{\text{iter}} D^9)$, with N_{iter} the number of disentangling iterations.

Minimizing the truncation error $f_{\text{trunc}}(U, \theta)$ and general Rényi-entropies $f_{\text{Rényi}}(U, \theta, \alpha \neq 2)$ is a harder problem. We follow the approach of [23, 26] and use Riemannian optimization [48–52] to solve the optimization problem. The idea of Riemannian optimization is to generalize common optimization algorithms that are defined in Euclidian vector spaces, such as Gradient Descent or Conjugate Gradients, to Riemannian manifolds. The set of all isometric matrices of shape $n \times m$ is a Riemannian manifold called the Stiefel manifold $\text{St}(n, p)$. A special case is the set of all unitary matrices of shape $n \times n$, $U(n) = \text{St}(n, n)$, over which we want to optimize here. Riemannian optimization over the Stiefel manifold is discussed in more detail in Appendix B.

A typical optimization algorithm iteratively improves an iterate $U_k \in \text{St}(n, p)$, $k = 1, 2, \dots$ until a local minimum of the cost function f is found. In Riemannian optimization, the gradient of the cost function $\nabla f(U_k)$ is restricted to the tangent space $T_{U_k} \text{St}(n, p)$ of the iterate U_k [48], which we visualize in Figure 3.13. The gradient can be computed either analytically or via automatic differentiation [51, 52].

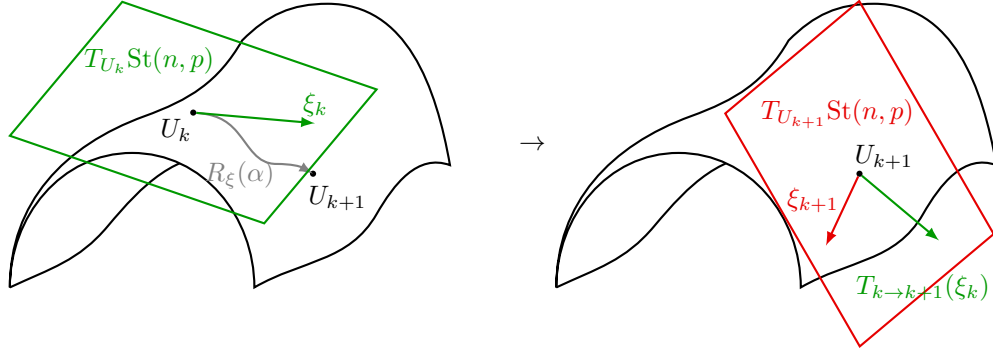


Figure 3.13: In this figure, a visualization of optimization on Riemannian manifolds is given. The iterate U_k (left) is updated along the search direction ξ_k , which is an element of the tangent space $T_{U_k} \text{St}(n, p)$. The next iterate U_{k+1} is computed with the retraction $R_\xi(\alpha)$, where $\alpha \in \mathbb{R}$ is the step size. For the computation of the next search direction ξ_{k+1} some algorithms need the previous search direction ξ_k , which must first be brought to the tangent space $T_{U_{k+1}} \text{St}(n, p)$ of the new iterate U_{k+1} via the vector transport $T_{k \rightarrow k+1}(\xi_k)$.

Optimization algorithms typically compute a search direction $\xi_k \in T_{U_k} \text{St}(n, p)$ and a step size $\alpha_k \in \mathbb{R}$ from the gradient. In an optimization algorithm defined on an Euclidean vector space one would then move along this direction as

$$\tilde{U}_{k+1} = U_k + \alpha_k \xi_k.$$

However, \tilde{U}_{k+1} is in general not an element of the manifold. To ensure $U_{k+1} \in \text{St}(n, p)$, one can introduce a *retraction* $R_{\xi_k} : \mathbb{R} \rightarrow \text{St}(n, p)$ [48]. One can think of $R_{\xi_k}(\alpha_k)$ as moving along the direction of ξ_k while staying on the manifold. As α_k increases, we move further along the path defined by the retraction, with $R_{\xi_k}(0) = U_k$, see Figure 3.13. Different retractions can be chosen, varying by how well they perform in optimization problems and by how hard they are to compute. Here we choose the retraction

$$R_{\xi_k}(\alpha_k) = \text{qf}(U_k + \alpha_k \xi_k),$$

where $\text{qf}(A)$ is the Q-factor of the QR-decomposition $A = QR$. This retraction is particularly easy to compute and yields good results in practice.

Many optimization algorithms such as Conjugate Gradients require gradients or search directions from previous iterates for computing a search direction at the current iterate. In Riemannian optimization, one must first bring these gradients and search directions from the tangent spaces of previous iterates to the tangent space of the current iterate. This is handled by a so-called *vector transport* $T_{k \rightarrow k+1}(\xi_k)$ [48], see Figure 3.13.

Finally, for optimization algorithms of second order such as the trust-region method, one needs to generalize the notion of the Hessian-vector product to Riemannian

manifolds. This generalization is given by the *Riemannian connection* [48]. For the Stiefel manifold the Hessian-vector product is simply given by projecting the Hessian-vector product of the embedding euclidean vector space $\mathbb{C}^{n \times p}$ to the tangent space.

We use two algorithms for solving the disentangling optimization problem, Conjugate Gradients (CG) and the Trust-Region Method (TRM). CG uses the accumulated gradients of previous iterations to compute an improved search direction, trying to achieve superlinear convergence. CG is discussed in more details in Appendix B.3. The TRM approximates the cost function around the current iterate through a quadratic function using the Hessian-vector product. This approximate cost function is then minimized within a region of radius $\Delta \in \mathbb{R}$ using truncated Conjugate Gradients (tCG), which converges quickly for the quadratic approximation. Depending on the quality of the approximation at the current iterate one can then shrink or enlarge the trust region. TRM is able to achieve local superlinear convergence while still retaining desired global convergence properties [48] and can be thought of as an improved version of Newton's method. For more details, see Appendix B.4.

The gradients and Hessian-vector products of the cost functions (3.4) and (3.5) can be computed analytically with a computational cost of $\mathcal{O}(D^9)$, see Appendix C for a derivation.

Approximate Gradients and Hessian-Vector Products

The cost of both CG and the TRM are dominated by the computation of the gradient and Hessian-vector product, particularly by the SVD $\tilde{\theta} = XSY^\dagger$ and contractions involving the tensors X and Y . The reason for this is the large bond dimension χD^2 of the bond connecting X and Y , see Figure 3.10. We thus propose to approximate the gradient and Hessian-vector product by instead performing an approximate SVD $\tilde{\theta} \approx \tilde{X}\tilde{S}\tilde{Y}^\dagger$, where we only keep χ of the χD^2 singular values. The algorithm for performing this approximate SVD is inspired by [53], where a similar algorithm was used to speed up TEBD updates for MPS. We sketch the algorithm in Figure 3.14. First, an approximate QR-decomposition $\tilde{\theta} = QR$ with $Q \in \mathbb{C}^{\chi D^2 \times \chi}$ and $R \in \mathbb{C}^{\chi \times \chi D^2}$ is performed by variationally minimizing the distance $\|\tilde{\theta} - QR\|$, which is equivalent to maximizing the real part of the overlap $\text{Re}\langle \tilde{\theta}, QR \rangle_F$. The overlap is shown as a tensor diagram in Figure 3.14a. It can be maximized by alternately optimizing the tensors Q and R as shown in Figures 3.14b and 3.14c respectively, which costs $\mathcal{O}(\chi^3 D^4) = \mathcal{O}(D^7)$ per iteration. A standard SVD is then performed on the R -factor of the approximate QR-decomposition as $R = A\tilde{S}\tilde{Y}^\dagger$, and the contraction $\tilde{X} = QA$ finalizes the decomposition, see Figure 3.14d. In total, the cost of the approximate SVD is $\mathcal{O}(N_{\text{svd}} D^7)$, with N_{svd} the number of iterations, instead of $\mathcal{O}(D^9)$ for a full SVD. It is observed that the variational minimization that is used to compute the approximate SVD converges very quickly in practice, especially if a good initialization

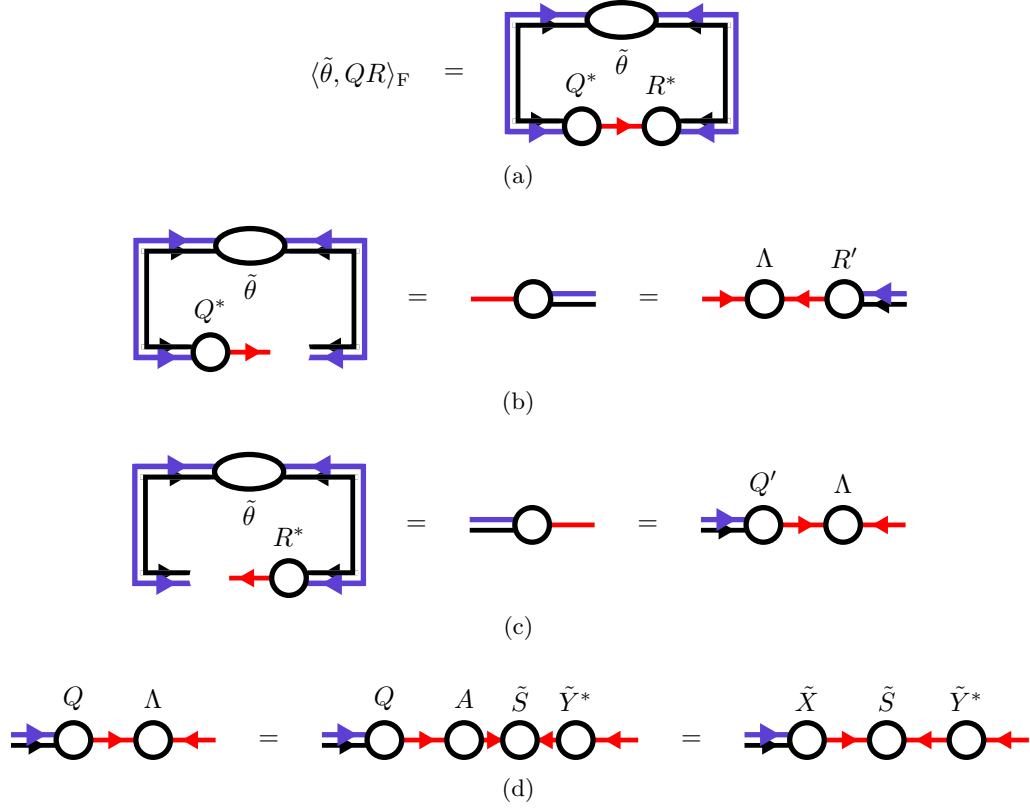


Figure 3.14: In this figure we draw tensor diagrams for the approximate SVD. First, an approximate QR-decomposition is performed by minimizing the inner product $\langle \tilde{\theta}, QR \rangle_F$ (a). This can be done by iteratively updating the R -tensor (b) and the Q -tensor (c). We finish the approximate SVD by performing a standard SVD on the tensor Λ , which has reduced bond dimension (d).

is chosen. As the iterates U_k are expected to only change slightly in each iteration of CG or TRM, one can simply use the result Q, R obtained in the approximate QR-decomposition of the previous iteration as initialization for the next iteration. We observe that the variational optimization in practice converges in less than 5 iterations.

Using the approximate SVD, we were able to decrease the cost of the gradient computation from $\mathcal{O}(D^9)$ to $\mathcal{O}(D^8 + N_{\text{svd}} D^7)$. Moreover, through caching of the most costly contraction, the cost of the tCG sub-procedure that is called in every iteration of the TRM can be brought down from $\mathcal{O}(N_{\text{tCG}} D^9)$ to $\mathcal{O}(D^8 + N_{\text{svd}} D^7 + N_{\text{tCG}} D^7)$, where N_{tCG} is the maximum number of iterations for which the tCG sub-procedure is run. Finally, one can also use an approximate SVD for the final vertical splitting performed in step 3 of the YB move after the disentangling is complete, improving

Evenbly-Vidal style iterative optimization	$\mathcal{O}(N_{\text{iter}}D^8)$
SVD splitting	$\mathcal{O}(D^9)$
approximate SVD splitting	$\mathcal{O}(D^8 + N_{\text{svd}}D^7)$
Evenbly-Vidal Rényi-2 disentangler	$\mathcal{O}(N_{\text{iter}}D^9)$
CG disentangler	$\mathcal{O}(N_{\text{iter}}D^9)$
TRM disentangler	$\mathcal{O}(N_{\text{iter}}N_{\text{tCG}}D^9)$
approximate CG disentangler	$\mathcal{O}(N_{\text{iter}}(D^8 + N_{\text{svd}}D^7))$
approximate TRM disentangler	$\mathcal{O}(N_{\text{iter}}(D^8 + N_{\text{svd}}D^7 + N_{\text{tCG}}D^7))$

Table 3.1: In this table we summarize the complexity scaling of the different discussed algorithms for performing the YB move. The scaling of the Rényi-entropy and truncation error disentangling is the same, but with different prefactors.

the scaling from $\mathcal{O}(D^9)$ to $\mathcal{O}(N_{\text{svd}}D^7)$. To summarize, we list the computational complexity of all discussed algorithms for the YB move in Table 3.1.

Comparison of Different Disentanglers

We will now compare the different algorithms for solving the disentangling problem.

For this comparison we select the YB move environment $\{W_1, W_2, T\}$ that was already used to discuss the convergence behaviour of the iterative algorithm in Section 3.2.1. The results on other YB environments agree qualitatively with the results we present here. The bond dimensions chosen for the YB-isoTPS are $D = 4$, $\chi = 24$.

We first test the Evenbly-Vidal algorithm optimizing the Rényi-entropy with $\alpha = 2$, see Figure 3.15. The algorithm converges very quickly after only ≈ 20 iterations. The convergence speed depends drastically on the initialization of the disentangling unitary. We find that a initialization based on an SVD of θ works best, see our implementation [36]. This initialization procedure was introduced for the MM for isoTPS [23, 26].

Next, we look at the performance of CG and TRM optimizing the Rényi-entropy with $\alpha = 1/2$ and the truncation error in Figures 3.16a and 3.16c respectively. In both cases we observe that the TRM leads to a faster decrease in the cost function for the same number of iterations compared to CG. Remarkably, the approximate versions of both CG and TRM perform almost as good as their exact counterparts. Again, the speed of convergence depends strongly on the initialization. Because of the quick convergence of the Evenbly-Vidal algorithm optimizing the $\alpha = 2$ Rényi-entropy, we choose its result as an initialization for the optimization algorithms using Riemannian optimization. This achieved the best results in our testing.

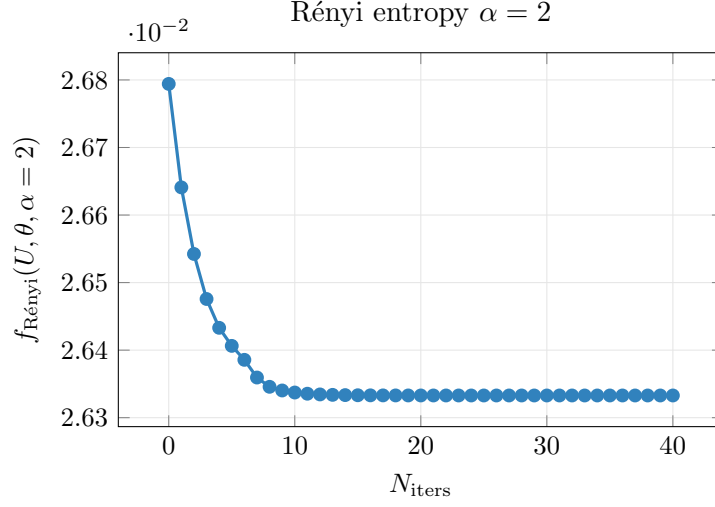


Figure 3.15: We plot the Rényi-2 entropy against the number of iterations N_{iter} of the Evenbly-Vidal disentangling algorithm. The environment of tensors on which the disentangling is performed is the same as in Figure 3.8. The Evenbly-Vidal disentangling algorithm converges quickly after only $N_{\text{iter}} \approx 20$ iterations.

Last, we plot the cost function against the walltime of the Riemannian disentangling algorithms in Figures 3.16b and 3.16d. For this benchmark, the algorithms were run on an i5-12500 CPU with 6 cores. As one can see, the approximate versions of both CG and TRM run up to an order of magnitude faster while still providing a comparable minimization of the cost function. Thus, in practice, it is often better to choose a larger maximum bond dimension with the approximate disentangling algorithms instead of a smaller maximum bond dimension with the exact algorithms.

3.2.3 Comparison of the Algorithms

In the following, we qualitatively compare the two discussed algorithms for the YB move. We again select the YB move environment $\{W_1, W_2, T\}$ that we used for discussing the individual convergence of the iterative YB move in Section 3.2.1 and the disentanglers in Section 3.2.2. We compare five algorithms for performing the YB move: A simple SVD splitting without a disentangling algorithm, using a naive guess for the disentangling unitary that is computed by performing an SVD as in [23, 26] (**SVD + init**), The iterative Evenbly-Vidal-style optimization of the truncation error (**EV trunc**) from Section 3.2.1, the Evenbly-Vidal-style disentangler minimizing the Rényi-2-entropy (**EV Rényi-2.0**), and the approximate TRM minimizing the truncation error (**approx TRM trunc**) and the Rényi-0.5-entropy (**approx TRM Rényi-0.5**). We plot the error of the YB move $\|\Psi - \Psi'\|$

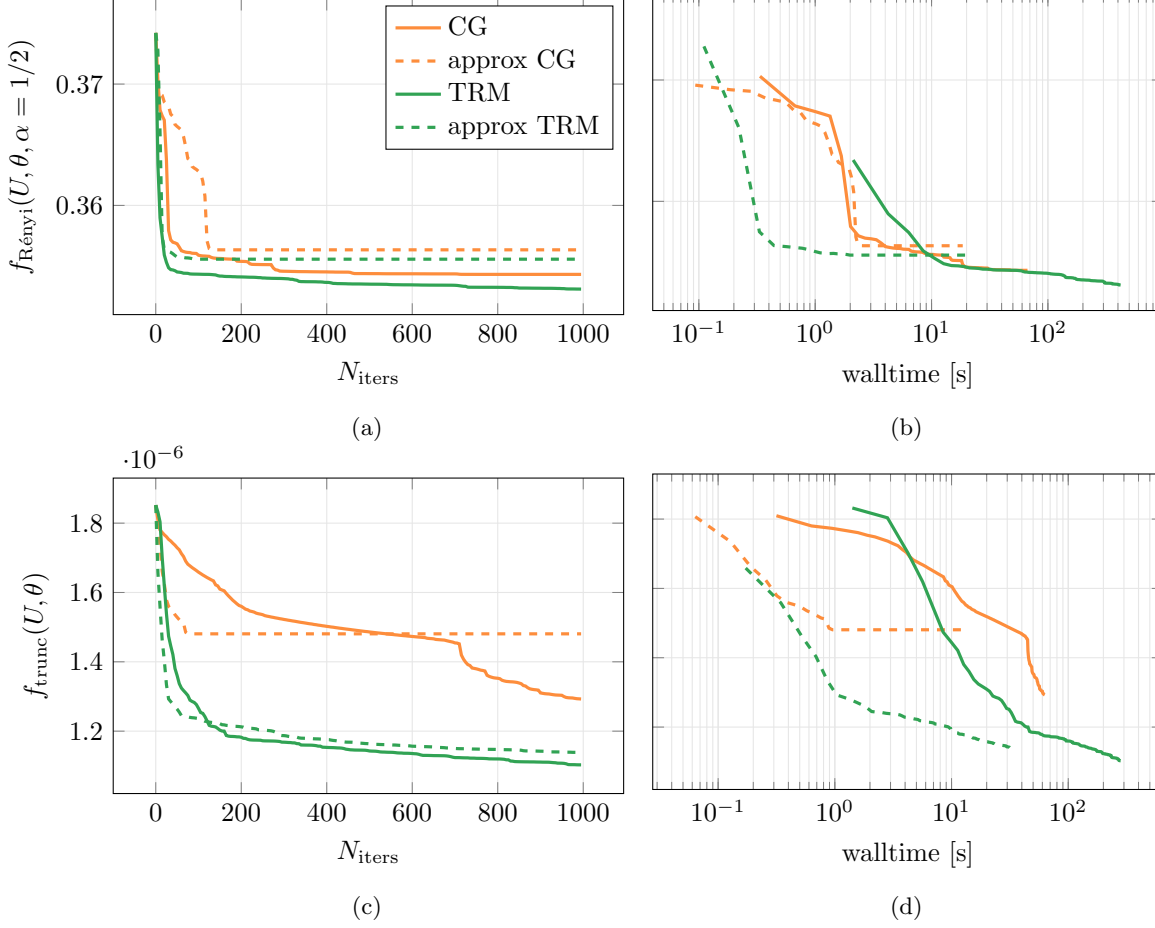


Figure 3.16: In this figure we qualitatively compare the different disentanglers that use Riemannian optimization to minimize the cost function. (a) (c) The $\alpha = 0.5$ Rényi-entropy and the truncation error are plotted against the number of disentangling iterations. The approximate versions of the CG and TRM algorithms perform almost as good as the exact versions. (b) (d) We now plot the Rényi-entropy and the truncation error against the walltime of the algorithms, showing the improved speed of the approximate algorithms. The environment of tensors used for the YB move is the same as in Figures 3.8 and 3.15.

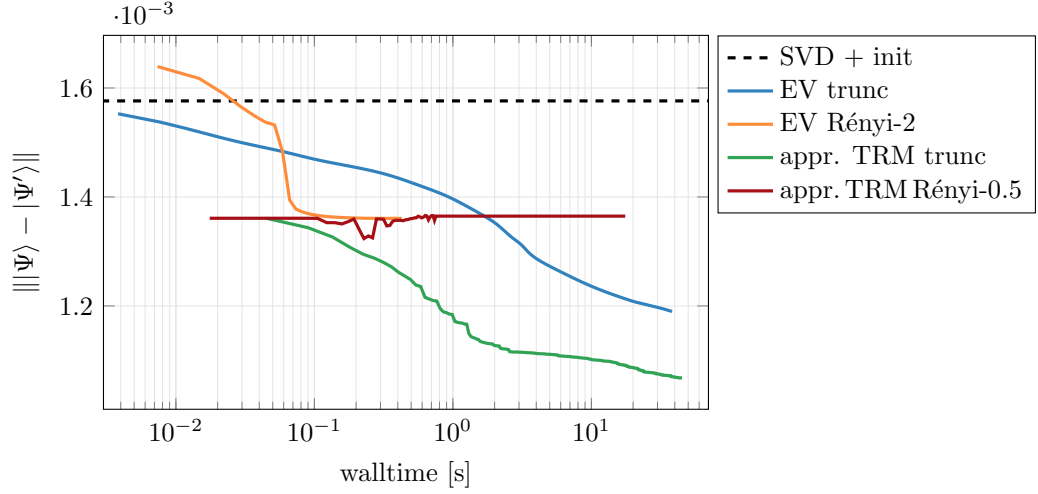


Figure 3.17: In this figure we qualitatively compare different algorithms for performing the YB move. We plot the error of the YB move against the walltime of the algorithms.

against the walltime in seconds in Figure 3.17. Note that this is only a qualitative comparison, since the environment was selected arbitrarily. For a more quantitative comparison, see Chapter 5. We observe that the algorithms that directly minimize the truncation error also are able to achieve a lower YB error than the algorithms minimizing the Rényi-entropy. However, as we will see in Chapter 5, minimizing the Rényi-entropy actually leads to a lower global error when performing a full shifting of the orthogonality hypersurface. We further observe the slow convergence of the iterative Evenbly-Vidal style algorithm, suggesting that the disentangling algorithm with Riemannian optimization of the truncation error will provide better results. Even though the computational complexity of **EV Rényi-2.0** scales as $\mathcal{O}(D^9)$, its quick convergence behaviour makes it faster than all other algorithms. Because of this, we use the algorithm as initialization for the disentanglers using Riemannian optimization. Note that in principle the approximate SVD discussed in Section 3.2.2 could be used to decrease the computational cost of **EV Rényi-2.0** to $\mathcal{O}(N_{\text{iter}}(D^8 + N_{\text{svd}}D^7))$, which was not necessary for the bond dimensions we used.

3.3 Time Evolving Block Decimation (TEBD)

We will now discuss the Time Evolving Block Decimation (TEBD) algorithm for YB-isoTPS, which can be used for both real and imaginary time evolution. The algorithm is a generalization of TEBD for MPS, which we discussed in Section 2.4. Analogously to MPS we start with a Suzuki-Trotter decomposition, approximating the

time evolution operator $\hat{U}(\Delta t) = e^{-i\Delta t \hat{H}}$ by a product of bond operators $\hat{U}^{[i,j]}(\Delta t)$ acting only on neighboring sites i and j of the bond $[i, j]$. These bond operators then must be applied to the state in the correct order, while keeping the YB-isoTPS structure intact. We will discuss the process of applying a single bond operator $\hat{U}^{[i,j]}(\Delta t)$ to the YB-isoTPS in Section 3.3.1. In Section 3.3.2 we then discuss the full TEBD algorithm.

3.3.1 Local TEBD Updates

Let us assume that the orthogonality center is positioned between the two sites on which the bond operator $\hat{U}^{[i,j]}(\Delta t)$ acts. The five tensors around the orthogonality center then make up a sub-network with only incoming arrows, compare Figure 3.3a. We call these five tensors T_i , T_j , W_1 , W_2 and W_3 . The local TEBD update can then be formulated as the following problem: Find tensors T'_i , T'_j , W'_1 , W'_2 and W'_3 satisfying the isometry constraints and minimizing the error

$$\varepsilon_{\text{trunc}} = \left\| \hat{U}^{[i,j]}(\Delta t) |\Psi\rangle - |\Psi'\rangle \right\|,$$

where $|\Psi\rangle = |\Psi(T_i, T_j, W_1, W_2, W_3)\rangle$ and $|\Psi'\rangle = |\Psi(T'_i, T'_j, W'_1, W'_2, W'_3)\rangle$. Similar to the YB-move, we can rewrite this as the problem of maximizing the overlap

$$(T'_{i,\text{opt}}, T'_{j,\text{opt}}, W'_{1,\text{opt}}, W'_{2,\text{opt}}, W'_{3,\text{opt}}) = \underset{T'_i, T'_j, W'_1, W'_2, W'_3}{\text{argmax}} \quad \text{Re} \langle \Psi' | \hat{U}^{[i,j]}(\Delta t) | \Psi \rangle \quad (3.7)$$

under the constraints $T_i^\dagger T'_i = \mathbb{1}$, $T_j^\dagger T'_j = \mathbb{1}$, $W_1^\dagger W'_1 = \mathbb{1}$, $W_3^\dagger W'_3 = \mathbb{1}$ and $\|W'_2\| = 1$. Using the isometry condition, the overlap $\langle \Psi' | \hat{U}^{[i,j]}(\Delta t) | \Psi \rangle$ can be computed by contracting the tensor network drawn in Figure 3.18.

For solving this problem we again use the Evenbly-Vidal algorithm. Similar to the iterative Evenbly-Vidal style algorithm for the YB-move we discussed in Section 3.2.1, we optimize one tensor at a time while keeping all other tensors fixed. This procedure is then repeated, sweeping over all five tensors until convergence is achieved. For more details on this optimization method see Appendix A. Since the time step Δt is chosen to be small, the bond operator is close to identity, $\hat{U}^{[i,j]}(\Delta t) \approx \mathbb{1}$. Thus, a good initialization for the tensors of the updated wave function $|\Psi'\rangle$ are simply the tensors of the old wave function $|\Psi\rangle$.

The computational complexity of applying a local bond operator to a YB-isoTPS with the discussed algorithm scales as $\mathcal{O}(\chi^3 D^3 d^2) = \mathcal{O}(D^6)$. In practice it is observed that the algorithm converges after only a few iterations.

3.3.2 Global TEBD Updates

A global TEBD update evolves the state by a time Δt and can be performed by applying local TEBD updates on all bonds. For each local TEBD update, the

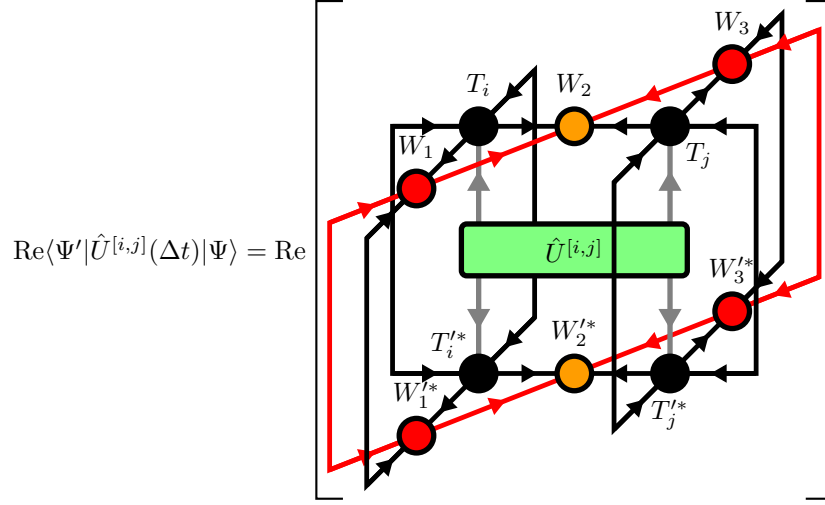


Figure 3.18: The cost function of the optimization problem (3.7) that must be solved for locally applying TEBD operators $\hat{U}^{[i,j]} := \hat{U}^{[i,j]}(\Delta t)$ can be computed as a contraction of the two-site wave functions of $|\Psi\rangle$ and $|\Psi'\rangle$, sandwiching the operator between the two.

orthogonality center must be moved to the bond at which the update is applied. Because moving the orthogonality hypersurface can only be done approximately, the number of necessary moves should be minimized.

As we have already done for MPS in Section 2.4, let us assume that the Hamiltonian \hat{H} can be written as a sum of nearest-neighbor operators. We index these nearest-neighbor operators $\hat{h}^{[x,y]}$ by two integers x and y corresponding to the position of the orthogonality hypersurface and orthogonality center if moved to the bond on which $\hat{h}^{[x,y]}$ acts. We define x to increase from left to right and y to increase from bottom to top, as shown in Figure 3.19. The Hamiltonian can then be split into four parts by first grouping the $\hat{h}^{[x,y]}$ into two sets acting only on even and odd columns respectively and then splitting each set again into terms acting only on even/odd bonds along the respective columns. We can write this as

$$\begin{aligned} \hat{H} &= \sum_{x=1}^{2L_x-1} \sum_{y=1}^{2L_y-1} \hat{h}^{[x,y]} = \sum_{\substack{x \text{ even} \\ y \text{ even}}} \hat{h}^{[x,y]} + \sum_{\substack{x \text{ even} \\ y \text{ odd}}} \hat{h}^{[x,y]} + \sum_{\substack{x \text{ odd} \\ y \text{ even}}} \hat{h}^{[x,y]} + \sum_{\substack{x \text{ odd} \\ y \text{ odd}}} \hat{h}^{[x,y]} \\ &=: \hat{H}_1 + \hat{H}_2 + \hat{H}_3 + \hat{H}_4. \end{aligned}$$

The operators appearing in the sum in \hat{H}_j commute with each other and thus the exponential $e^{-i\Delta t \hat{H}_j}$ factorizes into a product of bond operators $\hat{U}^{[x,y]}(\Delta t) = e^{-i\Delta t \hat{h}^{[x,y]}}$.

We next use a Suzuki-Trotter decomposition to approximate the time evolution

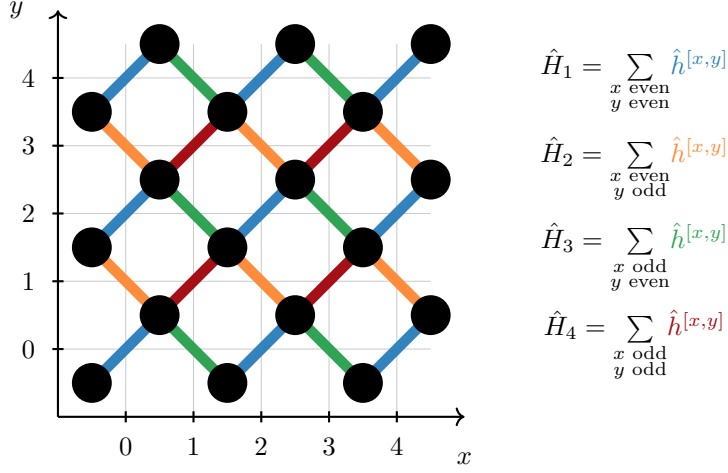


Figure 3.19: A Hamiltonian \hat{H} that is a sum of nearest-neighbor operators $\hat{h}^{[x,y]}$ can be split into four parts made up of operators acting only on even/odd columns and even/odd bonds along a column.

operator

$$\hat{U}(\Delta t) = \hat{U}^{\text{TEBD1}}(\Delta t) + \mathcal{O}(\Delta t^2)$$

with

$$\hat{U}^{\text{TEBD1}}(\Delta t) := e^{-i\Delta t \hat{H}_4} e^{-i\Delta t \hat{H}_3} e^{-i\Delta t \hat{H}_2} e^{-i\Delta t \hat{H}_1}.$$

To evolve the state $|\Psi\rangle$ in time with this first order approximation, we must compute $|\Psi'\rangle \approx \hat{U}^{\text{TEBD1}}(\Delta t) |\Psi\rangle$ as a YB-isoTPS. The procedure is sketched in Figure 3.20a. We start in the left-most column and apply all bond operators that act on bonds along this column. The bond operators on the column are applied in a brick-wall fashion analogously to the MPS algorithm: First all even bonds are updated and then all odd bonds are updated. Local updates are computed using the algorithm discussed in Section 3.3.1. Next, we move the orthogonality hypersurface two columns to the right and again apply all bond operators along the column. We proceed until all bond operators on even columns have been applied, in which case the orthogonality hypersurface is now positioned at its right-most position. We now sweep back to the left, applying all bond operators acting on odd columns along the way. Arriving back at the left-most column, all bonds making up $\hat{U}^{\text{TEBD1}}(\Delta t)$ have been applied in the correct order and the state has been evolved by time Δt .

We can obtain a better approximation of the time evolution operator $\hat{U}(\Delta t)$ by performing a second order Suzuki-Trotter decomposition. By repeatedly applying the symmetrized decomposition

$$e^{-i\varepsilon(\hat{A}+\hat{B})} = e^{-i\frac{\varepsilon}{2}\hat{A}} e^{-i\varepsilon\hat{B}} e^{-i\frac{\varepsilon}{2}\hat{A}} + \mathcal{O}(\Delta t^3)$$

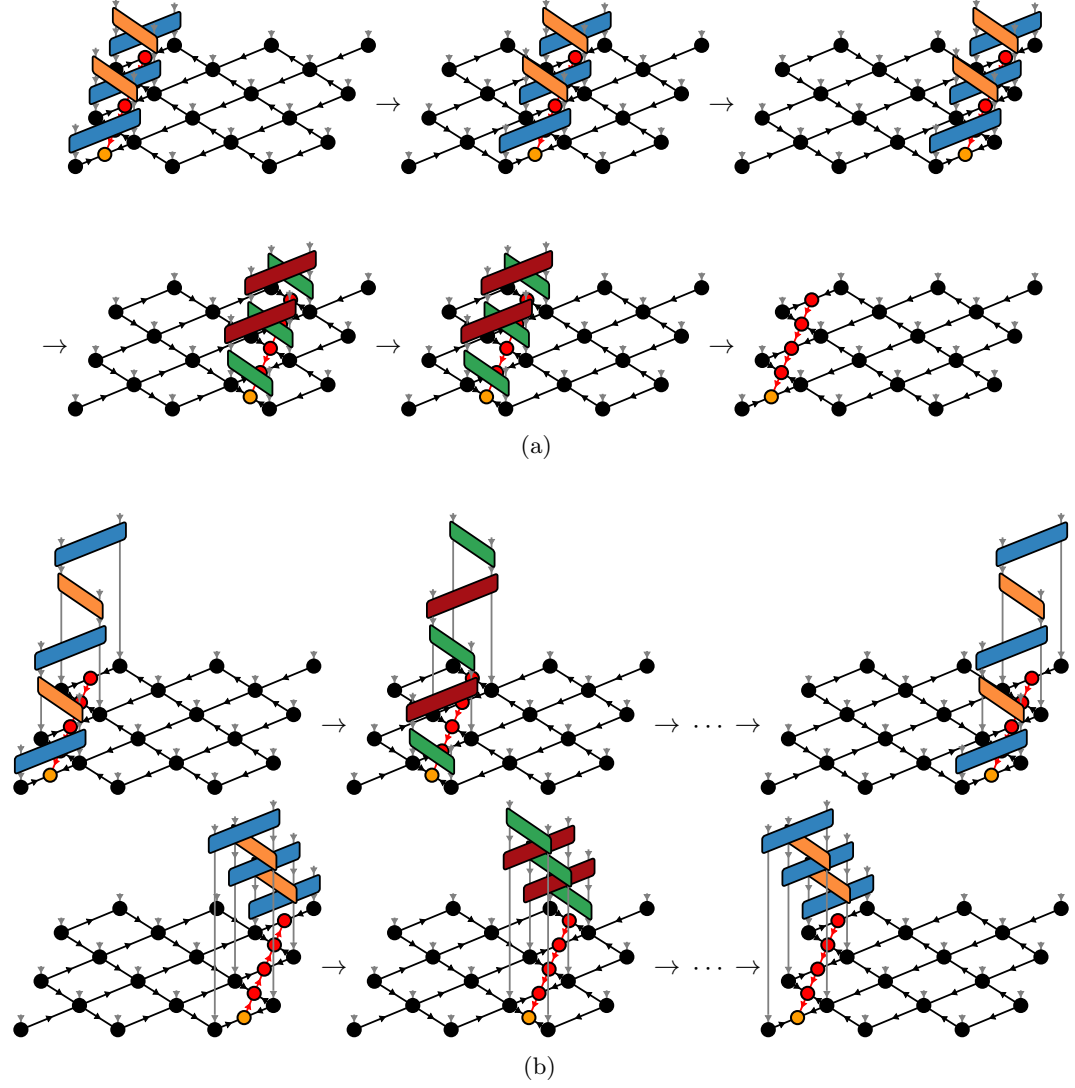


Figure 3.20: To apply a TEBD update, we sweep across the YB-isoTPS once from left to right and back from right to left. (a) TEBD1 applies the operators in a brick-wall fashion, while (b) TEBD2 applies the operators along a chain.

we obtain

$$\begin{aligned}
e^{-i\Delta t \hat{H}} &= \exp \left(-i\Delta t \sum_{x,y} \hat{h}^{[x,y]} \right) \\
&= e^{-i\frac{\Delta t}{2} \hat{h}^{[1,1]}} e^{-i\Delta t (\hat{H} - \hat{h}^{[1,1]})} e^{-i\frac{\Delta t}{2} \hat{h}^{[1,1]}} + \mathcal{O}(\Delta t^3) \\
&= e^{-i\frac{\Delta t}{2} \hat{h}^{[1,1]}} e^{-i\frac{\Delta t}{2} \hat{h}^{[1,2]}} e^{-i\Delta t (\hat{H} - \hat{h}^{[1,1]} - \hat{h}^{[1,2]})} e^{-i\frac{\Delta t}{2} \hat{h}^{[1,2]}} e^{-i\frac{\Delta t}{2} \hat{h}^{[1,1]}} + \mathcal{O}(\Delta t^3) \\
&= \dots \\
&= e^{-i\frac{\Delta t}{2} \hat{h}^{[1,1]}} e^{-i\frac{\Delta t}{2} \hat{h}^{[1,2]}} \dots e^{-i\frac{\Delta t}{2} \hat{h}^{[1,2]}} e^{-i\frac{\Delta t}{2} \hat{h}^{[1,1]}} + \mathcal{O}(\Delta t^3).
\end{aligned}$$

Here, in each step we "split off" one operator $\hat{h}^{[x,y]}$ from the sum. The final result is a product of bond operators $\hat{U}^{[x,y]}(\Delta t/2)$ that must be applied from right to left. The algorithm of applying a global second order update is thus similar to a TEBD update of first order. We sweep across the YB-isoTPS once from left to right and back, applying bond operators along the way in the correct order, as visualized in Figure 3.20b. The difference is that now the operators are applied in a chain-like order instead of the brick wall order of TEBD1. The number of YB moves for TEBD1 and TEBD2 is the same, but the smaller Trotter error of $\mathcal{O}(\Delta t^3)$ instead of $\mathcal{O}(\Delta t^2)$ allows us to use larger time steps for TEBD2, resulting in a smaller number of YB moves per unit time. We find that the YB move is the primary source of error in practice and thus expect TEBD2 to perform much better than TEBD1.

In principle, one could also go to higher decomposition orders [41]. However, already a third order decomposition would necessitate a larger number of sweeps for applying the full update, increasing the error accumulated through YB moves. It is therefore not clear if higher order decompositions would be able to improve the method further.

Chapter 4

The Toric Code: An Exactly Representable Model

In this chapter, we show that the YB-isoTPS ansatz introduced in Chapter 3 is able to exactly represent the ground state of the Toric Code Model, as was also shown for MM-isoTPS [27]. We first give a brief introduction to the Toric Code model in Section 4.1 and show how the ground state can be derived analytically. We then discuss how this ground state can be represented as a YB-isoTPS in Section 4.2, following [27].

4.1 The Toric Code Model

The Toric Code is an exactly soluble spin model with \mathbb{Z}_2 topological order that was introduced by Alexei Kitaev [54]. The model is defined on the square lattice with periodic boundary conditions, where on each edge of the lattice there sits a spin-1/2 degree of freedom. Two operators are introduced, the *star operators*

$$\hat{A}_+ := \sum_{j \in +} \hat{\sigma}_j^z \quad (4.1)$$

and the *plaquette operators*

$$\hat{B}_\square := \sum_{j \in \square} \hat{\sigma}_j^x, \quad (4.2)$$

where the sums are performed over the four spins connected in a star or plaquette pattern respectively (see Figure 4.1) and $\hat{\sigma}_j^x, \hat{\sigma}_j^z$ are Pauli matrices. The Hamiltonian of the Toric Code model is then defined as

$$H_{\text{TC}} := - \sum_+ \hat{A}_+ - \sum_\square \hat{B}_\square, \quad (4.3)$$

where the sums go over all possible stars and plaquettes respectively. Because an arbitrary star and plaquette operator share either two or zero spins, all terms of the Hamiltonian commute and it is thus possible to find the ground state of the model

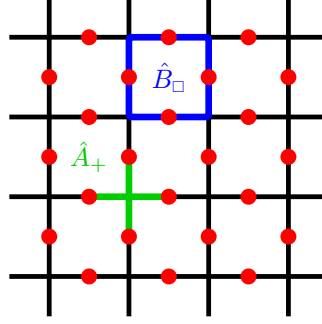


Figure 4.1: The Toric Code model is defined on the square lattice with spin-1/2 degrees of freedom living on the edges. the star and plaquette operators (4.1) and (4.2) act on the four spins arranged in a star or plaquette shape respectively.

by diagonalizing all terms simultaneously. To diagonalize the star operators \hat{A}_+ we choose a basis of $\hat{\sigma}_z$ -eigenstates $|i\rangle \in \{|\uparrow\rangle, |\downarrow\rangle\}$ with eigenvalues $\langle \hat{\sigma}_z \rangle_i = s_i = \pm 1$ for each spin i . In this basis every star operator is diagonal with eigenvalues

$$\langle \hat{A}_+ \rangle = \prod_{j \in +} s_j = \pm 1$$

To obtain the expectation value $\langle \hat{A}_+ \rangle = 1$, the number of spins in the down state $s_j = -1$ around the vertex $+$ must be even. Basis states $|s\rangle$ that give an expectation value of 1 for every star operator simultaneously are thus the states with an even number of down-spins around every vertex,

$$|s\rangle = |s_1\rangle \otimes \cdots \otimes |s_N\rangle, \quad \prod_{j \in +} s_j = 1 \quad \forall +. \quad (4.4)$$

The plaquette operator \hat{B}_\square acts on such a state $|s\rangle$ state by flipping all spins around the plaquette \square . Because a plaquette and a star share either zero or two spins, applying an plaquette operator to a state $|s\rangle$ satisfying condition (4.4) produces a state $|s'\rangle$ that again satisfies (4.4), and applying the same plaquette operator a second time produces the initial state $|s\rangle$. If we now take the equal weighted superposition $|\Psi\rangle = (|s\rangle + |s'\rangle) / \sqrt{2}$, the expectation value of \hat{B}_\square becomes $\langle \hat{B}_\square \rangle = 1$. The ground state of the Hamiltonian (4.3) is thus given by the equal weighted superposition of all basis states satisfying condition (4.4).

One can show that the ground state can be written as

$$|\Psi_0\rangle \propto \prod_{\square} \left(\mathbb{1} + \hat{B}_\square \right) |\uparrow\rangle \otimes \cdots \otimes |\uparrow\rangle.$$

Note that this is also the ground state for the model if open boundary conditions are chosen instead of periodic boundary conditions.

For periodic boundary conditions, which is equivalent to putting the model on a torus, one can further show that the ground state is fourfold topologically degenerate. To move from one degenerate section of the Hilbert space to another one must apply a string of operators, wrapping once around the torus. This is a highly non-local operation. Because perturbations are usually local, the toric code model can be interpreted as a form of hardware level error correction. The toric code is considered a topological quantum error correction code and can in theory be used for quantum memory. One can further implement quantum gates acting on the 4-dimensional ground state space by locally creating a pair of anyonic excitations, moving one of the excitations around the torus, and annihilating it with the other one [54]. Unfortunately, the gates that can be implemented as such do not form a complete gate set and thus do not allow for universal quantum computing. Nevertheless, the Toric code is an important model for the study of topological order and anyonic excitations.

4.2 Representing the Toric Code Ground State with YB-isoTPS

We will now derive the YB-isoTPS corresponding to the Toric Code ground state on a square lattice with open boundary condition. We choose rough boundary conditions [55], fixing all boundary spins to the state $(|\uparrow\rangle + |\downarrow\rangle)/\sqrt{2}$. As shown in [27], the Toric Code ground state can be represented exactly as a PEPS with bond dimension $D = 2$. One can construct such a PEPS by first doubling the Hilbert space on each edge as $|s_i\rangle \rightarrow |s_i\rangle \otimes |s_i\rangle$, which we show in Figure 4.2a. In the PEPS representation the physical degrees of freedom on each edge in the bulk are then carried by two identical tensors $\delta^B \in \mathbb{R}^{2 \times 2 \times 2}$,

$$\delta^B_{i,\alpha,\beta} = \begin{cases} 1 & \text{if } i = \alpha = \beta \\ 0 & \text{else} \end{cases},$$

as shown in Figure 4.2b. The boundary spins are represented by tensors $\delta^E \in \mathbb{R}^{2 \times 2}$,

$$\delta^E_{i,\alpha} = \begin{cases} 1 & \text{if } i = \alpha \\ 0 & \text{else} \end{cases}.$$

We proceed by associating each vertex with the spins on the four connected edges and contract the corresponding tensors δ^B and δ^E with a tensor $T \in \mathbb{R}^{2 \times 2 \times 2 \times 2}$ that is placed on each vertex,

$$T_{i,j,k,l} = \begin{cases} 1 & \text{if } (i + j + k + l) \bmod 2 = 0 \\ 0 & \text{else} \end{cases}.$$

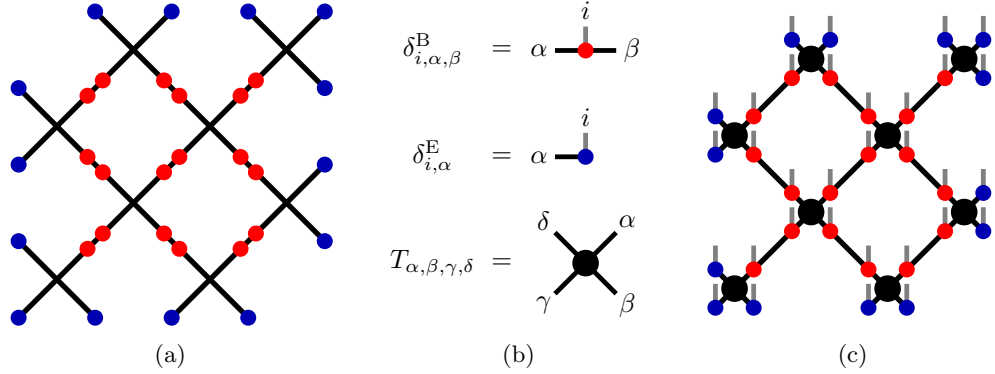


Figure 4.2: (a) To represent the Toric Code ground state as a PEPS we start by doubling the local degrees of freedom on each edge in the bulk. Bulk spins are denoted in red, while boundary spins are coloured blue. (b) Tensor diagrams of the tensors δ^B , δ^E and T introduced in the text. (b) The PEPS representation of the Toric Code ground state before contracting the tensors at each vertex, made up from the tensors (b).

This tensor ensures that all states with an odd number of down spins around a vertex have an amplitude of zero, satisfying condition (4.4).

We arrive at the PEPS in Figure 4.2c. Each basis state satisfying condition (4.4) results in the same amplitude when contracting the PEPS, while basis states violating the condition vanish. Thus, the PEPS represents the ground state of the Toric Code.

We now want to transform the PEPS into a YB-isoTPS. This can be easily done by choosing the correct rescaling for the vertex tensors, which transforms them into isometries as shown in Figure 4.3b. Note that a different rescaling needs to be chosen for tensors at the corners, edges, and in the bulk. For each vertex tensor we can choose the isometry direction to point to the left or to the right respectively, allowing us to place the orthogonality hypersurface anywhere in the lattice. As a last step, the tensors of the orthogonality hypersurface must be specified. The two spins that are connected to a tensor W of the orthogonality hypersurface must be in the same local state, since they were created by doubling the local degree of freedom. This constraint can be enforced by setting $W \in \mathbb{R}^{2 \times 1 \times 2 \times 1}$ to

$$W_{\alpha,\nu,\beta,\mu} = \frac{\delta_{\alpha,\beta}}{\sqrt{2}}$$

with dummy indices ν, μ of bond dimension 1, see Figure 4.3a. Trivially, the tensors W fulfil the isometry condition. We can again choose the direction of isometry to point either up or down for every W -tensor, allowing us to place the orthogonality center freely along the orthogonality hypersurface.

We have thus found an exact YB-isoTPS representation of the Toric Code ground state with $D = 2$ and $\chi = 1$, similar to the construction done in [27] for MM-isoTPS.

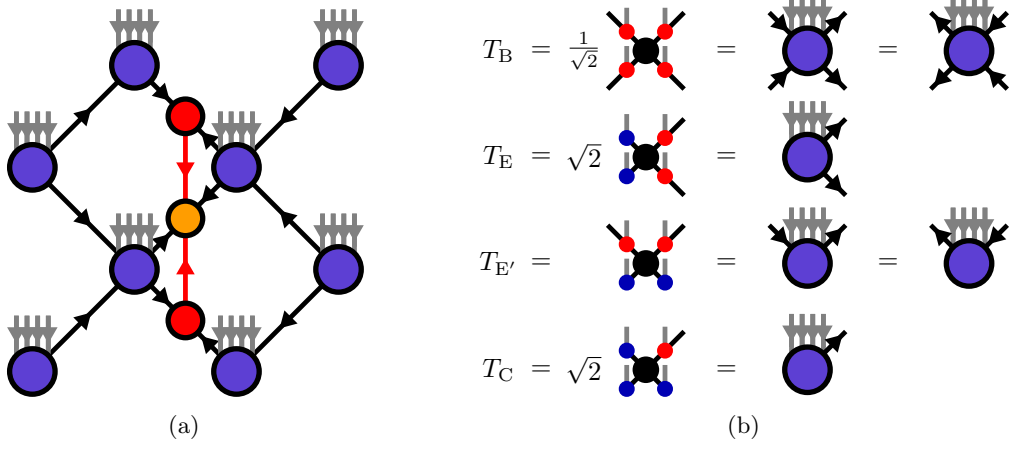


Figure 4.3: The PEPS in figure 4.2c can be transformed to the YB-isoTPS (a) by rescaling the tensors as shown in (b). Note that the tensors T'_E at the top and bottom edges of the lattice need a different rescaling than the tensors T_E at the left and right edges.

The final network is depicted in Figure 4.3a. We test the different algorithms for the YB move on the Toric Code ground state on a 5×5 lattice. All algorithms are able to move the orthogonality surface exactly up to computational accuracy. This however only works well if a good initialization is chosen for the disentangling unitary. We choose an initialization based on an SVD, see [23, 26] or our implementation [36].

Chapter 5

The Transverse Field Ising Model: Ground State Search and Time Evolution

The Transverse Field Ising (TFI) Model is a well-studied spin lattice model that is often used to benchmark numerical methods. We introduce the TFI model in Section 5.1. We then proceed by benchmarking YB-isoTPS methods on the model. We first perform ground state searches using imaginary time evolution in Section 5.2. We benchmark the different proposed algorithms for the YB move and compare the first and second order TEBD algorithms. We further show numerical evidence that YB-isoTPS are able to capture area law entanglement. Last, we perform a ground state search on the honeycomb lattice, showing that YB-isoTPS can be easily generalized to different lattice types. In Section 5.3, we perform a global quench and compute real time evolution. We observe that YB-isoTPS struggle with the rapid entanglement growth and discuss some ideas for overcoming the problem.

We compare the results obtained with YB-isoTPS to reference DMRG simulations using the tenpy library [38]. The DMRG simulations are performed by "snaking" an MPS through the 2D lattice as shown in Figure 5.1. The disadvantage of this method is that sites that are close to each other in the lattice can be far apart in the MPS. Because of the close proximity of these sites we expect entanglement to build up between them. This entanglement cannot be captured well by the MPS because of its finite bond dimension which is only able to capture entanglement locally in the MPS. We thus expect DMRG to break down for large systems. However, because of the low computational complexity of DMRG, one can scale the bond dimension to large values. For the lattice sizes we looked at, this still allows for well-converged results at reasonable computation times.

5.1 The Transverse Field Ising Model

The Transverse Field Ising (TFI) model is a well-studied spin lattice model that is described by the Hamiltonian

$$\hat{H}_{\text{TFI}} = -J \sum_{\langle i,j \rangle} \hat{\sigma}_i^x \hat{\sigma}_j^x - g \sum_i \hat{\sigma}_i^z, \quad (5.1)$$

with

$$\mathcal{N} = \left\| \sum_n \Psi_n e^{-E_n t} \right\|.$$

If we now take the limit $t \rightarrow \infty$ and assume that the ground state $|0\rangle$ with the lowest energy E_0 is nondegenerate, all states except the ground state vanish because of the exponential terms $e^{-E_n t}$. We end up with the ground state

$$|\Psi(t \rightarrow \infty)\rangle = |0\rangle.$$

To use the TEBD algorithm we must choose a good step size $\Delta\tau = -i\Delta t$. The total error of a single TEBD step evolving the YB-isoTPS by imaginary time $\Delta\tau$ is a sum of three errors,

$$\varepsilon_{\text{TEBD}} = \varepsilon_{\text{Trotter}} + \varepsilon_{\text{trunc}} + \varepsilon_{\text{YB}}.$$

The trotterization error $\varepsilon_{\text{Trotter}}$ comes from the Suzuki-Trotter decomposition, the truncation error $\varepsilon_{\text{trunc}}$ from locally applying the bond operators, and the YB error ε_{YB} arises when shifting the orthogonality hypersurface. A smaller time step Δt decreases both $\varepsilon_{\text{Trotter}}$ and $\varepsilon_{\text{trunc}}$ while the YB error ε_{YB} is not directly affected. However, since for a smaller time step Δt more TEBD iterations are necessary to approach the limit $t \rightarrow \infty$, YB errors add up and prevent the state from reaching the true ground state. Therefore we expect, similar to [23, 26], that the YB-error dominates for small time steps, while the trotterization and truncation errors dominate for larger time steps. The best results can be achieved when the time step Δt is tuned such that $\varepsilon_{\text{Trotter}} + \varepsilon_{\text{trunc}} \approx \varepsilon_{\text{YB}}$.

In Figure 5.2 we benchmark the different algorithms for the YB move that were discussed in Section 3.2. We perform an imaginary time evolution of the TFI model with a transverse field of $g = 3.5$, using second order TEBD and time steps $\Delta t \in [0.02, 0.5]$. We used the second order TEBD algorithm as discussed in Section 3.3, with a maximum of $N_{\text{iter,TEBD}} = 100$ iterations of the Evenly-Vidal style algorithm for applying local bond operators. The model is put on a 4×4 square lattice containing $N = 32$ spins. For each data point we start at $\Delta t = 0.5$, slowly decreasing the time step until arriving at the desired time step Δt . We then perform another 50 TEBD iterations and compute the average energy of the last 20 iterations. The relative error compared to the numerically exact DMRG reference simulation with a bond dimension of $\chi = 1024$ is then computed and plotted against the time step Δt . Additionally, we plot the accumulated walltime of all YB-moves during a single TEBD step for a bond dimension $D = 4$ in Figure 5.3. For this measurement, the algorithms were run on a i5-12500 CPU with 6 cores.

We will compare the different algorithms row by row, starting with the left-most plot in the first row of Figure 5.2, where we used a simple **SVD** without any disentangling for the YB move. The resulting error is large and the ground state energy is only

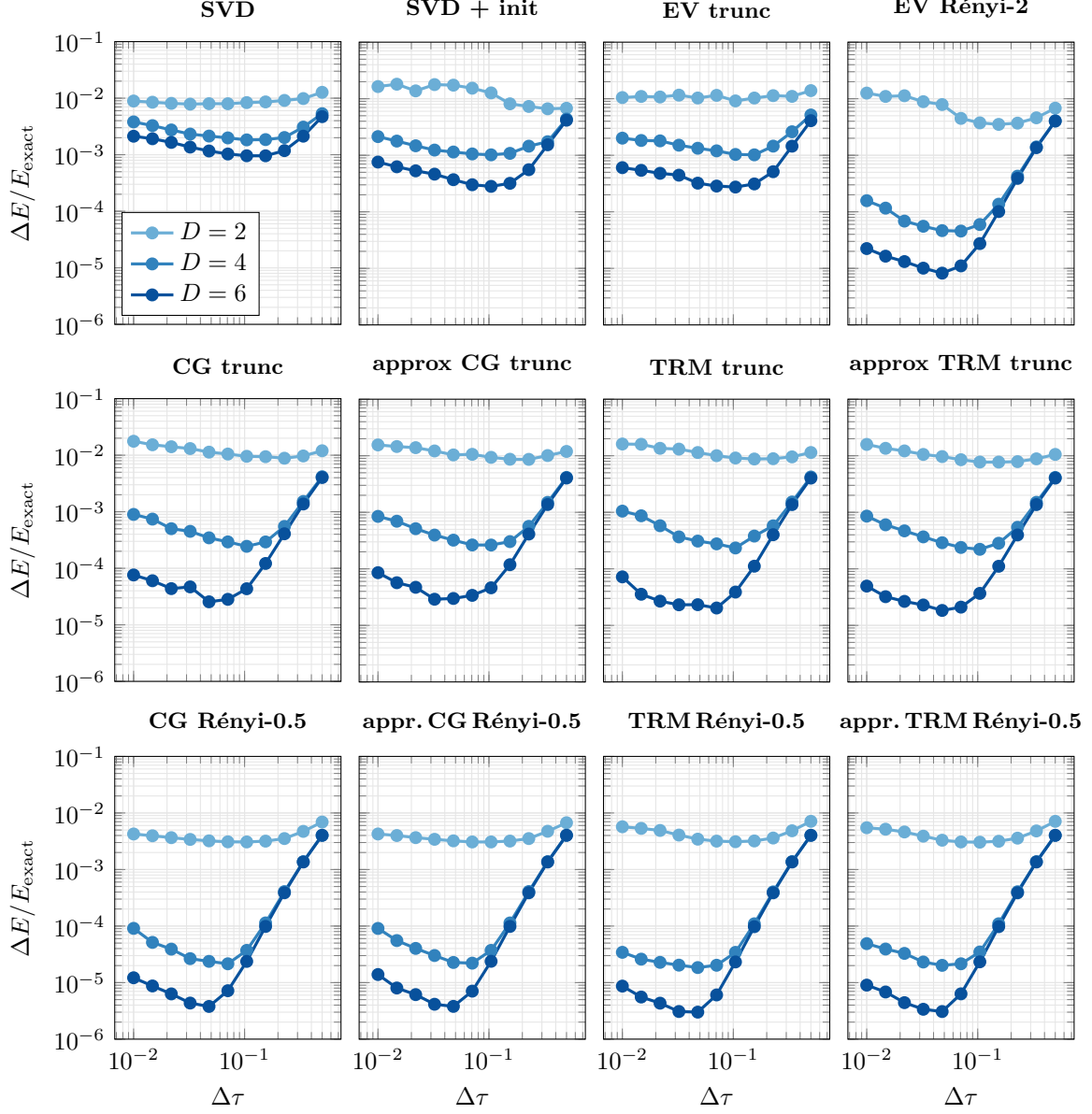


Figure 5.2: We benchmark the different implemented methods for the YB move on the TFI model on a 4×4 square lattice. The transverse field is set to $g = 3.5$. We compute the ground state energy with imaginary TEBD for different time step sizes $\Delta\tau$. First row: SVD splitting without disentangling, SVD splitting with a disentangling unitary initialized with an SVD as in [23, 26], Evenbly-Vidal minimization of the truncation error, and Evenbly-Vidal minimization of the Rényi-2 entropy. Second row: Disentangling with Riemannian optimization of the truncation error. Third row: Disentangling with Riemannian optimization of the Rényi-1/2 entropy. All iterative methods were run for a maximum of $N_{\text{iter}} = 100$ iterations per YB move. The bond dimension of the orthogonality hypersurface was set to $\chi = 6 \cdot D$.

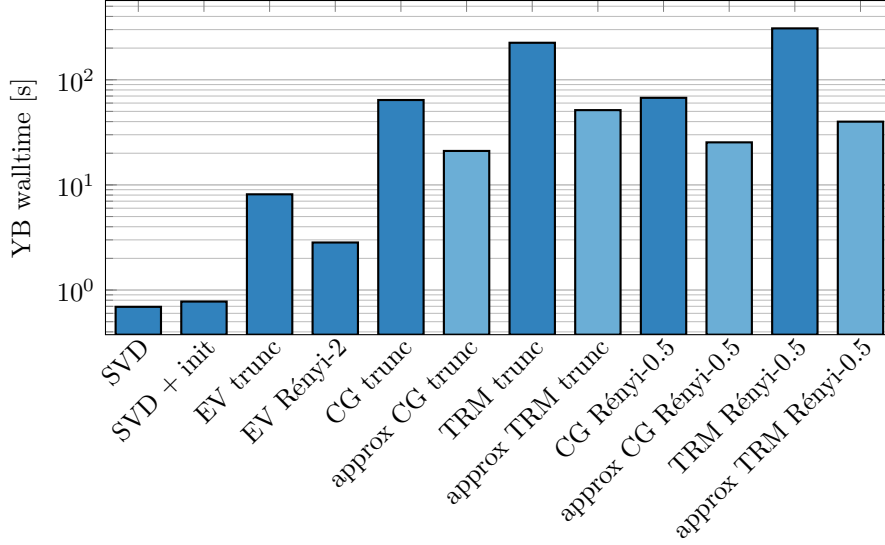


Figure 5.3: In this figure we compare the duration that the different algorithms spend on the YB move during a single TEBD time step (updating the complete YB-isoTPS by an imaginary time $\Delta\tau$). We compute this accumulated walltime by running TEBD for $N_{\text{TEBD}} = 10$ steps, measuring the time spent performing YB moves, and computing the average walltime per TEBD step. We compare all methods benchmarked in figure 5.2. We plot the exact and approximate versions of the Riemannian optimization algorithms next to each other and denote the approximate versions with a lighter color.

found up to an accuracy of $\approx 10^{-3}$. If we use the initialization procedure from [23, 26] as a naive guess for the disentangling unitary (**SVD + init**), the ground state estimate improves by half an order of magnitude. Using the Evenbly-Vidal algorithm minimizing the truncation error for the YB move (**EV trunc**) as discussed in Section 3.2.1 results in a comparable error. In the right-most plot of the first row of Figure 5.2 we used the Evenbly-Vidal algorithm for disentangling, optimizing the Rényi entropy with $\alpha = 2$ (**EV Rényi-2**). This improves the results drastically, pushing the relative error below 10^{-5} .

The second row of Figure 5.2 shows the results obtained when disentangling by optimizing the truncation error using Riemannian optimization. We test both CG (**CG trunc**) and the TRM (**TRM trunc**), together with their approximate versions **approx CG trunc** and **approx TRM trunc**. CG and TRM perform very similar, and notably the approximate version of both algorithms performs almost as good as the exact version while being much faster. As a whole, disentangling by minimizing the truncation error gives worse results than when minimizing the Rényi-2-entropy. The reason for this is the following: While minimizing the truncation error leads to a smaller error for a single YB-move, it can lead to a larger error for the following YB-

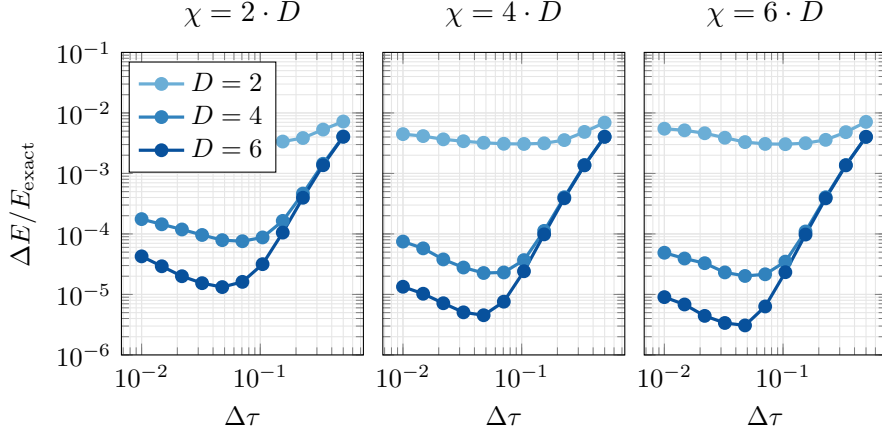


Figure 5.4: In this figure we test the effect of using different maximum bond dimensions χ for the orthogonality hypersurface. For the YB move we used the approximate TRM algorithm optimizing the Rényi-0.5 entropy. The optimization was run for a maximum of $N_{\text{iter}} = 100$ iterations per YB move. As a model we use the TFI model on a 4×4 square lattice with a transverse field of $g = 3.5$. We compute the ground state energy with imaginary TEBD for different time step sizes $\Delta\tau$.

moves on the same column. When adding together the errors of all YB moves that are necessary for moving the orthogonality hypersurface, truncation error disentangling performs worse than Rényi-entropy disentangling in our testing. We suspect that the reason for this is that a disentangling of the entanglement entropy leads to a more “physical” representation, which is able to better capture the entanglement across the orthogonality hypersurface.

In the last row of Figure 5.2 we compare the different algorithms using Riemannian optimization to disentangling by minimizing the Rényi entropy with $\alpha = 1/2$. Again we benchmark both CG (**CG Rényi-0.5**), the TRM (**TRM Rényi-0.5**) and the approximate versions of both algorithms (**approx CG Rényi-0.5**, **approx TRM Rényi-0.5**). TRM performs only slightly better than CG. The approximate versions of the two algorithm again produce a similar error compared to the exact versions while being much faster.

To conclude, we find that disentangling by optimizing the Rényi $\alpha = 1/2$ entropy with the approximate TRM is the best method out of all methods tested. We will therefore use this method for the following plots.

As a next test, we want to observe the effect of choosing a different bond dimension $\chi = f \cdot D$ along the orthogonality hypersurface. We compare $f \in \{2, 4, 6\}$ in Figure 5.4. We observe that for large f the effect of increasing f further is only small, and one should instead increase the overall bond dimension D to achieve more accurate results.

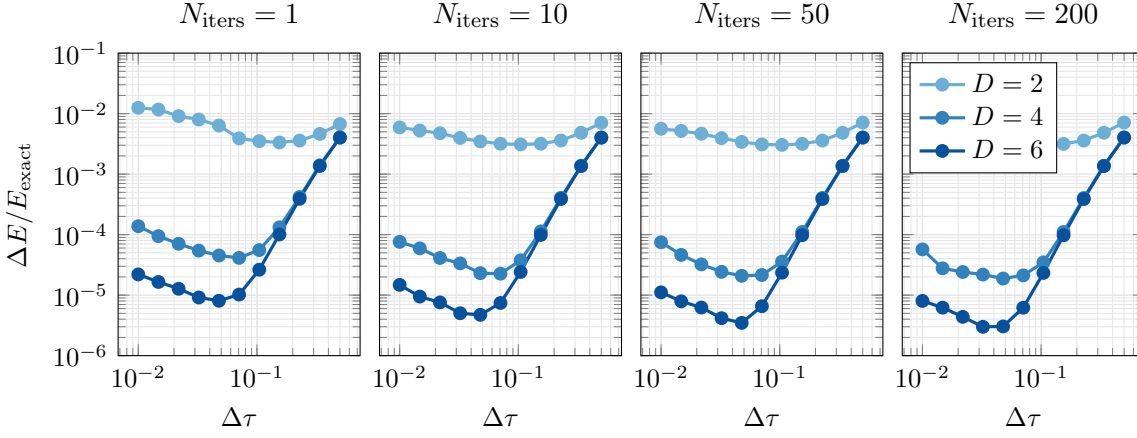


Figure 5.5: In this figure we test how many iterations of Riemannian optimization are necessary for the approximate TRM algorithm minimizing the Rényi-0.5 entropy to converge. As a model we use the TFI model on a 4×4 square lattice with a transverse field of $g = 3.5$. The bond dimension of the orthogonality hypersurface is set to $\chi = 6 \cdot D$. We compute the ground state energy with imaginary TEBD for different time step sizes $\Delta\tau$.

It is also interesting to observe how many iterations of the TRM optimization are necessary for the disentangling to converge. In Figure 5.5 we compare different values for the maximum number of iterations $N_{\text{iter}} \in \{1, 10, 50, 200\}$. We observe that already for $N_{\text{iter}} = 50$ the algorithm is mostly converged. This is unexpected, especially when comparing this to Figure 3.16 in Section 3.2.2, where we qualitatively show that the optimization during a single YB move needs $N_{\text{iter}} \approx 10^3$ iterations to converge. The reason for this discrepancy is that for imaginary TEBD it is not necessary for the YB move to be fully converged. By applying an iteration of imaginary TEBD, the state is changed and projected further towards the ground state. Since most of the minimization in the YB move happens in the first few iterations, the incremental improvements of successive iterations do not play a big role. We expect that going to a higher number of maximum iterations will be more important when performing real-time evolution, where the error of shifting the orthogonality hypersurface should be as low as possible, since else the state diverges from the exact solution.

We compare first and second order TEBD in Figure 5.6. For the YB move we again use the approximate Rényi-0.5 disentangler. We observe that TEBD2 allows us to reach an relative error in energy that is over an order of magnitude smaller than when using TEBD1. Note that the minimum in error is located at a much larger $d\tau$ for TEBD2 compared to TEBD1. The reason for this is that the lower Suzuki-Trotter error of TEBD2 allows us to go to larger $d\tau$, decreasing the number of YB move per unit time, which results in a more accurate computation.

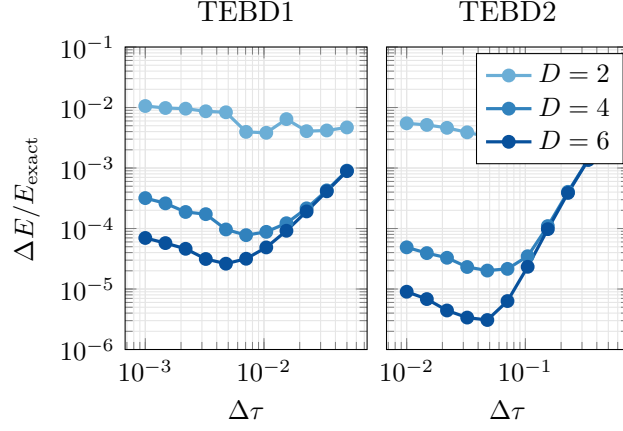


Figure 5.6: In this figure we compare the TEBD algorithms of first and second order, TEBD1 and TEBD2. For the YB move we used the approximate TRM algorithm optimizing the Rényi-0.5 entropy. The optimization was run for a maximum of $N_{\text{iter}} = 100$ iterations per YB move. As a model we use the TFI model on a 4×4 square lattice with a transverse field of $g = 3.5$. The bond dimension of the orthogonality hypersurface was chosen as $\chi = 6 \cdot D$. We compute the ground state energy with imaginary TEBD for different time step sizes $\Delta\tau$.

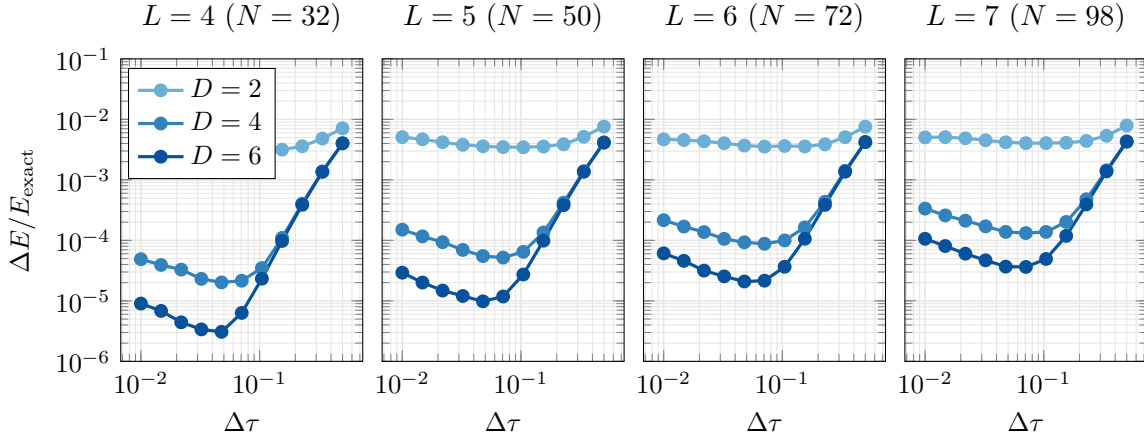


Figure 5.7: In this figure we test how well an approximate ground state can be found by using imaginary TEBD on different system sizes. For the YB move we used the approximate TRM algorithm optimizing the Rényi-0.5 entropy. The optimization was run for a maximum of $N_{\text{iter}} = 100$ iterations per YB move. As a model we use the TFI model on a $L \times L$ square lattice with a transverse field of $g = 3.5$. The bond dimension of the orthogonality hypersurface was chosen as $\chi = 6 \cdot D$. We compute the ground state energy with imaginary TEBD for different time step sizes $\Delta\tau$.

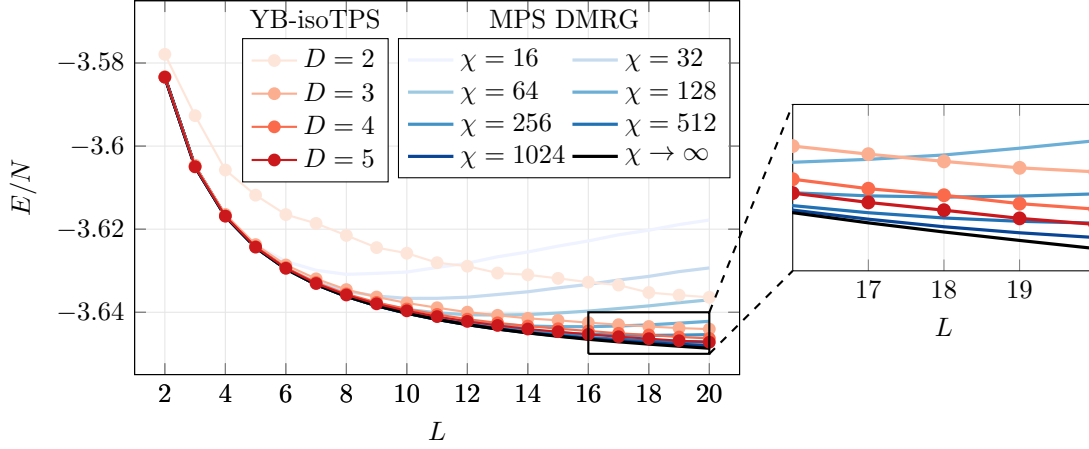


Figure 5.8: In this figure we plot the energy density E/N of the TFI model against the linear system size L . The system is put on a diagonal $L \times L$ square lattice consisting of $N = 2L^2$ spins, at a transverse field of $g = 3.5$. DMRG results are extrapolated to infinite bond dimension $\chi \rightarrow \infty$. The YB-isoTPS results were achieved with imaginary TEBD. For the YB move we used the approximate TRM Rényi-0.5 disentangler, which was run for a maximum of $N_{\text{iter}} = 100$ iterations per YB move. The maximum bond dimension of the orthogonality hypersurface was set to $\chi = 6 \cdot D$.

Next, we go to larger system sizes. In Figure 5.7, we perform the energy minimization for the TFI model on $L \times L$ square lattices with $L \in \{4, 5, 6, 7\}$. Because the chosen unit cell contains two spins, the total number of spins on a $L \times L$ lattice is $N = 2L^2$. While we observe that the relative error in ground state energy increases when going to larger system sizes, it seems to converge to a constant relative energy error for large L . To further investigate this, we plot the energy density against the linear system size in Figure 5.8, going up to a system size of $L = 20$, which corresponds to $N = 800$ spins. The reference data was again computed using DMRG on MPS. We additionally extrapolated the MPS bond dimension $\chi \rightarrow \infty$ to obtain a better energy estimate. This can be done because it is observed in practice that the ground state energy obtained with DMRG scales linearly with the truncation error [60]. To perform the extrapolation one plots the energy against the truncation error at different bond dimensions and extrapolates to a truncation error of zero. This process is shown for $L = 20$ in Figure 5.9.

In the limit $L \rightarrow \infty$ we expect the energy density to approach a constant $E/N \rightarrow \text{const.}$, whereas the energy density of small systems is dominated by finite size effects. We observe that the energy density computed using DMRG first decreases but then increases again when going to larger system sizes. This happens earlier for smaller bond dimensions and can be explained by the fact that the MPS is not able to correctly capture the entanglement structure of the model. In contrast, the energy

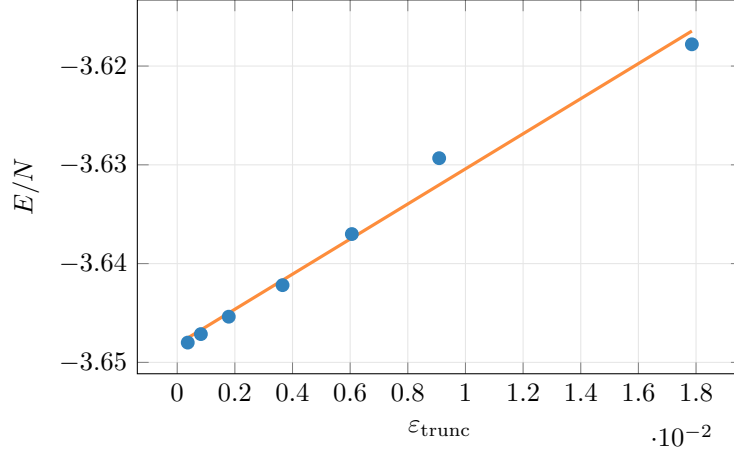


Figure 5.9: In this figure we show the extrapolation of $\chi \rightarrow \infty$ for the DMRG bond dimension χ . We plot the energy density obtained for the TFI model on a 20×20 diagonal square lattice at a transverse field of $g = 3.5$ using the tenpy reference simulation [38] at different bond dimensions χ against the truncation error that was measured during the simulation. Higher bond dimensions lead to a lower error. One observes that the energy density scales linearly with the error. Extrapolating to an error of $\varepsilon_{\text{trunc}} = 0$ as shown with the linear fit yields an approximation of the exact energy density at $\chi \rightarrow \infty$.

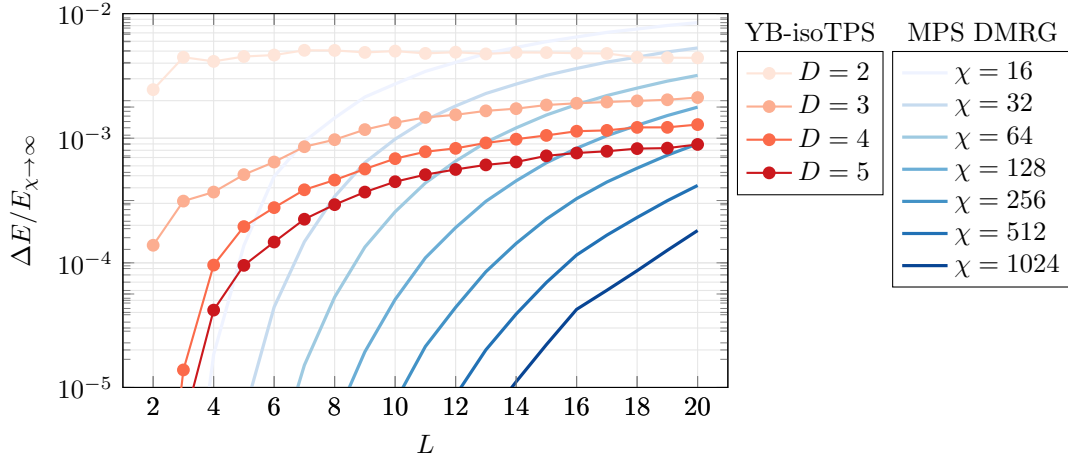


Figure 5.10: In this figure we visualize the data from figure 5.7 by plotting the relative ground state energy error with respect to the energy obtained from extrapolating the DMRG simulation to $\chi \rightarrow \infty$. One can observe that the energy error of the YB-isoTPS simulation approaches a constant for large L .

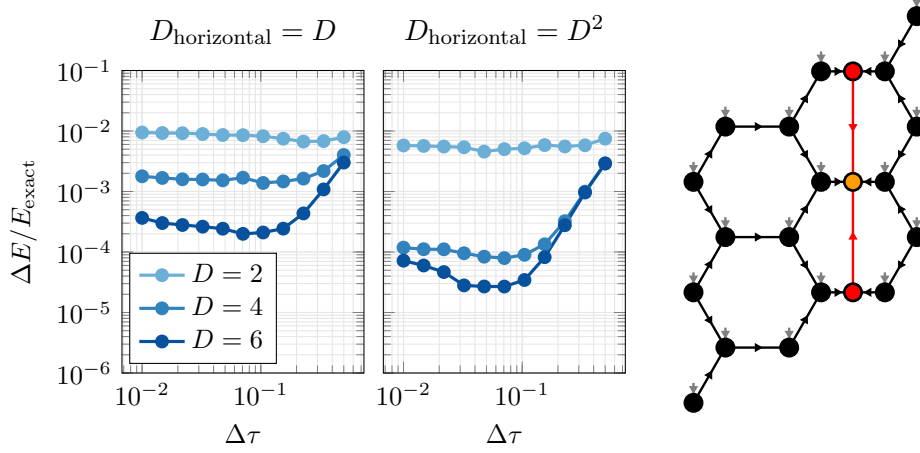


Figure 5.11: In this figure we show imaginary TEBD results using YB-isoTPS on the honeycomb lattice. We used two different values for the horizontal bond dimension, $D_{\text{horizontal}} = D$ and $D_{\text{horizontal}} = D^2$. The bond dimension along the orthogonality hypersurface was chosen as $\chi = 6 \cdot D$. For the YB move we used the approximate Rényi-0.5 disentangler with a maximum of $N_{\text{iter}} = 100$ iterations per YB move. The model is the TFI model on a 4×4 honeycomb lattice at a transverse field of $g = 3.5$. On the right we show the YB-isoTPS structure of a 3×3 honeycomb lattice.

density computed using YB-isoTPS does not show this effect and seems to approach a constant energy density. This can be interpreted as the YB-isoTPS being able to correctly capture the 2D area law entanglement structure. This effect is better visible in Figure 5.10, where we plot the relative ground state energy error compared to the extrapolated $\chi \rightarrow \infty$ DMRG energy. While for the system sizes we looked at, DMRG with $\chi = 1024$ was still able to find a state with a lower energy than YB-isoTPS with $D = 5$ and $\chi = 30$, we expect this to change for even larger systems or for more complicated models, where capturing the area law entanglement structure becomes more important.

Last, to show the generalization of YB-isoTPS to other lattice types, we implemented YB-isoTPS on the honeycomb lattice. The network structure is shown on the right in Figure 5.11. For details of the implementation see [36]. For YB-isoTPS on the honeycomb lattice it can be beneficial to choose a larger bond dimension $D_{\text{horizontal}}$ for horizontal bonds, since else the maximal bond dimension of the diagonal bonds is not reached even in the bulk, see Figure 5.12. We test this in Figure 5.11, where we compute the ground state energy of the TFI model on a 4×4 honeycomb lattice. We run the algorithm once with $D_{\text{horizontal}} = D$ and once with $D_{\text{horizontal}} = D^2$, which improves the results but also has a higher computational cost. Further testing is required to determine which bond dimension should be chosen in practice.

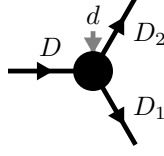


Figure 5.12: If the maximum horizontal bond dimension of the honeycomb YB-isoTPS is set to D , a physical tensor in the bulk must fulfil the isometry condition $D \cdot d \leq D_1 \cdot D_2$. Since most often $d < D$, the maximum bond dimension can't be reached for the outgoing legs D_1, D_2 . This can create anisotropies in the tensor network.

5.3 Time Evolution after a Global Quench

As a second experiment, we study the capabilities of YB-isoTPS to perform real-time evolution. For this we perform a global quench by initializing the YB-isoTPS to a product state, which we then evolve in time, measuring local expectation values. We start with an all-up-state $|\Psi\rangle = |\uparrow\rangle \otimes \cdots \otimes |\uparrow\rangle$ on the 8×8 diagonal square lattice and evolve with the Hamiltonian of the TFI model at critical transverse field $g \approx 3.04438$. At the critical field the entanglement grows very quickly, making this a hard problem. For the YB-isoTPS we choose bond dimensions of $D \in \{2, 3, 4, 5, 6\}$, $\chi = 6 \cdot D$ and a step size of $\Delta t = 0.02$. We evolve up to time $t = 1.0$, requiring 50 full TEBD iterations. For the YB-move we used approximate TRM disentangling optimizing the Rényi $\alpha = 0.5$ entropy for a maximum number of $N_{\text{iter,YB}} = 100$ iterations. For the application of the TEBD bond operators we used a maximum of $N_{\text{iter,TEBD}} = 100$ iterations. For a comparison we used the MPO-time evolution algorithm from [61] defined on MPS, which is able to perform time evolution in the presence of long range interactions and is implemented in `tenpy` [38]. For this reference simulation we used bond dimensions ranging from $\chi = 16$ to $\chi = 1024$ and a time step of $\Delta t = 0.01$. We show the results in Figure 5.13. We observe that YB-isoTPS is in good agreement with the reference simulation up to a time of $t \approx 0.2$, at which the expectation value diverges. This happens at earlier times for smaller bond dimensions D . We expect that this fast divergence is due to the accumulated error of the YB move. One could improve the method by applying a per-column variational optimization as done in isoTPS [23, 26], which was found to be essential for real-time evolution [26], or by otherwise improving the YB move.

Finally, we want to test the time evolution in a less challenging regime, for which we used the TFI model at a transverse field of $g = 6$, which is well in the paramagnetic phase. In this regime, entanglement is expected to build up much slower than when simulating at the critical field. We again initialize an all-up-state $|\Psi\rangle = |\uparrow\rangle \otimes \cdots \otimes |\uparrow\rangle$ on the 8×8 square lattice but additionally flip a spin in the center into the down-state $|\downarrow\rangle$. We then compute the time evolution of the $\langle \hat{\sigma}_z \rangle$ expectation value of the flipped center spin and neighboring spins. The results are shown in Figure 5.14. Note

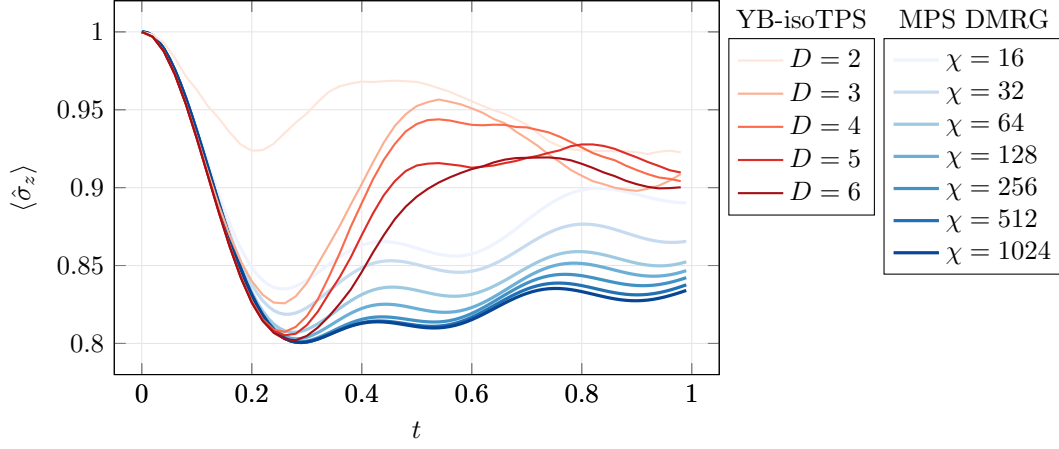


Figure 5.13: In this figure we show the time evolution of the $\langle \hat{\sigma}_z \rangle$ expectation value of a spin in the middle of the 8×8 diagonal square lattice, containing in total $N = 128$ spins. As a model we use the TFI model at critical field g_C . We compute the time evolution once with DMRG on a MPS and once with YB-isoTPS with the parameters given in the text. We observe good agreement up to times of $t \approx 0.2$, when the YB-isoTPS results diverge from the DMRG reference simulation.

that the DMRG reference simulation converges for much lower bond dimensions χ compared to Figure 5.13. We also observe much better agreement of YB-isoTPS TEBD and MPS DMRG.

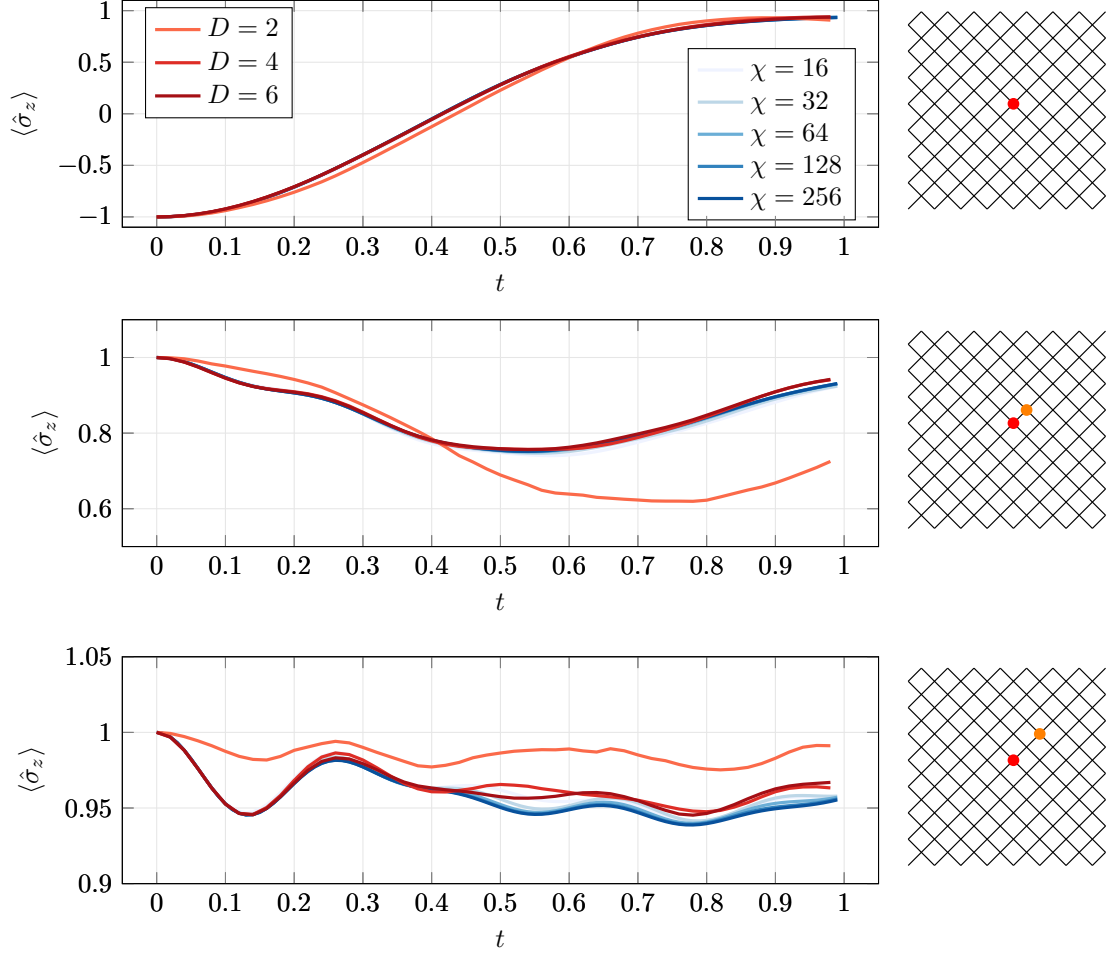


Figure 5.14: In this figure we show the time evolution of the $\langle \hat{\sigma}_z \rangle$ expectation value of a spin in the middle of the lattice and its neighboring spins. The position of the measured spins is visualized in orange in the lattice next to the plots. As an initial state we choose the all-up state, with a spin in the center of the lattice flipped to the down-state $|\downarrow\rangle$. We draw the flipped spin in red. As a model we use the TFI model in the paramagnetic phase with a transverse field of $g = 6$, put on an 8×8 diagonal square lattice containing in total $N = 128$ spins. We compute the time evolution once with DMRG on a MPS and once with YB-isoTPS with the parameters given in the text.

Chapter 6

Conclusion and Outlook

In this thesis, a new ansatz for defining the canonical form of isometric tensor product states in 2D was implemented. In Chapter 2 an introduction to tensor networks, isometric tensor networks, Matrix Product States (MPS) and isometric Tensor Product States (isoTPS) was given. The new ansatz for defining the canonical form on isoTPS, which we call YB-isoTPS, was introduced in Chapter 3. Several algorithms were discussed for moving the orthogonality hypersurface through the YB-isoTPS, which is done by performing so-called Yang-Baxter (YB) moves. It was found that a Riemannian disentangling procedure that minimizes the truncation error yields the lowest error for a single YB move. This was also found in previous works on MM-isoTPS [23, 26]. Further, an approximate algorithm was introduced for computing the required gradients and Hessian-vector products of the cost functions, decreasing the computational cost from $\mathcal{O}(D^9)$ to $\mathcal{O}(D^8)$. A qualitative comparison of the different methods revealed that the approximate versions of the algorithms perform nearly as well as the exact versions, while being significantly faster. The introduced algorithms were then tested in Chapters 4 and 5. In Chapter 4 it was shown that YB-isoTPS are able to represent the ground state of the Toric Code model, with the YB move being able to shift the orthogonality hypersurface without error up to numerical accuracy. In Chapter 5, imaginary and real time evolution with the TEBD algorithm was used to find ground states and perform global quenches of the Transverse Field Ising model. It was found that YB-isoTPS are able to produce similar results to MM-isoTPS. The algorithms performing best in the ground state search were found to be the Riemannian optimization algorithms minimizing the Rényi entropy with $\alpha = 1/2$. In a large scale simulation of up to $N = 800$ spins, numerical evidence was found that YB-isoTPS are able to correctly capture the area law entanglement structure of the ground state. While at this regime a reference simulation of DMRG on MPS with a large bond dimension of $\chi = 1024$ was still able to produce lower ground state energies, it is expected that this will change when moving to larger system sizes or more challenging models. Additionally, the ansatz was used to compute the ground state energy of the TFI model on a honeycomb lattice, showcasing that YB-isoTPS can be easily generalized to other lattice types. Computing a real time evolution after a global quench was found to

be a very challenging problem for YB-isoTPS. Because of the accumulation of YB errors, the time evolution diverges from the reference simulation after short times. This issue becomes less significant when moving away from the critical point, which corresponds to an easier problem due to the slower growth of entanglement over time. Nevertheless, YB-isoTPS were found to be able to correctly capture short-time behaviour of two-dimensional lattice systems of $N = 128$ spins even at criticality.

To summarize, the YB-isoTPS ansatz is able to produce comparable results to MM-isoTPS. While the computational complexity of shifting the orthogonality hypersurface of YB-isoTPS is larger ($\mathcal{O}(D^8)$ compared to $\mathcal{O}(D^7)$) it is still an interesting alternative way of defining the isometry condition. One advantage of YB-isoTPS is the ease with which the ansatz can be generalized to different lattices. For instance, extending it to the Kagome lattice is expected to be feasible without increasing the cost of the YB move. Moreover, more involved algorithms like DMRG require the contraction of a boundary MPS, which has a computational complexity scaling as $\mathcal{O}(D^{12})$. For such algorithms, we expect the increased cost for the YB move compared to the MM to not make a large difference.

It would be interesting to implement a DMRG algorithm on YB-isoTPS and compare its performance to isoTPS. Future research could explore alternative algorithms for performing the YB move, which we find to be the main source of errors. Similar to MM-isoTPS, implementing a variational optimization on the complete column when shifting the orthogonality surface may be beneficial, as this was found to be essential for achieving good results when performing time evolution with MM-isoTPS [26]. Additionally, extending the method to the thermodynamic limit and further investigating the connection between isoTPS and quantum computing [30, 31] are promising research directions. Finally, the algorithm could significantly benefit from an implementation on Graphics Processing Units (GPUs), which can greatly accelerate tensor contractions and decompositions while also increasing the power efficiency.

Appendix A

Optimization Problems for Isometric Tensor Networks

When discussing algorithms on isometric tensor networks, one often needs to find optimal tensors extremizing a given cost function f . In the most general case, f is a function

$$f : \mathbb{C}^{m_1 \times n_1} \times \mathbb{C}^{m_2 \times n_2} \times \dots \times \mathbb{C}^{m_K \times n_K} \rightarrow \mathbb{R},$$

mapping K tensors T_1, \dots, T_K to a scalar cost value. Here, the tensors have already been reshaped into matrices, grouping together legs with incoming arrows and legs with outgoing arrows respectively. The tensors must satisfy certain constraints. If a tensor T_i possesses both legs with incoming arrows and legs with outgoing arrows, it must satisfy the isometry constraint $T_i^\dagger T_i = \mathbb{1}$, where without loss of generalization we assumed $m_i \geq n_i$. If instead the tensor T_j possesses only legs with incoming arrows (and thus is the orthogonality center), it is constrained to be normalized to one, $\|T_j\|_F = 1$. To summarize, we want to solve the optimization problem

$$T_1^{\text{opt}}, \dots, T_K^{\text{opt}} = \underset{T_1, \dots, T_K}{\operatorname{argmax}} f(T_1, \dots, T_K) \quad (\text{A.1})$$

under the constraints

$$T_i^\dagger T_i = \mathbb{1}$$

for isometries T_i and

$$\|T_j\|_F = 1$$

for the orthogonality center T_j .

In the following, we will discuss several approaches for solving optimization problem (A.1). We will first assume that the input of the cost function is a single tensor T . If the cost function is linear, the problem is known as the *orthogonal Procrustes problem* and we discuss its closed form solution in Section A.1. Non-linear cost functions can be optimized by using the Evenbly-Vidal algorithm, see Section A.2. Finally, we will discuss how cost functions of multiple tensors can be optimized in Section A.3.

A different, more involved approach to solving the optimization problem is given by Riemannian optimization, which we discuss in Appendix B.

A.1 The orthogonal Procrustes problem

If the cost function is linear, it can be written as

$$f(T) = \sum_{j=1}^m \sum_{k=1}^n [\alpha_{j,k} \operatorname{Re}(T_{j,k}) + \beta_{j,k} \operatorname{Im}(T_{j,k})]$$

with parameters $\alpha_{j,k}, \beta_{j,k} \in \mathbb{R}$. Introducing the *environment tensor* $E \in \mathbb{C}^{m \times n}$ as $E_{j,k} = \alpha_{j,k} + i\beta_{j,k}$, we can write the cost function as

$$f(T) = \sum_{j=1}^m \sum_{k=1}^n \operatorname{Re}(E_{j,k}^* T_{j,k}) = \operatorname{Re} \operatorname{Tr}(E^\dagger T) = \operatorname{Re} \operatorname{Tr}(T^\dagger E).$$

Maximizing $f(T)$ under the isometry constraint $T^\dagger T = \mathbb{1}$ is known as the orthogonal Procrustes problem and permits the closed form solution

$$T_{\text{opt}} = \operatorname{argmax}_{T^\dagger T = \mathbb{1}} \operatorname{Re} \operatorname{Tr}(T^\dagger E) = UV^\dagger, \quad (\text{A.2})$$

where the matrices U and V are computed using an SVD $E = USV^\dagger$. To prove this result we insert the SVD into the cost function as

$$\begin{aligned} f(T) &= \operatorname{Re} \operatorname{Tr}(ET^\dagger) = \operatorname{Re} \operatorname{Tr}(USV^\dagger T^\dagger) = \operatorname{Re} \operatorname{Tr}\left[\left(U\sqrt{S}\right)\left(\sqrt{S}V^\dagger T^\dagger\right)\right] \\ &= \operatorname{Re} \left\langle \sqrt{S}U^\dagger, \sqrt{S}V^\dagger T^\dagger \right\rangle_{\text{F}}. \end{aligned}$$

We next use the fact that the Frobenius inner product satisfies the Cauchy-Schwarz inequality to obtain the upper bound

$$\begin{aligned} f(T) &= \operatorname{Re} \left\langle \sqrt{S}U^\dagger, \sqrt{S}V^\dagger T^\dagger \right\rangle_{\text{F}} \leq \left\| \sqrt{S}U^\dagger \right\|_{\text{F}} \left\| \sqrt{S}V^\dagger T^\dagger \right\|_{\text{F}} \\ &= \sqrt{\operatorname{Tr}(USU^\dagger) \operatorname{Tr}(TVSV^\dagger T^\dagger)} = \operatorname{Tr}(S), \end{aligned}$$

where in the last step we used $U^\dagger U = \mathbb{1}$, $V^\dagger V = \mathbb{1}$, $T^\dagger T = \mathbb{1}$ and the cyclic property of the trace. This upper bound is reached by the solution

$$F(T_{\text{opt}}) = \operatorname{Re} \operatorname{Tr}(USV^\dagger VU^\dagger) = \operatorname{Tr}(S),$$

proving (A.2).

If the tensor T must not satisfy the isometry condition but must be normalized to one, the closed form solution can be found as

$$T_{\text{opt}} = \operatorname{argmax}_{\|T\|=1} \operatorname{Re} \operatorname{Tr}(T^\dagger E) = E / \|E\|. \quad (\text{A.3})$$

We arrive at this solution through a similar argument as before. First, we obtain an upper bound

$$f(T) = \text{Re Tr} \left(T^\dagger E \right) = \text{Re} \langle T, E \rangle_F \leq \|T\| \|E\| = \|E\|$$

using the Cauchy-Schwarz inequality and the normalization constraint $\|T\| = 1$. We proceed by showing that the upper bound is reached by T^{opt} ,

$$f(T_{\text{opt}}) = \text{Re Tr} \left(E E^\dagger / \|E\| \right) = \|E\|,$$

proving (A.3).

A.2 The Evenbly-Vidal algorithm

In general the cost function $f(T)$ is not linear. For example, a non-linear cost function is encountered in the disentangling procedure when optimizing a MERA wave function [45]. It was proposed by Evenbly and Vidal [45, 46] to linearize the cost function and to update the tensor T iteratively using the closed form solutions from Section A.1. Let us assume that the cost function $f(T)$ can be written as the contraction of a tensor network, where in general the tensor T may appear multiple times. We contract all tensors except one of the tensors T into an environment tensor $E_T \in \mathbb{C}^{n \times n}$ and the cost function becomes

$$f(T) = \text{Re Tr} (E_T T).$$

We now keep the environment E_T fixed, treating it as if it were independent of T , and updating T with the closed form solutions (A.2) or (A.3). This is repeated until T is converged. If and how fast T converges depends on the details of the cost function, but convergence cannot be guaranteed for arbitrary cost functions.

One can also use Riemannian optimization for the optimization of general non-linear cost functions of isometries. This method is more powerful but also more involved and is discussed in Appendix B.

A.3 Cost functions of multiple tensors

cost functions of multiple tensors T_1, \dots, T_K can be optimized iteratively via an algorithm similar to the Evenbly-Vidal algorithm. The idea is to optimize one tensor at a time, keeping all other tensors fixed. To optimize the tensor T_i , we again contract all other tensors into an environment tensor E . If the environment tensor is independent of T_i (i.e. if the cost function is linear in T_i), we can update the tensor with the closed form solutions of Section A.1. Such an update is locally optimal in the

sense that it maximizes $f(T_1, \dots, T_K)$ for fixed tensors T_j , $j \neq i$. If the environment tensor is dependant of T_i , we need to use the Evenbly-Vidal algorithm (see Section A.2) or Riemannian optimization (see Appendix B). If the cost function is linear in all tensors T_1, \dots, T_K and bounded $f(T_1, \dots, T_K) \leq c \in \mathbb{R}$, this algorithm is guaranteed to converge, since each local update is optimal and thus the cost function can never decrease.

An alternative approach for optimizing a cost function of multiple tensors is given by Riemannian optimization over product manifolds [50].

Appendix B

Riemannian Optimization of Isometries

In this appendix we provide a brief introduction to Riemannian optimization, which can be used to optimize a cost function on the constrained set of isometric matrices. We optimize over the matrix manifold of isometric matrices, which is called the Stiefel manifold. For a more in-depth introduction to the topic we recommend the excellent book [48]. Riemannian optimization of complex matrix manifolds is discussed in the context of quantum physics and isometric tensor networks in [50, 51]. An implementation of Riemannian Optimization on the real Stiefel manifold and other matrix manifolds in python is given in [52]. Some parts of this implementation were also used in our implementation [36].

B.1 The complex Stiefel manifold

We define the *complex Stiefel manifold* $\text{St}(n, p)$ with $n \geq p$ as the set of all isometric $n \times p$ matrices:

$$\text{St}(n, p) := \left\{ X \in \mathbb{C}^{n \times p} : X^\dagger X = \mathbb{1} \right\}.$$

In particular, for $n = p$, the complex Stiefel manifold reduces to the set of unitary matrices $U(n)$. One can show, similar to [48], that the complex Stiefel manifold is naturally an embedded submanifold of the Euclidian vector space $\mathbb{C}^{n \times p} \cong \mathbb{R}^{2np}$ of general complex $n \times p$ matrices.

Tangent vectors on manifolds generalize the notion of directional derivatives. A mathematical definition of tangent vectors and tangent spaces of manifolds is given in [48]. The set of all tangent vectors to a point $X \in \text{St}(n, p)$ is called the *tangent space* $T_X \text{St}(n, p)$, which is given by [48, 50]

$$T_X \text{St}(n, p) = \left\{ Z \in \mathbb{C}^{n \times p} : X^\dagger Z + Z^\dagger X = 0 \right\}.$$

An arbitrary element $\xi \in \mathbb{C}^{n \times p}$ from the embedding space $\mathbb{C}^{n \times p}$ can be projected to the tangent space $T_X \text{St}(n, p)$ by [48, 50]

$$P_X \xi = \xi - \frac{1}{2} X \left(X^\dagger \xi + \xi^\dagger X \right). \quad (\text{B.1})$$

Additionally, we will also need to define a notion of length that we can apply to tangent vectors. This can be done in the form of an *inner product* on tangent spaces, called the *Riemannian metric*. A natural metric for the tangent space $T_X \text{St}(n, p)$ of the Stiefel manifold is the Euclidean metric of the embedding space $\mathbb{C}^{n \times p}$, which is given by the real part of the Frobenius inner product:

$$g_W : T_X \text{St}(n, p) \times T_X \text{St}(n, p) \rightarrow \mathbb{R}, \quad g_X(\xi_1, \xi_2) = \text{Re Tr} \left(\xi_1^\dagger \xi_2 \right). \quad (\text{B.2})$$

Equipped with a Riemannian metric the Stiefel manifold becomes a Riemannian submanifold of $\mathbb{C}^{n \times p}$.

With these definitions, we can now formulate the optimization problem as the problem of finding the isometry $W_{\text{opt}} \in \text{St}(n, p)$ that minimizes the cost function

$$f : \text{St}(n, p) \rightarrow \mathbb{R}, \quad X \mapsto f(X). \quad (\text{B.3})$$

B.2 Gradients, retractions, and vector transport

First order optimization algorithms like Gradient Descent and Conjugate Gradients use the gradient of the cost function to update the search direction at each iteration. In the case of the Stiefel manifold and the cost function (B.3), we first define the matrix of partial derivatives $D \in \mathbb{C}^{n \times p}$ of f at $X \in \text{St}(n, p)$ by

$$D_{ij} := \left. \frac{\partial f}{\partial \text{Re}(X_{ij})} \right|_X + i \left. \frac{\partial f}{\partial \text{Im}(X_{ij})} \right|_X. \quad (\text{B.4})$$

With this definition, the directional derivative $\text{D}f(X)[Z]$ at $X \in \text{St}(n, p)$ in direction $Z \in \mathbb{C}^{n \times p}$ is simply given by an inner product of D with the direction Z , using the Riemannian metric (B.2):

$$\begin{aligned} g_X(D, Z) &= \text{Re Tr} \left(D^\dagger Z \right) = \text{Re} \sum_{ij} D_{ij}^* Z_{ij} \\ &= \sum_{ij} \left(\left. \frac{\partial f}{\partial \text{Re}(X_{ij})} \right|_X \text{Re } Z_{ij} + \left. \frac{\partial f}{\partial \text{Im}(X_{ij})} \right|_X \text{Im } Z_{ij} \right) \\ &=: \text{D}f(X)[Z]. \end{aligned}$$

With this we can now define the gradient $\nabla f(X)$ of f at $X \in \text{St}(n, p)$ as the projection of the partial derivative matrix (B.4) to the tangent space [48, 50]:

$$\nabla f(X) := P_X D = D - \frac{1}{2} X \left(X^\dagger D + D^\dagger X \right), \quad (\text{B.5})$$

where we used the projection (B.1).

After a search direction ξ has been computed, we would like to update the iterate X as $X' = X + \alpha\xi$ with a given step size $\alpha \in \mathbb{R}$. However, in this case the next iterate X' is not guaranteed to remain in the manifold. For this reason it is convenient to define the notion of a *retraction*. A retraction is a function

$$R_\xi : \mathbb{R} \rightarrow \text{St}(n, p), \quad \alpha \mapsto R_\xi(\alpha),$$

that satisfies $R_\xi(0) = X$ and $\left. \frac{dR_\xi(\alpha)}{d\alpha} \right|_{\alpha=0} = \xi$. One can think of the retraction as moving in the direction of ξ while staying on the manifold. There exist different possible retractions for the Stiefel manifold. A contraction that is particularly easy to compute and yields good results in practice is the retraction

$$R_\xi \alpha = \text{qf}(X + \alpha\xi),$$

where $\text{qf}(A)$ denotes the Q -factor of the QR-decomposition $A = QR$.

Some Optimization algorithms, for example Conjugate Gradients, additionally use the search directions from previous iterations for computing the next search direction. In Riemannian optimization algorithms, these search directions must first be transported from the tangent space of the previous iterate to the tangent space of the current iterate. This can be performed by using a *vector transport* [48]. Let $\xi_k \in T_{X_k} \text{St}(n, p)$ be the search direction for the iterate $X_k \in \text{St}(n, p)$, and let $X_{k+1} \in \text{St}(n, p)$ be the next iterate. The vector transport $T_{k \rightarrow k+1}$ is then a function

$$T_{k \rightarrow k+1} : T_{X_k} \text{St}(n, p) \rightarrow T_{X_{k+1}} \text{St}(n, p), \quad \xi_k \mapsto T_{k \rightarrow k+1}(\xi_k).$$

For Riemannian submanifolds of Euclidean vector spaces, a simple vector transport is given by the projection onto the current tangent space [48],

$$T_{k \rightarrow k+1}(\xi_k) = P_{X_{k+1}} \xi_k,$$

where we used the projection (B.1).

B.3 Conjugate Gradients

The *Conjugate Gradients* (CG) algorithm [62–64] was initially introduced as an iterative method for solving large systems of linear equations of the form $Ax = b$ with a known vector b , a known, square, positive-definite matrix A , and an unknown vector x . It is however found that the method also works well on non-linear problems, often outperforming simple Gradient Descent. We will only discuss non-linear GD, for an introduction to linear GD see [62]. The main idea of CG is to compute an accumulated search direction ξ_k from the gradients at previous iterates as

$$\xi_k = -\nabla f(X_k) + \beta_k \xi_{k-1}.$$

There has been a lot of research on determining good algorithms for computing the parameter β_k . Two popular choices are the *Fletcher-Reeves formula* [48]

$$\beta_k^{\text{FR}} = \frac{\langle \nabla f(x_k), \nabla f(x_k) \rangle}{\langle \nabla f(x_{k-1}), \nabla f(x_{k-1}) \rangle}$$

and the *Polak-Ribiere formula* [48]

$$\beta_k^{\text{PR}} = \frac{\langle \nabla f(x_k), \nabla f(x_k) - \nabla f(x_{k-1}) \rangle}{\langle \nabla f(x_{k-1}), \nabla f(x_{k-1}) \rangle},$$

where $\langle \cdot, \cdot \rangle$ denotes the inner product of the vector space. After the search direction is computed, the next iterate is computed as $x_{k+1} = x_k + \alpha_k \xi_k$, where α_k is determined using a suitable line-search procedure, e.g. Armijo line search [48]. The initial search direction is simply the direction of steepest descent, $\xi_0 = -\nabla f(x_0)$.

On Riemannian manifolds, the inner product $\langle \cdot, \cdot \rangle$ is replaced by the Riemannian metric. Additionally, a retraction must be used for updating the iterates, $x_{k+1} = R_{\xi_k}(\alpha_k)$. Finally, a suitable vector transport $T_{k-1 \rightarrow k}$ must be used for computing β_k , if the formula requires gradients or search direction from previous iterates. For an in-depth explanation of how CG on the Stiefel manifold can be implemented, see [48, 50, 65].

In our implementation we additionally used Powell's restart strategy [52, 63, 66], which can significantly improve the efficiency of CG.

B.4 Trust Region Method

Trust-region methods (TRM) are a class of second order optimization techniques that are known for their desirable global convergence properties with a local superlinear rate of convergence [48, 67]. The main idea of the TRM is to locally approximate the cost function f by a quadratic model

$$m_{X_k}(\eta) = f(X_k) + \langle \nabla f(X_k), \eta \rangle + \frac{1}{2} \langle \text{Hess} f(X_k)[\eta], \eta \rangle \approx f(X_k + \eta),$$

in a *trust-region* $\langle \eta, \eta \rangle \leq \Delta_k^2$ of radius Δ_k around the current iterate X_k . To define this model, one must compute the Hessian-vector product $\text{Hess} f(X_k)[\eta]$ or an approximation thereof. On Riemannian submanifolds of Euclidean vector spaces, the Hessian can be computed by projecting the directional derivative $D(\nabla f(X_k))[\eta]$ of the gradient $\nabla f(X_k)$ in direction η from the embedding space to the tangent space of X_k [48]. Since the Stiefel manifold is such a Riemannian submanifold, it holds

$$\text{Hess} f(X_k)[\eta] = P_{X_k} D(\nabla f(X_k))[\eta]$$

with the projection (B.1). Optimizing the cost function on the quadratic model inside the trust-region is called the *trust-region subproblem* and can be solved via *truncated Conjugate Gradients* (tCG), which converges quickly on the quadratic model [48]. The solution of the trust-region subproblem is a vector η_{opt} . The proposed next iterate is then given by moving in the direction η_{opt} as $X_{k+1} = R_{\eta_{\text{opt}}}(1)$. To decide if the next iterate is accepted or not, we proceed to compute the quotient

$$\rho_k := \frac{f(X_k) - f(X_{k+1})}{m_{X_k}(0) - m_{X_k}(\eta_{\text{opt}})}.$$

The quotient ρ_k is a measure of how well the cost function is represented by the model m_{X_k} . If ρ_k is too small, the model is very inaccurate. In this case the proposed update step must be rejected and the trust-region radius Δ_k must be reduced. If ρ_k is close to one, the model is a good approximation of the cost function, and thus the update step can be accepted and the trust-region radius increased. If $\rho_k \gg 1$, the model is inaccurate, but the iteration still produces a significant decrease in the cost. One possible strategy in this situation is to accept the update and to increase the trust-region radius, hoping that this behaviour will remain in the following iterations, decreasing the cost further. This finally concludes one iteration of the TRM. For more details on the TRM on Riemannian manifolds, see [48, 52, 67].

Appendix C

Computing the Gradient and Hessian of the Disentangling Cost Functions

In this appendix we compute the Riemannian gradients and Hessian-vector products for the cost functions (3.4) and (3.5). For this it is first necessary to derive the derivative of the complex-valued singular value decomposition (SVD), which we show in Section C.1. The derivation is similar to [68]. We then proceed by deriving the gradients in section C.2 and the hessian-vector products in section C.3.

C.1 Derivative of the SVD

Let $A \in \mathbb{C}^{m \times n}$ of rank $k \leq \min(m, n)$. The SVD of A is defined as $A = USV^\dagger$, with $U \in \mathbb{C}^{m \times k}$, $S \in \mathbb{R}^{k \times k}$ diagonal, $V \in \mathbb{C}^{n \times k}$ and

$$U^\dagger U = V^\dagger V = \mathbb{1}_k. \quad (\text{C.1})$$

In this definition we already truncated singular values $s_j = 0$, such that S has only non-zero entries on the diagonal. Let $dA \in \mathbb{C}^{m \times n}$ be an infinitesimal change of A . We are interested in the infinitesimal changes dU , dS and dV that are obtained when performing the SVD $(A + dA) = (U + dU)(S + dS)(V + dV)^\dagger$. Up to first order we obtain

$$dA = dUSV^\dagger + UdSV^\dagger + USdV^\dagger. \quad (\text{C.2})$$

Differentiating Equation (C.1) yields $dU^\dagger U + U^\dagger dU = 0$ and $dV^\dagger V + V^\dagger dV = 0$. It follows that $d\Omega_U := U^\dagger dU$ and $d\Omega_V := V^\dagger dV$ are $k \times k$ anti-hermitian matrices.

One can always find matrices $U_\perp \in \mathbb{C}^{m \times (m-k)}$ and $V_\perp \in \mathbb{C}^{n \times (n-k)}$ such that $[U \ U_\perp]$ and $[V \ V_\perp]$ are unitary and it holds $U^\dagger U_\perp = 0$ and $V^\dagger V_\perp = 0$. This procedure is called unitary completion and can for example be computed by using the Gram-Schmidt algorithm. The notation $[U \ U_\perp]$ means stacking the columns of U and U_\perp to form a $m \times m$ matrix. We may now expand dU as

$$dU = Ud\Omega_U + U_\perp dK_U$$

and dV as

$$dV = V d\Omega_V + V_\perp dK_V,$$

with $dK_U \in \mathbb{C}^{(m-k) \times k}$ and $dK_V \in \mathbb{C}^{(n-k) \times k}$ yet to be determined. We proceed by left-multiplying (C.2) by U^\dagger and right-multiplying by V to obtain

$$\begin{aligned} dP &:= U^\dagger dAV = U^\dagger dUS + dS + SdV^\dagger V \\ &= d\Omega_U S + dS + Sd\Omega_V^\dagger. \end{aligned} \quad (\text{C.3})$$

Since $d\Omega_U$ and $d\Omega_V$ are anti-hermitian, there diagonal elements are purely imaginary. However, dS is a diagonal matrix with purely real entries. Thus it is immediately clear that

$$dS = \mathbb{1}_k \circ \text{Re}[dP],$$

with the *Hadamard product* $(A \circ B)_{i,j} = A_{i,j} \cdot B_{i,j}$. It further follows

$$d\Omega_U S - Sd\Omega_V = \mathbb{1}_k \circ i \text{Im}[dP] + \bar{\mathbb{1}}_k \circ dP. \quad (\text{C.4})$$

Here, the notation $\bar{\mathbb{1}}_k$ means a $k \times k$ matrix with zeros on the diagonal and ones everywhere else. Taking the complex conjugate of (C.4) yields

$$-Sd\Omega_U + d\Omega_V S = -\mathbb{1}_k \circ i \text{Im}[dP] + \bar{\mathbb{1}}_k \circ dP^\dagger. \quad (\text{C.5})$$

To proceed we right-multiply (C.4) by S , left-multiply (C.5) by S and add the two equations together, yielding

$$d\Omega_U S^2 - S^2 d\Omega_U = \bar{\mathbb{1}}_k \circ SdP + \bar{\mathbb{1}}_k \circ dP^\dagger S = \bar{\mathbb{1}}_k \circ [dPS + SdP^\dagger], \quad (\text{C.6})$$

where we used the fact that $D(A \circ B) = DA \circ B = A \circ DB$ and $(A \circ B)D = AD \circ B = A \circ BD$ for diagonal matrices D . We now want to solve Equation (C.6) for $d\Omega_U$. The solution is given by

$$d\Omega_U = F \circ [dPS + SdP^\dagger] \quad (\text{C.7})$$

with

$$F_{i,j} := \begin{cases} \frac{1}{d_j^2 - d_i^2} & i \neq j \\ 0 & i = j \end{cases}, \quad (\text{C.8})$$

which can be easily checked by inserting. We can obtain a similar equation for $d\Omega_V$ by left-multiplying (C.4) by S and right-multiplying (C.5) by S before adding the two equations. The resulting equation is solved by

$$d\Omega_V = F \circ [SdP + dP^\dagger S]. \quad (\text{C.9})$$

Equations (C.7) and (C.9) do not fix the diagonals of $d\Omega_U$ and $d\Omega_V$. We can determine these remaining free parameters by looking at the diagonal elements of equation (C.4):

$$\begin{aligned} \mathbb{1}_k \circ [d\Omega_U S - S d\Omega_V] &= \mathbb{1} \circ i \operatorname{Im} [dP] \\ \Rightarrow \mathbb{1}_k \circ [d\Omega_U - d\Omega_V] &= \mathbb{1}_k \circ i \operatorname{Im} [dP] S^{-1}. \end{aligned}$$

We can solve this equation by setting

$$\begin{aligned} d\Omega_U &= F \circ [dPS + S dP^\dagger] + \mathbb{1}_k \circ dD, \\ d\Omega_V &= F \circ [S dP + dP^\dagger S] - \mathbb{1}_k \circ dD, \end{aligned}$$

with

$$dD := \frac{i}{2} \operatorname{Im} [dP] S^{-1}.$$

It remains to find dK_U and dK_V . We can compute dK_U by left-multiplying (C.2) by U_\perp^\dagger and right-multiplying by VS^{-1} , yielding

$$dK_U = U_\perp^\dagger dA V S^{-1}.$$

Similarly, we can left-multiply (C.2)[†] by V_\perp^\dagger and right-multiplying by US^{-1} to obtain

$$dK_V = V_\perp^\dagger dA^\dagger U S^{-1}.$$

Putting everything together, we obtain

$$\begin{aligned} dU &= U \left(F \circ [dPS + S dP^\dagger] + \mathbb{1}_k \circ dD \right) + (\mathbb{1}_m - UU^\dagger) dA V S^{-1}, \\ dS &= \mathbb{1}_k \circ \operatorname{Re} [dP], \\ dV &= V \left(F \circ [S dP + dP^\dagger S] - \mathbb{1}_k \circ dD \right) + (\mathbb{1}_n - VV^\dagger) dA U S^{-1}, \end{aligned} \tag{C.10}$$

with dP defined in Equation (C.3) and F defined in Equation (C.8). To arrive at the final expressions for dU and dV we used the fact that $M_U := [U U_\perp]$ and $M_V := [V V_\perp]$ are unitary and thus $M_U M_U^\dagger = UU^\dagger + U_\perp U_\perp^\dagger = \mathbb{1}_m$ and similarly $VV^\dagger + V_\perp V_\perp^\dagger = \mathbb{1}_n$ to eliminate $U_\perp U_\perp^\dagger$ and $V_\perp V_\perp^\dagger$.

There is one small subtlety left to discuss. The SVD is not unique, but has a gauge degree of freedom: A diagonal matrix of complex phases $\Lambda_{j,j} = e^{i\theta_j}$ can be inserted as $A = USV^\dagger = U'SV'^\dagger = (U\Lambda)S(V\Lambda)^\dagger$. This means that the exact values of dU and dV are ill-defined and it is only possible to compute derivatives of functions that are gauge-invariant, i.e. functions where Λ is cancelled with its adjoint.

C.2 Gradients

We now compute Riemannian gradients for the two cost functions discussed in Section 3.2.2, namely the truncation error

$$f_{\text{trunc}}(U, \theta) = \sqrt{\sum_{\mu=\chi+1}^{\chi D^2} S_{\mu}^2} = \sqrt{1 - \sum_{\mu=1}^{\chi} S_{\mu}^2}$$

and the Rényi-entropy

$$f_{\text{Rényi}}(U, \theta, \alpha) = \frac{1}{1-\alpha} \log \text{Tr}(\rho^{\alpha}) = \frac{1}{1-\alpha} \log \left(\sum_{\mu=1}^{\chi D^2} S_{\mu}^{2\alpha} \right).$$

The singular values stem from the SVD $U\theta = XSY$ as shown in figure 3.10. We first compute the derivative of a single singular value S_{μ} with respect to U . Using the product rule for matrices [69] and the derivative of the SVD (C.10), we obtain

$$\left(\frac{dS_{\mu}}{dU} \right)_{i,j,k,l} = \text{Diagram showing the derivative of } S_{\mu} \text{ with respect to } U \text{ via the SVD components } X, Y^*, \text{ and } \theta^*.$$

We can then use this result to compute the derivative of the truncation error as

$$\frac{d}{dU} f_{\text{trunc}}(U, \theta) = -\frac{1}{f_{\text{trunc}}(U, \theta)} \sum_{\mu} S_{\mu} \frac{dS_{\mu}}{dU}$$

and the derivative of the Rényi-entropy as

$$\frac{d}{dU} f_{\text{Rényi}}(U, \theta, \alpha) = \frac{2\alpha}{1-\alpha} \frac{1}{\sum_{\mu} S_{\mu}^{2\alpha}} \sum_{\mu} S_{\mu}^{2\alpha-1} \frac{dS_{\mu}}{dU}.$$

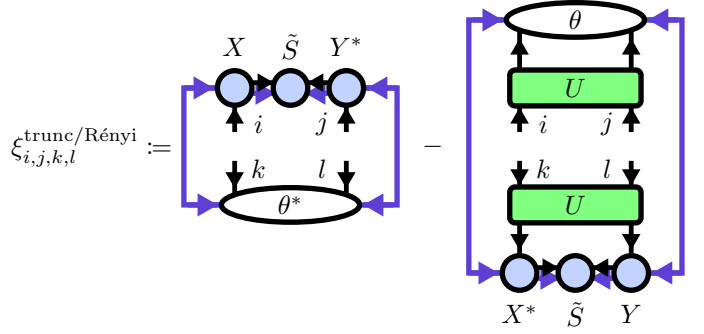
As a last step, the derivatives must be projected back to the tangent space of U , see Equation (B.5). We obtain

$$(\nabla f_{\text{trunc}}(U, \theta))_{i,j,k,l} = \frac{1}{2f_{\text{trunc}}(U, \theta)} \xi_{i,j,k,l}^{\text{trunc}}$$

and

$$(\nabla f_{\text{Rényi}}(U, \theta, \alpha))_{i,j,k,l} = \frac{\alpha}{1-\alpha} \frac{1}{\sum_{\mu} S_{\mu}^{2\alpha}} \xi_{i,j,k,l}^{\text{Rényi}}$$

respectively, with



where $\tilde{S} = S$ for ξ^{trunc} and $\tilde{S} = S^{2\alpha-1}$ for $\xi^{\text{Rényi}}$.

C.3 Hessian-Vector Products

In this section we compute the Hessian-vector product of ∇f and ΔU . We start by first calculating the directional derivative of the gradient in direction ΔU

$$D(\nabla f)[\Delta U],$$

which we subsequently need to project to the tangent space of U . For matrix multiplication it holds[69]

$$D(AB)[\Delta A] = \Delta AB.$$

Directional derivatives of X , U and Y can be obtained with equation (C.10) by setting $dA = \Delta U \theta$. The final result are the directional derivatives

$$\begin{aligned} ((D(\nabla f_{\text{trunc}})[\Delta U]))_{i,j,k,l} = \\ - \frac{1}{2f_{\text{trunc}}(U, \theta)} \cdot \left\{ \frac{1}{f_{\text{trunc}}(U, \theta)^2} \sum_{\mu=1}^{\chi} S_{\mu} (DS_{\mu}[\Delta U]) \xi_{i,j,k,l} + G_{i,j,k,l}^{\text{trunc}} \right\} \end{aligned}$$

and

$$\begin{aligned} ((D(\nabla f_{\text{Rényi}})[\Delta U]))_{i,j,k,l} = \\ \frac{\alpha}{1-\alpha} \left\{ \frac{2\alpha}{\left(\sum_{\mu} S_{\mu}^{2\alpha}\right)^2} \sum_{\mu} S_{\mu}^{2\alpha-1} dS_{\mu} \xi_{i,j,k,l} + \frac{1}{\sum_{\mu} S_{\mu}^{2\alpha}} G_{i,j,k,l}^{\text{Rényi}} \right\} \end{aligned}$$

with the definition of G^{trunc} and $G^{\text{Rényi}}$ given in tensor diagram notation in Figure C.1. Finally, The derivatives must be projected to the tangent space of U , see Equation (B.5).

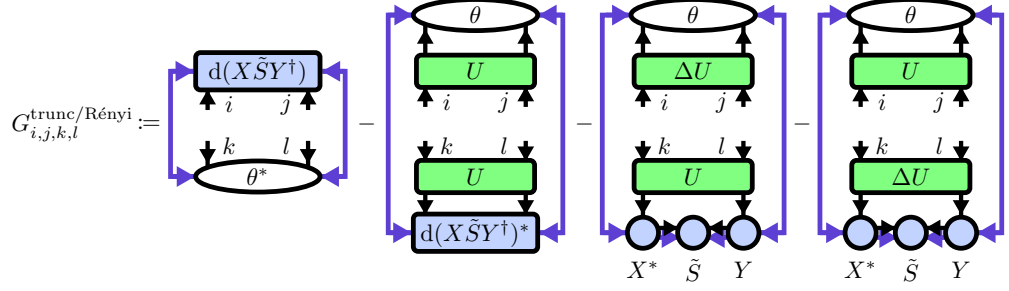


Figure C.1: In this figure we give the definition for G^{trunc} and $G^{\text{Rényi}}$ in tensor diagram notation. For G^{trunc} we set $\tilde{S} = S$ and for $G^{\text{Rényi}}$ we set $\tilde{S} = S^{2\alpha-1}$. The definition of $d(X\tilde{S}Y)$ is given in figure C.2

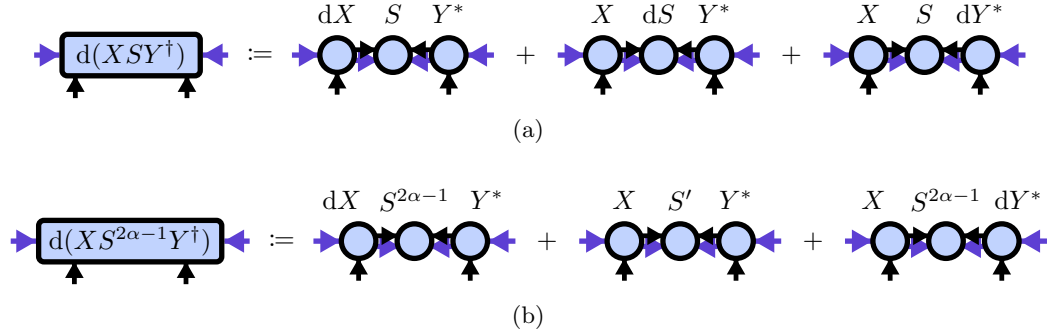


Figure C.2: The definitions for (a) $d(XSY^\dagger)$ and (b) $d(XS^{2\alpha-1}Y^\dagger)$ are given in tensor diagram notation. In (b), we use $S'_\mu := (2\alpha-1)S_\mu^{2\alpha-2}dS_\mu$.

Bibliography

- [1] Daniel C Tsui, Horst L Stormer and Arthur C Gossard. ‘Two-dimensional magnetotransport in the extreme quantum limit’. In: *Physical Review Letters* 48.22 (1982), p. 1559.
- [2] Robert B Laughlin. ‘Anomalous quantum Hall effect: an incompressible quantum fluid with fractionally charged excitations’. In: *Physical Review Letters* 50.18 (1983), p. 1395.
- [3] Horst L Stormer, Daniel C Tsui and Arthur C Gossard. ‘The fractional quantum Hall effect’. In: *Reviews of Modern Physics* 71.2 (1999), S298.
- [4] Tian-Heng Han et al. ‘Fractionalized excitations in the spin-liquid state of a kagome-lattice antiferromagnet’. In: *Nature* 492.7429 (2012), pp. 406–410.
- [5] Xiao-Gang Wen. ‘Colloquium: Zoo of quantum-topological phases of matter’. In: *Reviews of Modern Physics* 89.4 (2017), p. 041004.
- [6] J George Bednorz and K Alex Müller. ‘Possible high T_c superconductivity in the Ba- La- Cu- O system’. In: *Zeitschrift für Physik B Condensed Matter* 64.2 (1986), pp. 189–193.
- [7] Patrick A Lee, Naoto Nagaosa and Xiao-Gang Wen. ‘Doping a Mott insulator: Physics of high-temperature superconductivity’. In: *Reviews of modern physics* 78.1 (2006), pp. 17–85.
- [8] Anders W Sandvik and Juhani Kurkijärvi. ‘Quantum Monte Carlo simulation method for spin systems’. In: *Physical Review B* 43.7 (1991), p. 5950.
- [9] Anders W Sandvik. ‘Computational studies of quantum spin systems’. In: *AIP Conference Proceedings*. Vol. 1297. 1. American Institute of Physics. 2010, pp. 135–338.
- [10] EY Loh Jr et al. ‘Sign problem in the numerical simulation of many-electron systems’. In: *Physical Review B* 41.13 (1990), p. 9301.
- [11] Steven R White. ‘Density matrix formulation for quantum renormalization groups’. In: *Physical review letters* 69.19 (1992), p. 2863.
- [12] Jorge Dukelsky et al. ‘Equivalence of the variational matrix product method and the density matrix renormalization group applied to spin chains’. In: *Europhysics letters* 43.4 (1998), p. 457.

- [13] Ulrich Schollwöck. ‘The density-matrix renormalization group in the age of matrix product states’. In: *Annals of physics* 326.1 (2011), pp. 96–192.
- [14] Román Orús. ‘A practical introduction to tensor networks: Matrix product states and projected entangled pair states’. In: *Annals of physics* 349 (2014), pp. 117–158.
- [15] M B Hastings. ‘An area law for one-dimensional quantum systems’. In: *Journal of Statistical Mechanics: Theory and Experiment* 2007.08 (Aug. 2007), P08024. DOI: 10.1088/1742-5468/2007/08/P08024. URL: <https://dx.doi.org/10.1088/1742-5468/2007/08/P08024>.
- [16] J. Eisert, M. Cramer and M. B. Plenio. ‘Colloquium: Area laws for the entanglement entropy’. In: *Rev. Mod. Phys.* 82 (1 Feb. 2010), pp. 277–306. DOI: 10.1103/RevModPhys.82.277. URL: <https://link.aps.org/doi/10.1103/RevModPhys.82.277>.
- [17] Frank Verstraete and J Ignacio Cirac. ‘Matrix product states represent ground states faithfully’. In: *Physical Review B—Condensed Matter and Materials Physics* 73.9 (2006), p. 094423.
- [18] Guifré Vidal. ‘Efficient simulation of one-dimensional quantum many-body systems’. In: *Physical review letters* 93.4 (2004), p. 040502.
- [19] Jutho Haegeman et al. ‘Time-dependent variational principle for quantum lattices’. In: *Physical review letters* 107.7 (2011), p. 070601.
- [20] Frank Verstraete and J Ignacio Cirac. ‘Renormalization algorithms for quantum-many body systems in two and higher dimensions’. In: *arXiv preprint cond-mat/0407066* (2004).
- [21] Michael Lubasch, J Ignacio Cirac and Mari-Carmen Banuls. ‘Unifying projected entangled pair state contractions’. In: *New Journal of Physics* 16.3 (2014), p. 033014.
- [22] Michael Lubasch, J Ignacio Cirac and Mari-Carmen Banuls. ‘Algorithms for finite projected entangled pair states’. In: *Physical Review B* 90.6 (2014), p. 064425.
- [23] Michael P. Zaletel and Frank Pollmann. ‘Isometric Tensor Network States in Two Dimensions’. In: *Phys. Rev. Lett.* 124 (3 Jan. 2020), p. 037201. DOI: 10.1103/PhysRevLett.124.037201. URL: <https://link.aps.org/doi/10.1103/PhysRevLett.124.037201>.
- [24] Reza Haghshenas, Matthew J. O’Rourke and Garnet Kin-Lic Chan. ‘Conversion of projected entangled pair states into a canonical form’. In: *Phys. Rev. B* 100 (5 Aug. 2019), p. 054404. DOI: 10.1103/PhysRevB.100.054404. URL: <https://link.aps.org/doi/10.1103/PhysRevB.100.054404>.

- [25] Katharine Hyatt and E. M. Stoudenmire. *DMRG Approach to Optimizing Two-Dimensional Tensor Networks*. 2020. arXiv: 1908.08833 [cond-mat.str-el]. URL: <https://arxiv.org/abs/1908.08833>.
- [26] Sheng-Hsuan Lin, Michael P. Zaletel and Frank Pollmann. ‘Efficient simulation of dynamics in two-dimensional quantum spin systems with isometric tensor networks’. In: *Phys. Rev. B* 106 (24 Dec. 2022), p. 245102. DOI: 10.1103/PhysRevB.106.245102. URL: <https://link.aps.org/doi/10.1103/PhysRevB.106.245102>.
- [27] Tomohiro Soejima et al. ‘Isometric tensor network representation of string-net liquids’. In: *Phys. Rev. B* 101 (8 Feb. 2020), p. 085117. DOI: 10.1103/PhysRevB.101.085117. URL: <https://link.aps.org/doi/10.1103/PhysRevB.101.085117>.
- [28] Daniel Malz and Rahul Trivedi. *Computational complexity of isometric tensor network states*. 2024. arXiv: 2402.07975 [quant-ph]. URL: <https://arxiv.org/abs/2402.07975>.
- [29] Zhi-Yuan Wei, Daniel Malz and J. Ignacio Cirac. ‘Sequential Generation of Projected Entangled-Pair States’. In: *Phys. Rev. Lett.* 128 (1 Jan. 2022), p. 010607. DOI: 10.1103/PhysRevLett.128.010607. URL: <https://link.aps.org/doi/10.1103/PhysRevLett.128.010607>.
- [30] Lucas Slattery and Bryan K. Clark. *Quantum Circuits For Two-Dimensional Isometric Tensor Networks*. 2021. arXiv: 2108.02792 [quant-ph]. URL: <https://arxiv.org/abs/2108.02792>.
- [31] Yu-Jie Liu, Kirill Shtengel and Frank Pollmann. *Topological quantum phase transitions in 2D isometric tensor networks*. 2024. arXiv: 2312.05079 [quant-ph]. URL: <https://arxiv.org/abs/2312.05079>.
- [32] Zhehao Dai et al. *Fermionic Isometric Tensor Network States in Two Dimensions*. 2024. arXiv: 2211.00043 [cond-mat.str-el]. URL: <https://arxiv.org/abs/2211.00043>.
- [33] Yantao Wu et al. ‘Two-dimensional isometric tensor networks on an infinite strip’. In: *Phys. Rev. B* 107 (24 June 2023), p. 245118. DOI: 10.1103/PhysRevB.107.245118. URL: <https://link.aps.org/doi/10.1103/PhysRevB.107.245118>.
- [34] Maurits S. J. Tepaske and David J. Luitz. ‘Three-dimensional isometric tensor networks’. In: *Phys. Rev. Res.* 3 (2 June 2021), p. 023236. DOI: 10.1103/PhysRevResearch.3.023236. URL: <https://link.aps.org/doi/10.1103/PhysRevResearch.3.023236>.

- [35] Wilhelm Kadow, Frank Pollmann and Michael Knap. ‘Isometric tensor network representations of two-dimensional thermal states’. In: *Phys. Rev. B* 107 (20 May 2023), p. 205106. DOI: 10.1103/PhysRevB.107.205106. URL: <https://link.aps.org/doi/10.1103/PhysRevB.107.205106>.
- [36] Benjamin Sappier. *YB-isoTPS*. <https://github.com/SnackerBit/YB-isoTPS>. 2024.
- [37] Carl Eckart and Gale Young. ‘The approximation of one matrix by another of lower rank’. In: *Psychometrika* 1.3 (1936), pp. 211–218.
- [38] Johannes Hauschild and Frank Pollmann. ‘Efficient numerical simulations with Tensor Networks: Tensor Network Python (TeNPy)’. In: *SciPost Phys. Lect. Notes* (2018), p. 5. DOI: 10.21468/SciPostPhysLectNotes.5. URL: <https://scipost.org/10.21468/SciPostPhysLectNotes.5>.
- [39] Frank Verstraete, Juan J Garcia-Ripoll and Juan Ignacio Cirac. ‘Matrix product density operators: Simulation of finite-temperature and dissipative systems’. In: *Physical review letters* 93.20 (2004), p. 207204.
- [40] Jutho Haegeman et al. ‘Unifying time evolution and optimization with matrix product states’. In: *Physical Review B* 94.16 (2016), p. 165116.
- [41] Naomichi Hatano and Masuo Suzuki. ‘Finding exponential product formulas of higher orders’. In: *Quantum annealing and other optimization methods*. Springer, 2005, pp. 37–68.
- [42] J Ignacio Cirac et al. ‘Matrix product states and projected entangled pair states: Concepts, symmetries, theorems’. In: *Reviews of Modern Physics* 93.4 (2021), p. 045003.
- [43] F. Verstraete et al. ‘Criticality, the Area Law, and the Computational Power of Projected Entangled Pair States’. In: *Phys. Rev. Lett.* 96 (22 June 2006), p. 220601. DOI: 10.1103/PhysRevLett.96.220601. URL: <https://link.aps.org/doi/10.1103/PhysRevLett.96.220601>.
- [44] RJ Baxter and IG Enting. ‘Series expansions from corner transfer matrices: the square lattice ising model’. In: *Journal of Statistical Physics* 21 (1979), pp. 103–123.
- [45] Glen Evenbly and Guifré Vidal. ‘Algorithms for entanglement renormalization’. In: *Physical Review B—Condensed Matter and Materials Physics* 79.14 (2009), p. 144108.
- [46] Glen Evenbly and Guifré Vidal. ‘Algorithms for entanglement renormalization: boundaries, impurities and interfaces’. In: *Journal of statistical physics* 157 (2014), pp. 931–978.

- [47] Johannes Hauschild et al. ‘Finding purifications with minimal entanglement’. In: *Phys. Rev. B* 98 (23 Dec. 2018), p. 235163. DOI: 10.1103/PhysRevB.98.235163. URL: <https://link.aps.org/doi/10.1103/PhysRevB.98.235163>.
- [48] P.-A. Absil, R. Mahony and Rodolphe Sepulchre. *Optimization Algorithms on Matrix Manifolds*. Princeton: Princeton University Press, 2008. ISBN: 9781400830244. DOI: doi : 10.1515/9781400830244. URL: <https://doi.org/10.1515/9781400830244>.
- [49] Steven Thomas Smith. ‘Optimization techniques on Riemannian manifolds’. In: *arXiv preprint arXiv:1407.5965* (2014).
- [50] Markus Hauru, Maarten Van Damme and Jutho Haegeman. ‘Riemannian optimization of isometric tensor networks’. In: *SciPost Physics* 10.2 (Feb. 2021). ISSN: 2542-4653. DOI: 10.21468/scipostphys.10.2.040. URL: <http://dx.doi.org/10.21468/SciPostPhys.10.2.040>.
- [51] Ilia A Luchnikov, Mikhail E Krechetov and Sergey N Filippov. ‘Riemannian geometry and automatic differentiation for optimization problems of quantum physics and quantum technologies’. In: *New Journal of Physics* 23.7 (July 2021), p. 073006. ISSN: 1367-2630. DOI: 10.1088/1367-2630/ac0b02. URL: <http://dx.doi.org/10.1088/1367-2630/ac0b02>.
- [52] James Townsend, Niklas Koep and Sebastian Weichwald. *Pymanopt: A Python Toolbox for Optimization on Manifolds using Differentiation*. 2016. arXiv: 1603.03236 [cs.MS].
- [53] Jakob Unfried, Johannes Hauschild and Frank Pollmann. ‘Fast time evolution of matrix product states using the QR decomposition’. In: *Physical Review B* 107.15 (2023), p. 155133.
- [54] A Yu Kitaev. ‘Fault-tolerant quantum computation by anyons’. In: *Annals of physics* 303.1 (2003), pp. 2–30.
- [55] Alexei Kitaev and Liang Kong. ‘Models for gapped boundaries and domain walls’. In: *Communications in Mathematical Physics* 313.2 (2012), pp. 351–373.
- [56] Timothy H Hsieh. ‘From d-dimensional Quantum to d+ 1-dimensional Classical Systems’. In: *Student Review* (2016).
- [57] MSL du Croo de Jongh and JMJ Van Leeuwen. ‘Critical behavior of the two-dimensional Ising model in a transverse field: A density-matrix renormalization calculation’. In: *Physical Review B* 57.14 (1998), p. 8494.
- [58] Bikas K Chakrabarti, Amit Dutta and Parongama Sen. *Quantum Ising phases and transitions in transverse Ising models*. Vol. 41. Springer Science & Business Media, 2008.

-
- [59] Henk WJ Blöte and Youjin Deng. ‘Cluster Monte Carlo simulation of the transverse Ising model’. In: *Physical Review E* 66.6 (2002), p. 066110.
 - [60] Örs Legeza and Gábor Fáth. ‘Accuracy of the density-matrix renormalization-group method’. In: *Physical Review B* 53.21 (1996), p. 14349.
 - [61] Michael P Zaletel et al. ‘Time-evolving a matrix product state with long-ranged interactions’. In: *Physical Review B* 91.16 (2015), p. 165112.
 - [62] Jonathan Richard Shewchuk et al. ‘An introduction to the conjugate gradient method without the agonizing pain’. In: (1994).
 - [63] William W Hager and Hongchao Zhang. ‘A survey of nonlinear conjugate gradient methods’. In: *Pacific journal of Optimization* 2.1 (2006), pp. 35–58.
 - [64] William W Hager and Hongchao Zhang. ‘Algorithm 851: CG_DESCENT, a conjugate gradient method with guaranteed descent’. In: *ACM Transactions on Mathematical Software (TOMS)* 32.1 (2006), pp. 113–137.
 - [65] Xiaojing Zhu. ‘A Riemannian conjugate gradient method for optimization on the Stiefel manifold’. In: *Computational optimization and Applications* 67 (2017), pp. 73–110.
 - [66] Cai-Xia Kou et al. ‘ON THE USE OF POWELL’S RESTART STRATEGY TO CONJUGATE GRADIENT METHODS’. In: *PACIFIC JOURNAL OF OPTIMIZATION* 10.1 (2014), pp. 85–104.
 - [67] P-A Absil, Christopher G Baker and Kyle A Gallivan. ‘Trust-region methods on Riemannian manifolds’. In: *Foundations of Computational Mathematics* 7 (2007), pp. 303–330.
 - [68] James Townsend. *Differentiating the singular value decomposition*. Tech. rep. Technical Report 2016, [https://j-towns.github.io/papers/svd-derivative ...](https://j-towns.github.io/papers/svd-derivative...), 2016.
 - [69] Kaare Brandt Petersen, Michael Syskind Pedersen et al. ‘The matrix cookbook’. In: *Technical University of Denmark* 7.15 (2008), p. 510.

Resources for Plotting

- [1] Mark Harrower Cynthia Brewer and The Pennsylvania State University. *COLORBREW 2.0*. URL: <https://colorbrewer2.org/> (visited on 30/07/2024).
- [2] Joachim Goedhart. *Color blind friendly palettes for data visualization*. URL: <https://thenode.biologists.com/data-visualization-with-flying-colors/research/> (visited on 30/07/2024).